Universidade de Lisboa

Faculdade de Ciências

Departamento de Física

Development of a Compton Camera for Prompt-gamma Detection in Hadron Therapy

Inês Lourenço Castelhano

Dissertação

Mestrado Integrado em Engenharia Biomédica e Biofísica

Perfil de Radiações em Diagnóstico e Terapia

2014

Universidade de Lisboa

Faculdade de Ciências

Departamento de Física

Development of a Compton Camera for Prompt-gamma Detection in Hadron Therapy

Inês Lourenço Castelhano

Dissertação orientada pelo Prof. Dr. Luís Peralta e pelo PD. Dr. Peter G. Thirolf

Mestrado Integrado em Engenharia Biomédica e Biofísica

2014

Ludwig-Maximilians-Universität München

Faculty of Physics

Chair of Medical Physics

Development of a Compton Camera for Prompt-gamma Detection in Hadron Therapy

Inês Lourenço Castelhano

Master Thesis

External Supervisor: PD. Dr. Peter G. Thirolf

Internal Supervisor: Prof. Dr. Luís Peralta

Associated Supervisor: Saad Aldawood, MSc.

Master in Biomedical Engineering and Biophysics

Field of Radiations in Diagnosis and Therapy

2014

Para ti, Mãe. Para ti, Pai.

Acknowledgments

Completing my MSc. degree was probably the hardest challenge of my 23 years of life. The six months spent in Munich were shared with many people, from Europe to Australia. First of all, it was a privilege to spend these six months in the Medical Physics Department of the Ludwig-Maximillians-Universität München, surrounded by amazing people.

My first debt of gratitude must go to my supervisor, PD. Dr. Peter Thirolf. He provided the vision, the motivation, best advice and help that I could have had. For teaching me that we don't die if we take one night shift or if we skip the lunch, especially to finish our (important) work. For sharing his knowledge everyday, with patience for an engineer instead of a physicist. You know I was the outlier of the group, but even so you have always supported me. In everything related to the thesis and my life in Germany, giving me the courage to go further than I thought I could.

The second person I want to thank is Prof. Dr. Luís Peralta. For, during my five years of college, being not only a Professor, but also a friend. I can say that your love for what you do also guided me through this path of Medical Physics, serving as an inspiration. For being always available to help me when I asked questions and for all the support. I hope in the future, we can contribute (together) to the development of this field in Portugal.

Special thanks to all my Professors, from primary school to college, that, in some way, contributed for what I know and what I am today. I want to thank Prof. Dr. Katia Parodi for giving me the opportunity to work in the Chair of Medical Physics. I would like to express my gratitude to Andrea Leinthaler, for the support when I arrived to Munich and for being available to help me with everything I needed.

I also wish to thank to all my friends from Portugal. Especially, Catarina, Adriana, Francisco e Rui, e todos os da Benedita, que são demasiados para enumerar. Obrigado por me lembrarem que o mundo é mais do que Faculdade e me ouvirem, apoiarem e divertirem tanto nestes (muitos) anos de amizade. Que nem a distância nos separe! À Mariana Castelhano, a prima, por, enfim, tantas coisas. Obrigado por me suportarem durante tanto tempo! The second group of friends, but not less important, are the people from LMU. Saad Aldawood, for basically everything related to work: for teaching me, supporting me, encouraging me not to give up when work is not going well... To all my other colleagues, Hugh, Tiago, Benedikt, Björn, Christian, Lars and all the others that are too many to write. It was a pleasure to

meet you, inside and outside the walls of the lab. Finally, to all my temporary friends/family in Munich, that showed me that it is not that bad to be far from home, I want to say thanks to Tiago, Lisandro, Tony, Ana, Xana, Inês Crespo, Inês Santos...

A short acknowledgment for my grandparents. Que se orgulhem de mim tanto quanto eu me orgulho de vós.

A ti, João Bernardo, por toda a paciência, palavras de carinho e encorajamento, especialmente nestes oito últimos meses. Sem ti a meu lado, nunca chegaria tão longe.

The last acknowledgment goes to my family, em especial para os meus pais, Tiago e Célia Castelhano. Sim, para vocês, porque são a verdadeira razão de tudo isto. Por me apoiarem em tudo (vá, quase tudo...) desde que me lembro e por me darem umas lições quando eu as mereci. Por providenciarem as condições para o meu sucesso enquanto estudante do curso de Engenharia Biomédica e Biofísica em Lisboa, em Itália e em Munique. Pelo apoio incondicional... Vocês são os melhores. Obrigada!*

*Por decisão pessoal, a autora desta Dissertação não escreve segundo o novo Acordo Ortográfico.

Resumo

A terapia com hadrões já provou ser uma opção eficiente de tratamento para tumores, devido à forte queda da dose distal, a mais importante das propriedades do pico de Bragg. No entanto, é necessária uma verificação precisa do alcance do feixe, de forma a localizar de forma exacta a queda distal da dose. A detecção de fotões gama-*prompt* é uma técnica promissora baseada na detecção de fotões emitidos imediatamente após a interação do feixe de hadrões com os tecidos-alvo. O uso desta técnica de monitorização foi sugerido depois de se ter provado existir uma correlação entre os gama-*prompt* e a queda distal da dose para feixes de hadrões. A câmara de Compton fornece informação para a reconstrução da posição de emissão destes fotões, que é obtida a partir da informação espacial e energética proveniente dos fotões e dos electrões que sofreram dispersão de Compton. A limitação cinemática introduzida pelo conhecimento simultâneo das características do fotão e do electrão dispersos de Compton restringe a posição original do fotão incidente a uma zona contida num arco de círculo, aumentando assim a eficiência da reconstrução da posição original.

A câmara de Compton apresentada consiste num detector de cintilação de $LaBr_3$(Ce) para a medição da energia do fotão disperso, combinado com um conjunto de 6 detectores de dispersão do tipo DSSSD, lidos por uma placa ASIC. Neste projecto, foi realizada uma calibração em energia do detector de $LaBr_3$, tendo-se obtido uma resolução em energia de 2.9% para energias superiores a 1.173 MeV. Foram também realizadas várias tentativas de medições da resolução espacial que se revelaram inconclusivas.

Finalmente, a câmara de Compton foi usada em duas experiências no acelerador *Tandem* de Garching, associada a uma electrónica com 256 canais para leitura do PMT do $LaBr_3$, através da qual foram obtidos vários espectros gama-*prompt*.

Palavras-chave: Câmara de Compton; Terapia com hadrões; Gama-*prompt*; Reconstrução da posição; Monitorização do alcance.

Abstract

Hadron therapy has been established as an effective treatment option for tumors, due to the sharp distal falloff, the most important of the Bragg peak properties. However, very accurate particle beam range verification is needed, in order to locate the dose falloff. Prompt gamma imaging is a promising technique based on the detection of promptly emitted photons after the interaction of the incident hadron beam particles and target human tissues. Since the correlation of the prompt gamma emission peaks with the distal falloff was established for hadrons, the use of prompt gamma imaging for therapy monitoring was suggested. The Compton camera provides information to reconstruct the source position of these prompt photons, by using spatial and energetic information from photons and Compton-scattered electrons. Applying the Compton kinematics, one can restrict the source position to an arc segment, thus increasing the source position reconstruction efficiency.

The Compton camera described here consists of a $LaBr_3$(Ce) scintillation crystal as absorber detector, combined with an array of 6 DSSSD (Double-Sided Silicon Strip Detector) as scatter detectors, read out by a ASIC-based readout board. In this project, an optimum energy calibration was performed for the $LaBr_3$ detector, where a relative energy resolution of 2.9% was achieved for E_γ>1.173 MeV. Several spatial resolution measurements were performed, although further investigation needs to be done in terms of spatial resolution.

The full setup of the Compton camera was used in two Tandem accelerator experiments, associated to a 256-channel readout electronics for the PMT (from $LaBr_3$) readout. Several prompt γ ray energy spectra were obtained, where high-energy calibration points were included, allowing for a correct energy calibration of the spectra for E_γ<6.13 MeV.

Keywords: Compton Camera; Hadron Therapy; Prompt gamma imaging; Position reconstruction; Range monitoring.

Contents

List of Figures

List of Tables

Acronyms

ASIC	Application-Specific Integrated Circuit
CALA	Center for Advanced Laser Applications
CSA	Charge-sensitive pre-amplifier
DKFZ	German Cancer Research Institute
DSSSD	Double Sided Silicon Strip Detector
FWHM	Full Width at Half Maximum
GSI, Darmstadt	GSI Helmholtzzentrum für Schwerionenforschung
HZDR	Helmholtzzentrum Dresden-Rossendorf
IARC	International Agency for Research on Cancer
***k*-NN method**	k-Nearest Neighbor Method
LLUMC	Loma Linda University Medical Center
LMU	Ludwig-Maximilians Universität München
LOR	Line of Response
MLL	Maier-Leibnitz-Laboratorium
MAP	Munich-Centre for Advanced Photonics
MARaBOU	MBS and Root Based Online/Offline Utility
MBS	Multi-Branch System
MCFD-16	Constant Fraction Discriminator
MQDC	Charge-to-Digital-Converter
PET	Positron Emission Tomography
RPTC	Rinecker Proton Therapy Center
TUM	Technische Universität München

Preface

The Team and Project Overview

The recently established Chair of Medical Physics, integrated within the group of Experimental Physics, in the Faculty of Physics, belongs to the Ludwig-Maximilians Universität München (LMU). It is a research and teaching group in the field of Medical Physics, located in Garching, about 15 km from the center of Munich, Germany. The main research subjects are pre-clinical and clinical radio- and hadrontherapy for a wide range of beam modalities (such as conventional photon beams, protons and ion beams, and also laser-based systems) [1]. The figure below shows an aerial view of Garching Campus, where the two LMU buildings are placed in the lower right corner.

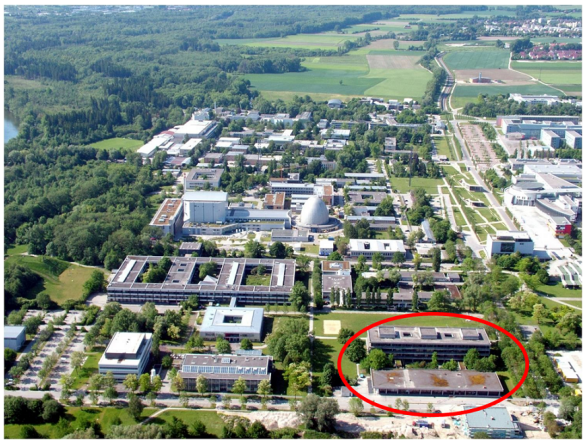

Aerial view of the Garching Campus. The LMU building is located in the bottom right corner.

The supervisor of this project is Prof. Peter Thirolf, one of the lecturers of the department, and the internal supervisor is Prof. Luís Peralta, from the Physics department of Faculty of Sciences. The project is being developed by many institutions working together, such as MAP, the Munich-Centre for Advanced Photonics, a Cluster of Excellence of the German Research Foundation (DFG), LEX/CALA (Laboratory for Extreme Photonics/ Center for Advanced Laser Applications)[2] in Garching, the first dedicated to the development of new coherent light sources and laser-driven particle sources with unprecedented properties, and the second represents the high-power, short-pulse future laser-acceleration center, which is presently under construction. The collaboration also comprises the Technical University Munich and international partners, for example, from TU Delft. These facilities aim at developing laser-driven proton beams for hadron therapy. Complementary technological developments pursued at the Chair of Medical Physics target detector developments for online ion beam range monitoring by

exploiting the emission of prompt γ rays for imaging the Bragg peak.

1

Introduction and Motivation

"Cancer is a group of diseases characterized by uncontrolled growth and spread of abnormal cells. If the spread is not controlled, it can result in death. Cancer is caused by both external factors (tobacco, chemicals, radiation and infectious organisms) and internal factors (inherited mutations, hormones, immune conditions, and mutations that occur from metabolism)" [3].

There are more than 200 types of cancer, each with different causes, symptoms and treatments [4]. Cancer is one of the major causes of death in modern society, ranking second after heart and circulatory diseases [5]. Nowadays, one in eight deaths is due to cancer, causing more deaths than AIDS, tuberculosis and malaria combined. According to estimates from the International Agency for Research on Cancer (IARC), about 13 million new cancer cases emerged in 2008, resulting in a total of almost 8 million deaths. Moreover, factors such as smoking, poor diet and sedentary life promote the increasing number of cancer cases. It is important to notice that about three-quarters of all cases are developed by people with more than 60 years, who represented 10% of the total world population in 2008, and are expected to represent 22% in 2050. This means that in 2050, the number of occurrences worldwide will grow to 33%, assuming that the current rate of incidence remains the same [4].

When the tumors are diagnosed, about 58% have not spread to long distance locations, which means they have not created metastases. Most of the tumors at this stage can usually be treated by local interventions, such as surgery, or by radiation therapy, chemotherapy or a combination of them. Nearly 22% of all cancer patients are cured by surgery, radiation therapy can cure about 12%, while another 6% receive a combination of surgery and

radiotherapy [5]). This is represented in Figure 1.1.

Nevertheless, local treatments in the European Union are not efficient for 18% of all cancer patients, resulting in 280 000 deaths per year. The main reasons behind these numbers are the impossibility of removing the entire tumor or applying a radiation dose sufficiently high to neutralize all cancer cells.

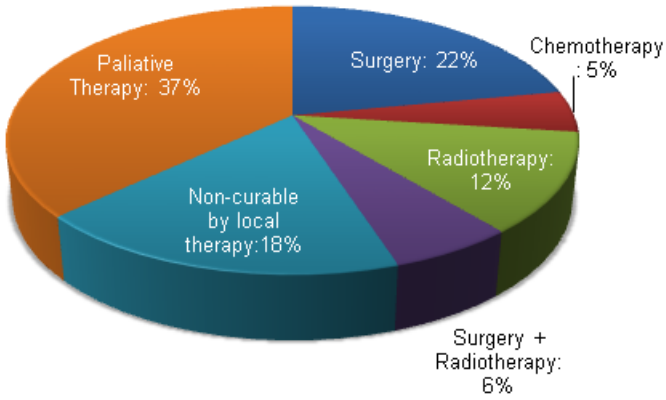

Figure 1.1: Overview of the quantitative distribution of presently used cancer treatment methods (Data from 2008). Adapted from [5].

Then, improving radiotherapy techniques became crucial for successfully cure these patients. Hadron therapy is one of the best examples of the improvement in this field: since December 1997, patients with radioresistant tumors in head and neck have been treated at GSI Helmholtzzentrum für Schwerionenforschung (GSI, Darmstadt), in a collaboration with the Helmholtzzentrum Dresden-Rossendorf (HZDR) and the Radiological Clinic of the University of Heidelberg and the German Cancer Research Institute (DKFZ) in Heidelberg) with high-energy carbon ions and protons - vulgarly called hadron therapy or heavy charged particles therapy. This therapy emerged after several years of radiobiological research and very sophisticated technical development, and it is a subject that still arouses the interest of many people all over the world [6]. Its origin already dates since almost 70 years.

Robert Wilson was an American physicist who, probably more than any other one, is connected to proton radiation therapy. In 1946, after his service to the atomic-bomb project during the World War II, Wilson wrote a seminal paper, suggesting the usage of proton beams for medical treatments, mentioning the therapeutic potential of the Bragg peak [7]. He thought that the depth-dose distribution shown by these particles would be adequate to treat tumors in humans.

Wilson's proposal was innovative, because it identified the mechanisms by which proton radiation treatment would work [7]. Protons demonstrate different dosimetric characteristics than photons, used in conventional radiation therapy. Protons show the characteristic Bragg peak, that is not observed for photons: there is an initial build-up region during which there

is a low and nearly flat energy deposition, but the energy deposition increases along the penetration depth, until it reaches a maximum, the so-called Bragg peak. Then, it falls abruptly to zero, while the conventional photon therapy shoes an exponentially decreasing energy deposition with increasing depth in tissue. This is represented in Figure 1.2.

Because of the Bragg peak, protons and other heavy charged particles reach the tumor at the end of their range and will deposit locally much more energy than photons or electrons (with the same energy), thus causing less damage to surrounding healthy tissue [9].

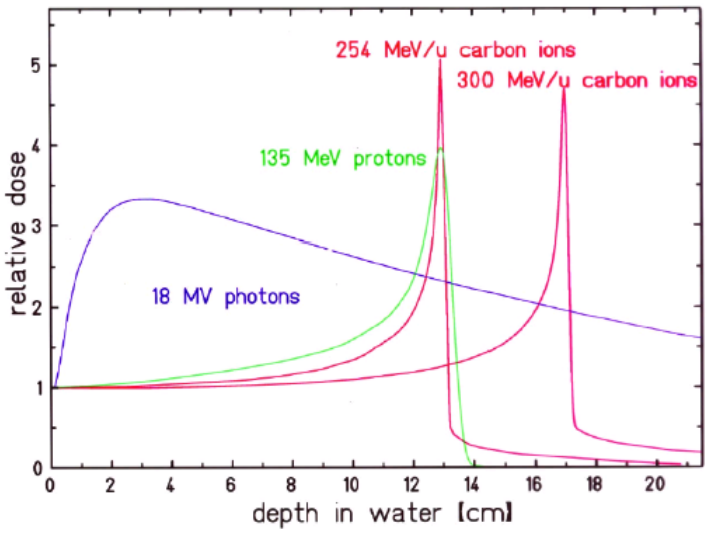

Figure 1.2: Depth-dose profiles for photons, carbon ions and protons [8].

In 1954, radiotherapy with protons started to be an option for cancer patients at the Lawrence Berkeley National Laboratory, after some previous animal experiments [10, 11]. By 1957, proton radiotherapy started being implemented in Europe at the University of Uppsala (Sweden), where some cancers were treated (such like glioblastoma multiform, carcinomas of the cervix, nasopharynx, head and neck)[12, 13]. In 1972, Wilson authorized his colleagues to start the development of a proton therapy facility in Chicago [7].

In 1996, digital imaging was used for the first time at the Proton Treatment Center at Loma Linda University Medical Center (LLUMC) [7]. This technology permitted more rapid verification of patient positioning and set-ups. The 2.000^{th} patient was treated during 1996. In 2001, LLUMC radiation oncologists were treating 150 patients daily with proton beams, and by late summer of that year, the 7500^{th} patient had been treated. Three years later, a successful active scanning proton beam was tested, and a flatpanel digital capability installation materialized at the LLUMC proton therapy center [7, 6].

Nowadays, almost 50 facilities worldwide are operating with protons or carbon ions. Since 2000, about 25 hadron therapy centers started operation, and many more are planned for the forthcoming years. According to J-M. Lagniel [14], since 2000, 5 centers started operation in

Japan, another 5 in America, and 13 in Europe. In particular, the Rinecker Proton Therapy Center (RPTC) in Munich, having started in 2007 treating patients with protons, was visited during the elaboration of this master thesis project [15]. The number of such facilities is growing fast each year, with Europe largely dominating, particularly Germany (5 of the 13 new centers are in located in Germany), mainly because a large majority of the upcoming facilities are being or will be built by specialized companies, since this is a field of therapy and research attracting the interest of industrial companies [14, 16].

1.1 Hadron Therapy

Robert Wilson was a pioneer in the proton beam therapy, having proposed the use of protons for therapy almost 70 years ago. Since then, many facilities for hadron therapy technique implementation have been developed, and many research groups are exclusively dedicated to this field of studies. In 2010, a total of more than 74 000 patients [17] had already been treated using hadron therapy, and this number remains increasing exponentially every year, because hadron therapy is today "part of the medical business landscape" according to J-M. Lagniel [14].

1.1.1 Physical and Radiobiological Rationale

The main rationale for the clinical use of proton and heavy ions beams is the viability of delivering higher and local doses of radiation to the tumor, leading to an increased tumor-control probability (TCP). Then, smaller volumes of healthy tissue are irradiated, increasing the patient's tolerance to the treatment, comparing with some other types of irradiation techniques.

Hadron therapy is particularly interesting and useful in cases of serially organized tissues, where a very small local radiation overdose can cause fatal complication, such as most tumors close to the spinal cord, and some other irregular shaped lesions near critical and delicate structures [18].

Ion beam therapy is a highly conformational irradiation technique. The dose actually delivered to the patient is supposed to correspond to the dose planned by the physicist, but only if there is no deviation between the several used parameters. In order to compensate for

a potential deviation between planned and actual dose delivery, safety margins are applied around the tumor volume during treatment planning, but a very precise verification of the dose is required. Then, real-time monitoring is crucial for these treatments.

Therefore, because hadrons deliver a large amount of energy to the tissue, hadron irradiation is much more sensitive to any variation of beam parameters or patient condition than photon irradiation. At the moment, the dose monitoring is based on the detection of secondary radiation that results from the nuclear fragmentation processes when the beam interacts with the tissue. A new and innovative monitoring technique is being developed, based on the detection of prompt γ rays (photons).

During tissue irradiation, prompt photons are locally emitted by excited nuclei resulting from nuclear reactions, in a very short period of time (shorter than 10^{-12} seconds)[18]. As the correlation between the γ ray emission profile and the Bragg peak position has been established for hadrons [19, 20, 21], it can be used for dose monitoring based on the detection of those prompt γ rays, offering a solution to *in vivo*, non-invasive dose delivery verification.

1.1.2 Challenges and future of Hadron Therapy

It was demonstrated earlier that radiotherapy with hadrons can offer important advantages, but due to the steep dose gradient at the distal edge of the dose deposition curve, the uncertainties in the treatment-planning calculation can cause a serious impact on the location where the dose will be applied to the patient. The sources of uncertainty can be setup errors, organ/patient motion, anatomical changes or even increased density in the tissues. For example, a small increased density can cause the stopping range of the hadron beam to deviate by as much as 2 cm, whereas with photon beams this would not have such a strong influence [22]. This comparison is shown in Figure 1.3, where a small increase in the density of the tissue (grey rectangle) along the penetration depth for 10 MeV photons (solid green curve) causes a relatively small deviation (dashed green curve) but a displacement of the distal edge of the Bragg peak of about 1 cm for protons (difference between solid and dashed blue curves). Here, the blue curves display the clinical situation of applying a "spread-out Bragg peak" (SOBP) across the volume of the tumor, while the reddish curve represents the pristine Bragg peak for monoenergetic protons.

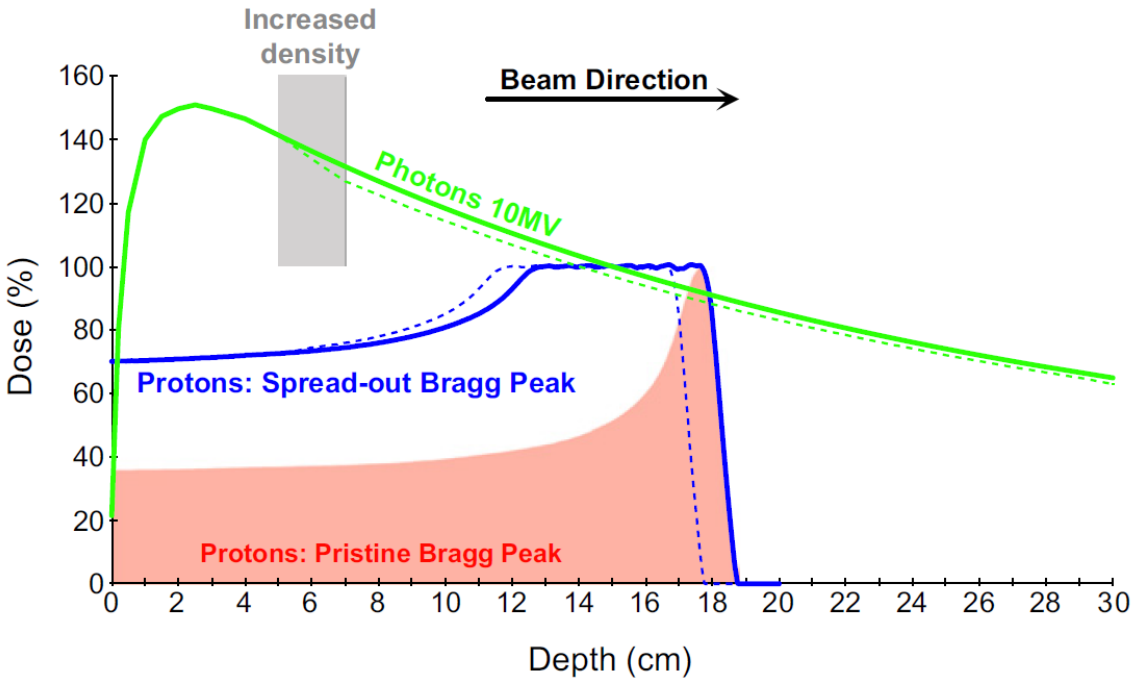

Figure 1.3: Depth-dose distribution for 10 MeV photons (solid green curve) and protons (solid blue curve), and the effect caused by a locally increased density for each case —photons (dashed green curve) and protons (dashed blue curve) [22]. The blue curves denote the spread-out Bragg peak, while the reddish area represents the pristine Bragg peak from monoenergetic protons.

Although thousands of patients have already been treated using protons and carbon ions, about one third of these patients were treated in non-dedicated accelerators, such as nuclear and particle physics laboratories, and less than 2% were treated with pencil beams. Hence, the use of dedicated facilities with high-end technology can lead to an optimum treatment, and thus to a more efficient therapy. The use of Linacs for hadron therapy is also being studied, although it is not yet implemented [23].

At the moment, correction tools and algorithms are not yet developed to accept these deviations and errors and, for example, moving organs, such as lung or stomach, may fluctuate by about 1 cm due to respiration or digestion. In particular, the lung is estimated to move about 10 mm with a frequency of 0.2 Hz [24], what can lead to a deviation of 1-2 cm and spoil the high precision that characterizes hadron therapy. Moreover, if there is a small deviation and (as it happens at most of the treatment centers) the tumor is "painted" with the beam only once, there may be parts of the tumor that are not irradiated, thus leading to a underdosage. This is already a field of research, where different approaches are being studied and

an adequate treatment planning of the dose distribution and the patient positioning play a crucial role.

1.2 Particle beam range verification

As mentioned before, it is mandatory to determine the exact position of the dose distal falloff with 1-2 mm accuracy, because a small overdose can cause complications in surrounding tissues or even damage critical organs at risk.

Therefore, several in-vivo particle beam range verification techniques were or are being developed, comprising, for example, PET [25], γ-PET [26] and prompt gamma imaging [9, 19]. All these methods are based on the detection of secondary radiation, generated by the interaction of the proton (or heavy ion) beam with the human body's constituents. However, secondary photons can be emitted from mainly two different origins: the first category, commonly exploited in Positron Emission Tomography (PET), are the coincident 511 keV γ rays from the decay of positron-emitting isotopes, already referred above. The second source of prompt photons results from the deexcitation of reaction products following nuclear reactions between the impinging therapeutic particle beam and tissue components. These two techniques will therefore be explained in more detail.

1.2.1 Positron emission tomography (PET)

The fundamental principle of the PET technique is the usage of positron-emitting radioisotopes, where the positron travels a short distance (1-2 mm) before suffering annihilation with an electron. From this annihilation result two annihilation photons with 511 keV each, traveling in opposite directions. PET scanners are constituted by a ring of photon detectors (scintillation crystals readout with photomultiplier tubes), allowing for simultaneous photon detection that allows for determining the Line of Response (LOR) that contains the initial (annihilation) event position. Thus the reconstruction of the LOR is performed by means of filtered backprojection or iterative methods. A summary example of a PET system is represented in Figure 1.4.

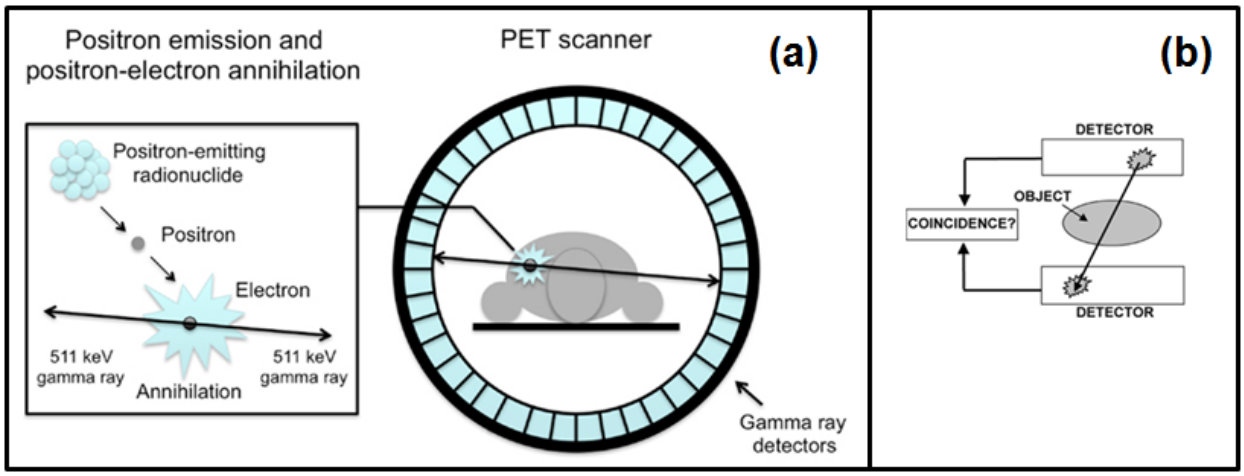

Figure 1.4: (a) Process of positron emission and subsequent positron-electron annihilation, that results in two (almost back-to-back emitted) 511 keV photons, and schematic drawing of a PET scanner consisting of a ring of segmented scintillation crystals. (b) When the photons are detected in a ring of small scintillation crystals, the detection locations define a line of response (LOR), along which the decaying nucleus was located . Adapted from [27, 28].

At the present, PET is the only method in clinical practice for monitoring and verification of the delivered dose during hadron therapy [25]. Exploiting the decay characteristics of β^+ emitting isotopes for the localization of the ion beam range in hadron therapy could in principle be performed in two ways: at present, exclusively stable particle beams (proton and carbon ions beams) are used as therapeutic beams, and β^+ emitting isotopes are exploited as reaction products from the interaction of the impinging primary beam with the human tissue constituents (represented in Table 1.1). However, in fundamental nuclear research, the use of radioactive ion beams, made available by large-scale research infrastructures during the past 30 years with ever increasing intensities, has opened completely new fields of research. Therefore, it is quite straightforward to think about the therapeutic use of such radioactive ion beams, in particular from β^+ emitting species like ^{14}O, ^{10}C or ^{11}C. Indeed, such proposals have been put forward in particular in Japan [29, 30, 31]. However, so far no facility has provided β^+-unstable ion beams for hadron therapy. One reason being the typically limited beam intensity of radioactive isotope beams. Nevertheless, in the meanwhile these beams have reached a quality that may allow their therapeutic use in the near future, which would significantly boost the diagnostic sensitivity of beam-range verification via PET (or γ-PET, in section 1.2.3).

During hadron therapy, positron (β^+) emitters are produced in the patient's body, due to nuclear reactions —when the ions of the incoming beam collide with the atomic nuclei of

the irradiated tissue, β^+ emitters may be produced amongst the resulting reaction products. Thus the impinging particle beam activates tissue components along the beam path. The subsequently emitted 511 keV photons from positron annihilation will be detected by a PET scanner, either during or after the treatment (depending on the positron emitters half-life, which is 20 minutes for ^{11}C, 2 min for ^{15}O and 19 seconds for ^{10}C) [32]. Some examples of the main reaction channels for β^+ emitter production in the human body during a proton beam irradiation are listed in Table 1.1.

Reaction	**Threshold energy [MeV]**	**Half-life [min]**	**Max. positron energy [MeV]**
^{16}O(p,α)^{13}N	5.66	9.97	1.19
^{14}N(p,pn)^{13}N	11.44	9.97	1.19
^{14}N(p,α)^{11}C	3.44	20.39	0.96
^{12}C(p,p2n)^{10}C	34.5	0.32	1.87
^{16}O(p,3p4n)^{10}C	39.1	0.32	1.87
^{14}N(p,n)^{14}O	6.6	1.18	1.81
^{16}O(p,p2n)^{14}O	30.7	1.18	1.81

Table 1.1: Main reaction channels for proton-induced β^+ emitters produced in human tissue [32].

In Table 1.1, the first 3 reactions account for 95% of the β^+ emitter production, while the 4 last reactions lead to reaction products, which are β^+-unstable but will emit another, third, prompt photon from an excited state. They allow for applying the novel "γ-PET technique" (see Section 1.2.3).

Currently, "conventional" PET scanners offer an accurate position reconstruction, with a position resolution of the order of ∼4—5 mm [33]. However, the new and improved methods like time-of-flight (TOF) PET use the time-of-flight difference between the two annihilation photons to improve the localization of the annihilation position, then they may offer a more accurate PET scanner measurement (with an improved position resolution of about 2 mm). Basically, using this information, one can constrain the two-photon emission point to a particular segment along the LOR, as shown in Figure 1.5. The TOF reconstruction method reduces the noise propagation along the LOR during the reconstruction, thus the TOF images show a lower level of noise and better resolution when compared to equivalent non-TOF images [34].

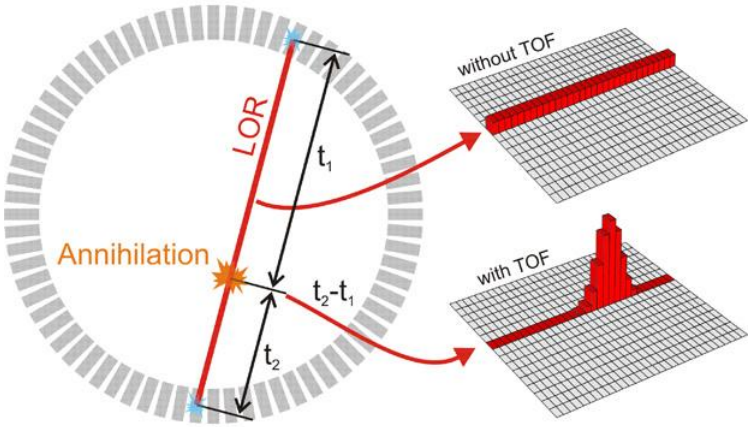

Figure 1.5: TOF-PET line of response, where the conventional two-photon emission point can be constrained to a particular segment along the LOR [35].

Since there is no direct correlation between the PET image and the dose distribution, the image is then compared with dose distributions of positron emitters as derived from Monte-Carlo simulations. However, this technique has several limitations, such as long delay times between treatment and PET scan (which leads to a reduced signal), biological washout effects due to the metabolism or even a change of the patient position. An improvement could be reached by implementing online PET imaging, or other more sensitive methods, such as online prompt-gamma imaging [25], the latter being the motivation for the project being reported here.

1.2.2 Prompt gamma imaging

Not only PET can be used as an online treatment monitoring and ion beam range verification technique. A new innovative technique called prompt γ imaging bears the potential of a promising alternative to PET, since the prompt γ rays are emitted almost immediately ($\sim 10^{-12}$ s) after the interaction of the ion beam with the tissue. These prompt γ rays are produced by inelastic interactions of incident protons (or heavy ions) and target nuclei, where the reaction product is excited to an energetically higher lying-state and subsequently emits one or more photons during deexcitation to the ground state.

The prompt gamma emission peaks were suggested to correlate with the distal falloff [36], and this matter was studied by C-H. Min et al. [19] in 2006, thus leading to investigate the use of prompt gamma imaging for therapy monitoring. Several studies [9, 19] allowed to reveal that the prompt gamma rays generated by several nuclear reactions within the human

body can be used for dose verification. Since it could be shown that the prompt gamma distribution is correlated with the distal falloff of the Bragg peak and that the emission profile is directly correlated to the primary beam range, this allows for beam path reconstruction (longitudinal distribution) and delivered dose determination [21].

Todd et al. [37] proposed the usage of a gamma camera to detect Compton scattered photons, in order to replace the conventional mechanical collimator with a second detector, working as an electronic collimator for the Compton scattered photons, by detecting two photons in (time) coincidence. In 1983, Singh and Doria [38] built the first Compton camera device with medical purposes, by replacing the gamma camera mechanical collimator with a germanium detector as scatter detector and the NaI crystal of the gamma camera as absorber detector. After this pioneering work, several Compton camera designs have been proposed, and are now being studied by several groups worldwide for medical purposes, which is also the aim of the present project [39, 40, 41, 42].

Then, the development of a Compton camera prototype for position-sensitive detection of prompt γ rays resulting from nuclear reactions after hadron irradiation is the aim of this project. The Compton camera operates by exploiting the Compton effect, offering many advantages such as wide field of view, the ability to reconstruct 3D images without tomography, and the absence of heavy collimation. In this camera, an absorber detector and a scatter detector are used, and these detectors are able to reconstruct the γ source position using the Compton scattering kinematics, and the Compton-scattered electrons.

1.2.3 γ-PET

After introducing the concept of PET technique in Section 1.2.1 and the concept of the prompt gamma imaging in Section 1.2.2, the principle of a Compton camera will later on be described in detail in Section 2.5. The γ-PET technique lies on the combination of the Compton camera principle, together with the usage of positron-emitting isotopes.

In Table 1.1, several β^+ emitters were presented. As mentioned above, the particularities of the 4 last reactions are their reaction products, β^+-unstable nuclides that will decay and emit a third photon from the deexcitation. In particular, ^{10}C and ^{14}O are adequate to apply the "γ-PET" technique during proton irradiation, in spite of having short halflives (of 19.3 and 70.6 s, respectively) [26].

The γ-PET technique uses the capabilities of the Compton camera to additionally detect a

LOR defined by the two 511 keV annihilation photons resulting from the β^+ decay (shown in Figure 1.6).

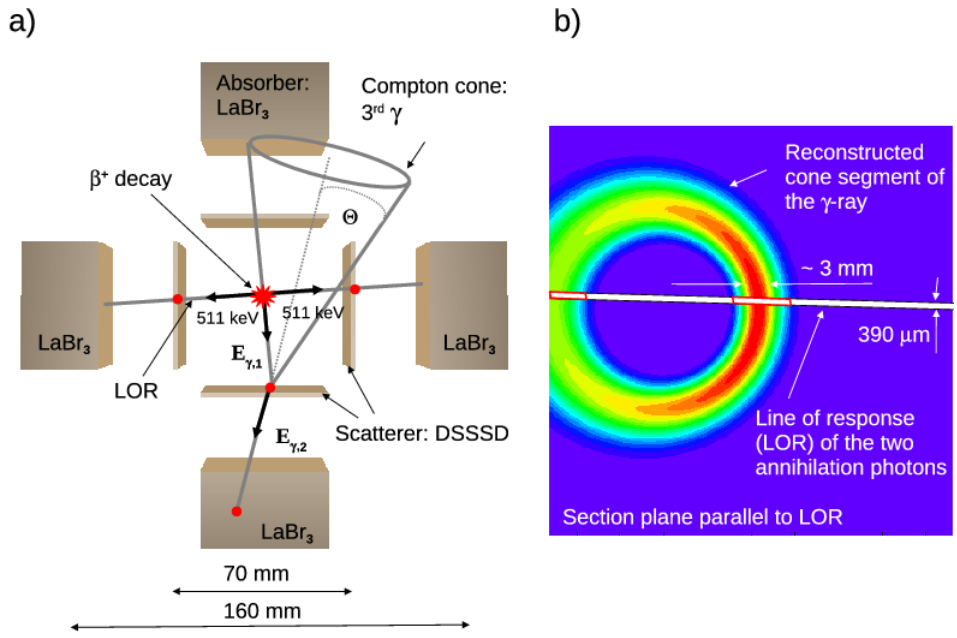

Figure 1.6: (a) Principle of the γ-PET technique using 4 Compton cameras,; (b) The intersection of the Compton cone and the LOR strongly suppresses background and restricts the reconstructed events to those belonging to the same β^+ γ coincidence event [26].

This novel technique exploits the triple (time) coincidence between the two annihilation photons and a third prompt photon, enabling to separate the reconstructed "true" events from the background events and allow for a significantly improved sensitivity. It was found [26] through Monte-Carlo simulations that making use of triple-γ coincidence, one is able to reach sub-millimeter spatial resolution in 3 dimensions for a small-animal irradiation scenario.

2

Basic Considerations

The operation of a radiation detector mainly depends on the interaction processes of the radiation with the material of the detector itself, and it is necessary to understand how the radiation interacts with certain materials. Moreover, it is convenient to know the major categories of radiation:

- Heavy charged particles;
- Fast electrons;
- Neutrons;
- X-rays and gamma rays;

The two first species represent charged particles that interact via the Coulomb interaction with (predominantly) the electrons of the medium they are penetrating. The two last species represent uncharged types of radiation. Photons still interact via the electromagnetic interaction, while neutrons involve the strong interaction, or nuclear force. This results either in total or partial energy transfer from the incident particle or photon to the target or detector (more specifically to its electrons or nucleons) or to charged particle products of nuclear reactions. If no interaction occurs in the detector material, these neutral types of radiation can pass through the detector without depositing any energy.

Moreover, when X-rays or γ rays interact within the detector material, they can generate secondary photons or electrons. The interaction of neutrons can also generate a variety of secondary reaction products, ranging from (heavy) charged particles to electrons or γ rays.

These secondary electrons or the (heavy) charged particles contribute to the output signal that can be detected afterwards.

Heavy charged particles are considered as the group of particles where mass is equal or heavier than the proton mass, including alpha particles, protons, and any other energetic heavy particles that can be produced as a particle beam in an accelerator, or as reaction product following a nuclear interaction [43]. In this work, we will focus specifically on photon detection from proton-induced interactions.

2.1 Photon interactions with matter

In this section the possible basic interaction processes between photons and matter will be briefly introduced, since for the present project one is particularly interested in such effects, and specifically in exploiting the Compton effect for prompt γ medical imaging. However, the other two main processes will also be briefly described, since they are relevant for the analysis and interpretation of data that will be discussed afterwards. The three main processes that play an important role in γ ray detection are the photoelectric effect, the Compton effect and pair production. All of these three processes involve energy transfer from incident photons to secondary electrons. Figure 2.1 shows the regions of dominance of these three processes of photon-matter interaction as a function of the energy of the photon E_γ and atomic number Z of the absorber material.

In Figure 2.1 are shown the domains of the three major photon-matter interaction processes, with the lines for silicon and germanium marked. It can be observed that the energy range of the Compton scattering process is larger for silicon (60 keV to 15 MeV) than for germanium (150 keV to 9 MeV).

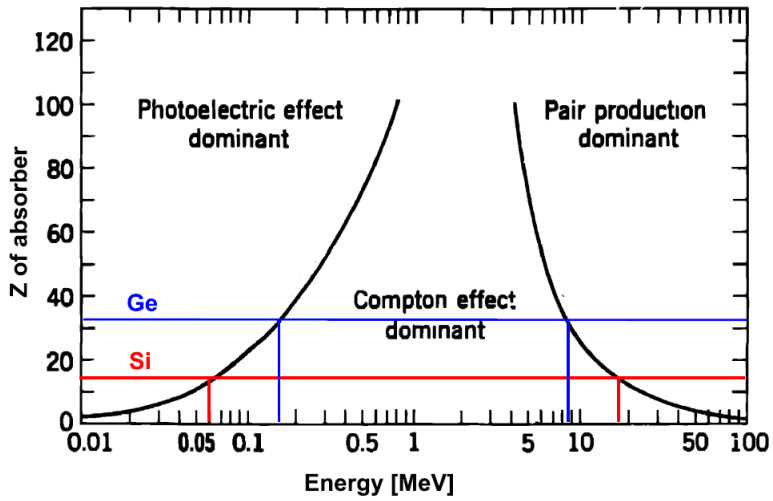

Figure 2.1: Regions of dominance of the three main processes of interaction between photons and matter, for several photon energies E_γ and atomic numbers Z of the absorbing material. The element silicon, acting as scatter detector in the experiments described here, is marked with a red line, where the predominance of the Compton effect is visible for γ ray energies between 60 keV and 18 MeV. Adapted from [43]

2.1.1 Photoelectric Effect

The photoelectric effect is the dominant process for relatively low γ ray energies, where an incident photon ejects an electron from the target or detector material, called photoelectron. The kinetic energy of the photoelectron is given by $E_{e^-} = E_\gamma$ - E_b, where E_γ corresponds to the energy of the incident photon and E_b is the binding energy of the photoelectron in the detector material. For relatively low energies, the electron carries most of the initial photon energy. The probability (cross-section) σ of photoelectric absorption per atom, outside the resonances, can be approximated by:

$$\sigma \cong constant \times \frac{Z^n}{E_\gamma^{3.5}} \tag{2.1}$$

where n varies between 4 or 5 as a function of the γ ray energy. For instance, this strong dependence of the γ ray absorption on the atomic number (and on the density) is what makes lead (and other high-Z materials) a good shielding material [43]. It should be noted, that due to the requirement of simultaneous energy and momentum conservation, the photoelectric effect is forbidden to occur with a free electron. Thus, the photoelectric effect is an interaction

between the photon and the atom.

2.1.2 Pair Production

The pair production process consists of the production of an electron-positron pair, following the incidence of a photon onto target or detector material. Subsequently, the positron slows down in the medium during a short period of the order of picoseconds via collisions, and annihilates with a bound electron, producing two annihilation photons, each with an energy of 511 keV. The probability of pair production increases with energy, starting from a threshold given by twice the rest-mass energy of an electron (1.02 MeV).

2.1.3 Compton Effect

The photoelectric effect is the dominant effect for low-energy γ rays, typically in silicon or germanium, below about 60 keV. For higher γ ray energies, as they are typical for the deexcitation of radioisotopes, or for the positron annihilation following β^+ decay, the Compton effect is dominating. This process is schematically illustrated in Figure 2.2.

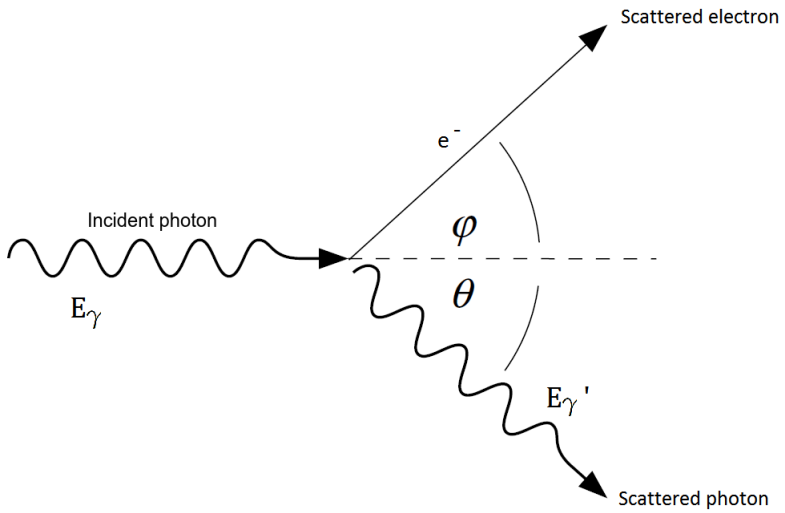

Figure 2.2: Schematic diagram of the Compton effect.

The Compton effect proceeds via a scattering of an incident photon, with energy E_γ, from a free electron considered to be at rest in the material. The photon transfers part of its energy to the electron as kinetic energy. After the interaction, the photon has a final energy of

$E_{\gamma'} < E_\gamma$, is scattered under an angle θ relative to the original direction, while the electron scattering angle is ϕ. The energy $E_\gamma^{'}$ and scattering angle θ of the photon can be derived in a straight-forward manner from the requirements of energy and momentum conservation as:

$$E_{\gamma'} = \frac{E_\gamma}{1 + (E_\gamma / m_e c^2)(1 - cos\theta)} \tag{2.2}$$

where m_e is the electron mass. Moreover, the lowest energy attainable for the scattered photon after the scattering process corresponds to the energy resulting for a scattering angle of 180° according to:

$$E_{\gamma'}^{\min} = \frac{E_\gamma}{1 + 2(E_\gamma / m_e c^2)} \tag{2.3}$$

Hence, the energy of the photon is converted into electrons' kinetic energy, which lose their energy by creating scintillation photons in a crystal or electron-hole pairs in a semiconductor detector (Section 2.4.1). From equation 2.2, and by conservation of the total energy, the kinetic energy E_e of the Compton electron can be related to the photon energy as:

$$E_e = E_\gamma - E_{\gamma'} = \frac{E_\gamma^2 (1 - cos\theta)}{mc^2 + E_\gamma (1 - cos\theta)} \tag{2.4}$$

since $E_\gamma - E_{\gamma'}$ is the energy transferred inelastically by the photon to the electron. Thus, while in the backscattering process ($\theta = 180°$) the electron receives its maximum kinetic energy, the minimum energy transfer to the electron is realized for the forward scattering at $\theta = 0°$ [44]. The scattered electrons can be scattered in angles from θ=0 °to θ=180, and will typically be absorbed in the scatter detector. Thus they contribute to the response of the detector, in particular to the Compton continuum, ranging from zero to the Compton edge (Figure 2.3). This continuum is not constant because, according to the Klein-Nishina formula, the Compton scattering probability varies with the scattering angle.

The probability for Compton scattering at an angle θ is determined by a quantum mechanical calculation starting from the Dirac equation. Thus the differential cross-section for Compton scattering per electron is given by the Klein-Nishina formula:

$$\frac{d\sigma}{d\Omega} = r_0 \left[\frac{1}{1 + \alpha(1 - cos\theta)} \right]^3 \left[\frac{1 + cos\theta}{2} \right] \times \left[1 + \frac{\alpha^2 (1 - cos\theta)^2}{(1 + cos\theta)[1 + \alpha(1 - cos\theta)]} \right] \tag{2.5}$$

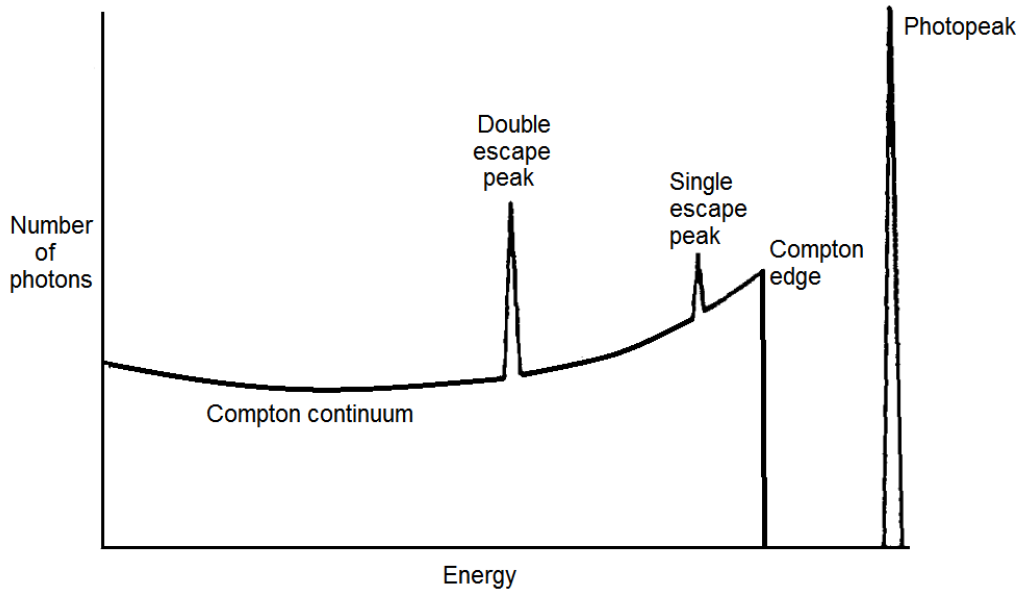

Figure 2.3: The response of a radiation detector to monoenergetic γ rays [43].

Figure 2.3 shows a schematic representation of a typical γ ray energy spectrum for monoenergetic photons ($E_\gamma > 1.02$ MeV) registered with a radiation detector. First, it exhibits the photopeak at the initial photon energy E_γ, where the complete photoelectric absorption occurs, and the single- and double-escape peaks which correspond to the occurence of pair creation, with subsequent escape of one or both 511 keV photons from the positron annihilation. The pair-production process, as previously described, leads to the creation of two annihilation photons each with an energy of 511 keV. These two photons can either be completely absorbed (and thus registered as a part of the photopeak), or can undergo Compton scattering (then contributing to the Compton continuum with other Compton-scattered photons). Finally, when both 511 keV photons escape from the detection volume (double-escape), the double-escape peak will be generated with an energy E_γ-$2mc^2$, while in case of only one photon escaping from the detector(single-escape), the single-escape peak will be observed with an energy E_γ-mc^2.

Finally, Figure 2.4 shows the linear attenuation coefficient of gamma radiation in matter ($LaBr_3$), composed of the contributions from the three main processes just discussed.

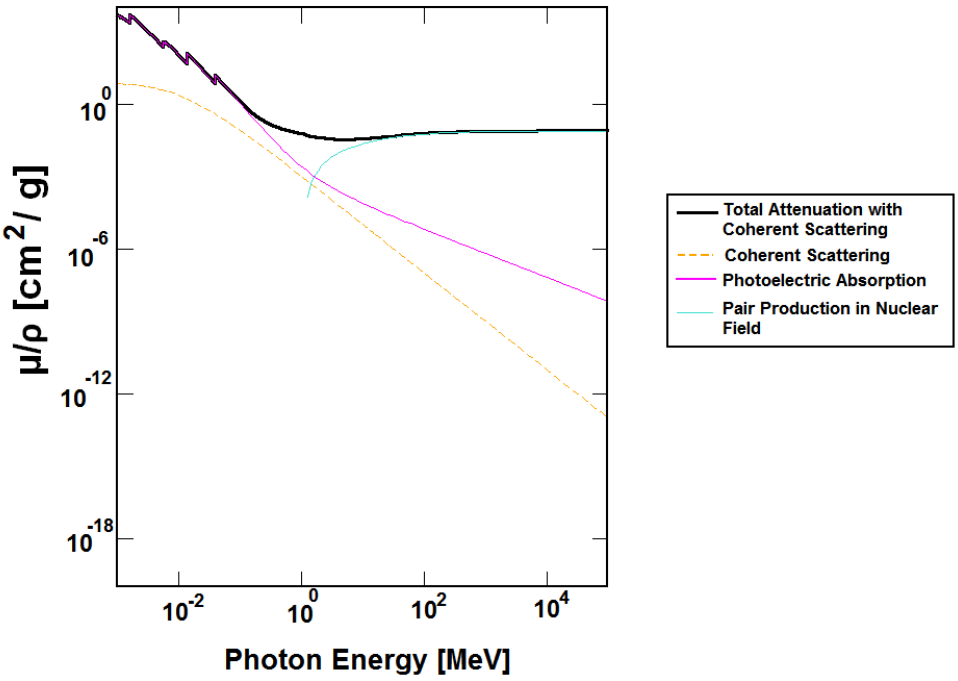

Figure 2.4: Mass attenuation coefficient for photon radiation in $LaBr_3$, composed of the contributions from the Coherent scattering, photoelectric absorption and pair production. Obtained from [45].

2.2 Proton-induced nuclear reactions in a water phantom

It is well known that up to 60% of the human adult body consists of water (oxygen and hydrogen atoms) [46], besides carbon ($\sim$ 19%) and nitrogen ($\sim$ 4%) [47] (and other elements in small percentages). Within human tissue, or in tissue-equivalent water phantoms, the prominent nuclear reactions involve hydrogen, oxygen or carbon nuclei [48], since they are the most abundant atoms in human tissue. The resulting characteristic prompt γ ray spectrum is then originating from the γ ray emission from nuclear transitions that occur from these nuclei to the prominent lines of:

- 2.2 MeV photons from the fusion reaction $^{1}H(n,\gamma)^{2}H$;
- 5.11 MeV photons from $^{14}N^{*}$ following the ^{16}O (p,p2n) $^{14}N^{*}$ reaction;

- 4.44 MeV photons originating from the deexcitation of the first excited state of ^{12}C;

- 6.13 MeV photons from the deexcitation of the first excited state in ^{16}O [48].

In order to allow for a comparison of the measured prompt γ ray energy spectrum with the expectation from Monte-Carlo simulations, in Figure 2.5(a) the scenario as used in our beam experiment at the Garching Tandem accelerator was simulated with GEANT4 [48]: 20 MeV protons impinge onto a water phantom (box with $1\times1\times5$ cm^3, the old water phantom). The resulting γ ray energy spectrum is shown in Figure 2.5(a), where the prominent lines are marked and their assignment is indicated.

A scenario more closely related to a therapeutic proton beam is shown in Figure 2.5(b), where a FLUKA [48] simulation is shown for 100 MeV protons bombarding a water phantom with a cylindric volume of 50 cm (length) and 10 cm of diameter.

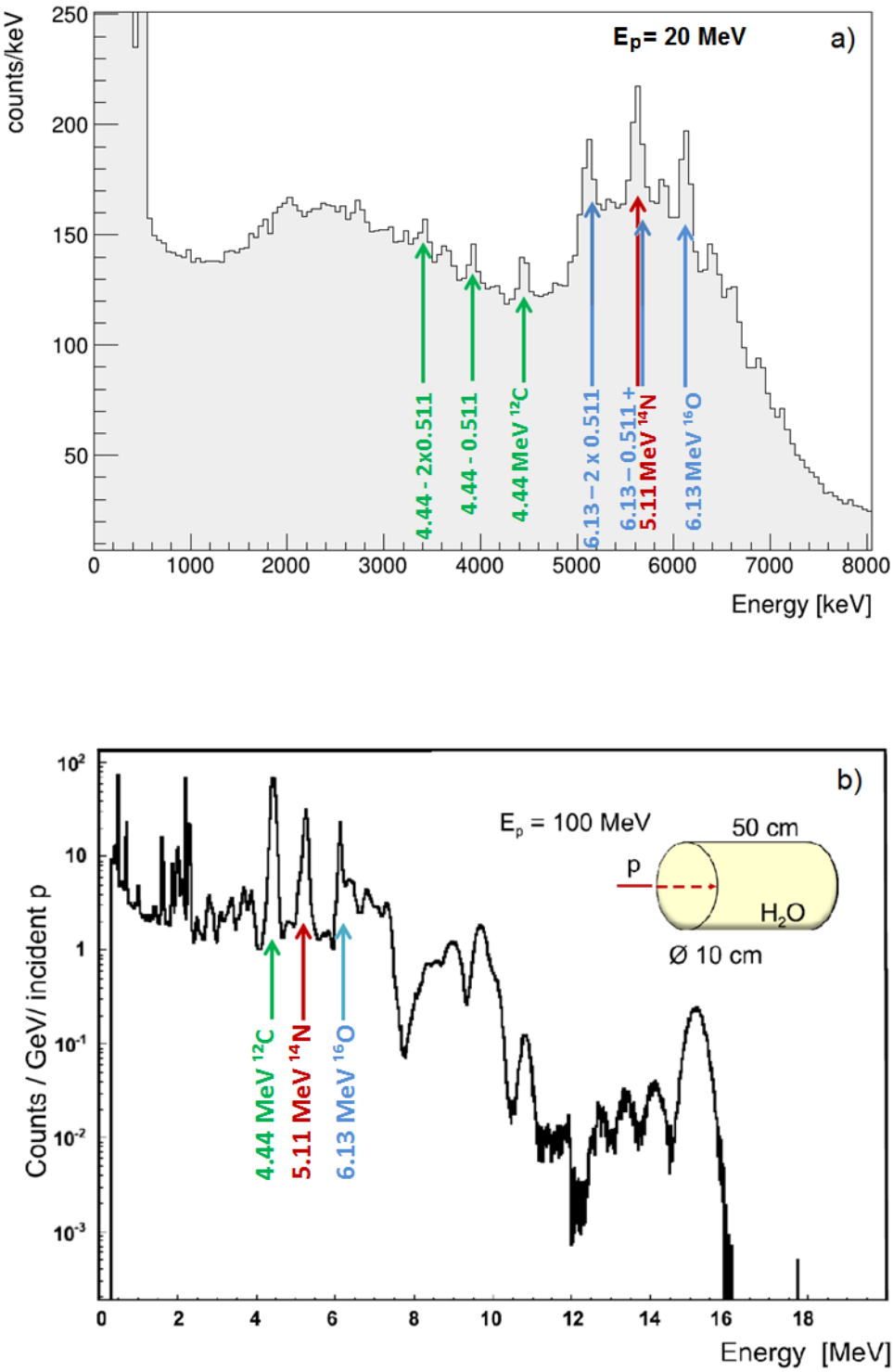

Figure 2.5: (a) γ ray energy spectrum from a GEANT4 [48] Monte-Carlo simulation, with 20 MeV protons hitting a water phantom ($1\times1\times5$ cm^3). (b) γ ray energy spectrum resulting from a Monte-Carlo FLUKA simulation [48] with 100 MeV protons impinging onto a cylindrical water phantom.

The γ ray energy spectra exhibit photons up to a maximum energy of about 16 MeV, again dominated by the strong transitions from reactions with the most abundant organic elements as discussed here. Namely, in Figure 2.5(a), the 4.44 MeV ^{12}C line (from the deexcitation of the first excited state of ^{12}C), as well as the corresponding single- (4.4-0.511 MeV) and double-escape (4.44-2×0.511 MeV) peaks, are drawn in green. In blue, the 6.13 MeV ^{16}O line from the deexcitation of the first excited state in ^{16}O, as well as the single-escape (6.13-0.511 MeV) and double-escape (6.13-2×0.511 MeV) lines are displayed. In Figure 2.5(b), the main lines are found again at 4.44 MeV (^{12}C), 5.11 MeV(^{14}N) and 6.13 MeV(^{16}O), overall showing prompt γ rays with energies up to 16 MeV.

2.3 Proton acceleration

The electrostatic Tandem Van-de-Graaff accelerator in Garching was used to accelerate the proton beams for our experiment. In general, particle accelerators use electromagnetic fields to accelerate charged particles, such as ions, electrons, or alpha particles. The "Tandem" principle (see below) allows for making efficient use of the acceleration voltage in 2 stages. Although this is a conventional facility, the Van-de-Graaff accelerator allows for obtaining rather high acceleration voltages. The Garching machine can reach a terminal voltage of up to 14 MV.

In this method, negative ions are first produced in an ion source and then accelerated towards a central electrode (the so-called terminal) at high positive potential in an evacuated glass tube, surrounded by a steel pressure vessel filled with (6 bar) of SF_6 as (inert) damping gas to prevent HV discharges. Inside the terminal, the negative ions pass through a stripper foil ($\sim$4 μg/cm^2 carbon foil), where the ions are separated from part of their electrons, producing a positive ion beam. This positive beam will then be accelerated in the second half of the accelerator, away from the central terminal electrode, towards the target. Due to the maximum terminal voltage of 14 MV, the maximum proton energy available at the Garching Tandem accelerator is limited to 28 MeV.

A completely new and radically different method to accelerate proton beams is using high-power, short-pulse lasers, called laser-accelerated proton beams [49]. When these beams interact with tissue or phantoms, they will cause the emission of multi-MeV prompt gamma rays, in the same way as from conventionally accelerated proton beams. However, the goal is to achieve larger acceleration fields, a much more compact (and thus more cost-efficient)

accelerator for biomedical applications, in particular for future use in hadron therapy. "The generation of such proton beams is one of the goals pursued within the Munich-Centre for Advanced Photonics (MAP) Cluster of Excellence and the upcoming Center for Advanced Laser Applications (CALA) facility in Garching" [2]. CALA is presently in its construction phase since June 2014 and is expected to start operation in 2017. The new CALA facility will have a total of 1600 m^2 experimental areas, 500 m^2 office space and 600 m^2 laboratory space. The total cost of this facility will be about 80 million euros, and it will be co-financed by the state of Bavaria and the German federal government.

The production and position-resolved detection of energetic prompt γ rays from proton-induced nuclear reactions with organic elements is one of the aims of LMU research group, because they carry important information about the beam trajectory and particularly about the position of the Bragg peak in tissue (or in equivalent phantoms). This information allows for verifying the stopping range and position of the proton beam, providing an improved therapy monitoring capability [1]. Besides the economical advantages of laser-driven particle acceleration, further advantages of such laser-driven ion beams (where presently ca. 5 GeV electron beams [51], 170 MeV proton beams or 200 MeV/u carbon beams [52] have already beam accomplished) are mainly lying into the field of ultrafast time-resolved radiation biology, and in the future also tumor therapy with laser-accelerated particles is envisaged.

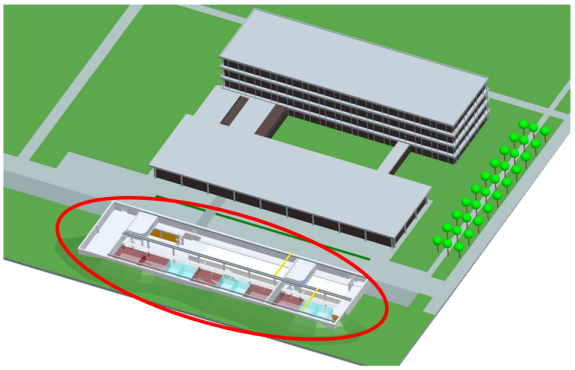

Figure 2.6: CALA building construction plan [50]. The upper (grey) buildings denote the existing LMU buildings on the Garching campus, while the red ellipsis indicates the CALA facility, presently under construction.

2.4 Photon Detectors

In order to ensure that the correct dose is delivered to the patient during a hadron therapy treatment, the dose distribution delivered by the beam has to be measured with, for example, radiation detectors. Most radiation detectors follow a similar principle: the radiation reaches the detector, interacts with the atoms that compose the detector material, induces some

energy loss, thus occurring ionization process. The resulting signal from this ionization pairs is then collected and detected, forming an electric pulse that is transmitted to the signal processing electronics of the experimental set-up [44]. In general, dose distributions can be measured using (gaseous) ionization chambers, semiconductor detectors, scintillation detectors, or passive detector systems like radiochromic films. In this section, we will focus on semiconductor and scintillation detectors.

2.4.1 Semiconductor Detectors: Silicon Strip Detectors

A semiconductor detector consisting of silicon or germanium is made of atoms with a diamond lattice structure, connected by covalent (tetrahedral) bonds to nearest neighbors. When a material shows such lattice structure, the electrons occupy certain bands in the material. These two bands are called valence band (the next band energetically above the last fully filled band) and conduction band (the lowest completely empty band at zero temperature), and are separated by a band gap: a range of energies that the electrons cannot assume. For semiconductor materials, this band is well defined and is in the order of ∼1-2 eV (for Ge: 0.67 eV and for Si: 1.12 eV) [53]. The number of free charge carriers that exist in an intrinsic semiconductor is not enough for its usage in the manufacturing of electronic devices. Then, when producing such devices, the conductance properties of the intrinsic semiconductors are modified by doping processes, thus obtaining the respective extrinsic semiconductor. An extrinsic semiconductor can exist in two forms: p- or n-type, according to the used dopant (or impurity).

Typically the semiconductor detectors are made of silicon or germanium. In this thesis, we will focus on silicon detectors and even more specifically to position-sensitive silicon strip detectors. Here, the electrical conductance near the electrical contacts is enhanced by doping with selected donors or acceptors. Besides the typical n-type bulk material, position sensitivity can be achieved by structuring one or both sides of the detector, for example, via parallel, insulated strips [54]. Each of these strips finally is operated as an individual detector, depending on the dopant implanted to the respective contact plane before segmentation, p or n-type strips can be created.

A semiconductor detector behaves as a diode, following the principle of reverse biasing. Since the diode comprises a p-n junction of two semiconductor materials (acting, respectively, as anode and cathode), there will be a momentary flow of electrons from the n- to the p-side,

thus a third region called depletion region is created, and in this region there is an absence of free charge carriers. When an external voltage (with the same polarity as the built-in potential) is applied to the diode, the depletion zone will act as an insulator, since no charge carriers will flow in this region. This is called the principle of reverse biasing [55, 43]. This can be used to increase the depletion layer width, so that in the extreme case there are no free charge carriers in the entire detector [53]. Thus an ionizing radiation that generates free charge carriers can be detected. The applied voltage separates the charge carrier-pairs and causes their drifts to the electrodes, so that a current pulse is generated and, after amplification, can be detected by the readout electronics.

The silicon detectors can be manufactured in several forms: unstructured silicon diode detectors, with thicknesses in the order of up to $\sim$ 1 mm, and sizes in the order of typically several cm^2, that only contain an n- and a p-contact, and are used for X-ray spectroscopy and γ ray spectroscopy (see left panel in Figure 2.7). Structured silicon diode detectors, such as single-sided strip detectors, have an n-contact and p-strips, with several cm^2 of size and larger thicknesses, and are used for particle and photon tracking (middle panel in Figure 2.7). Double-sided strip detectors, finally, show orthogonal p- and n-strips, enabling n^2 resolution elements with 2·n readout channels (right panel in Figure 2.7).

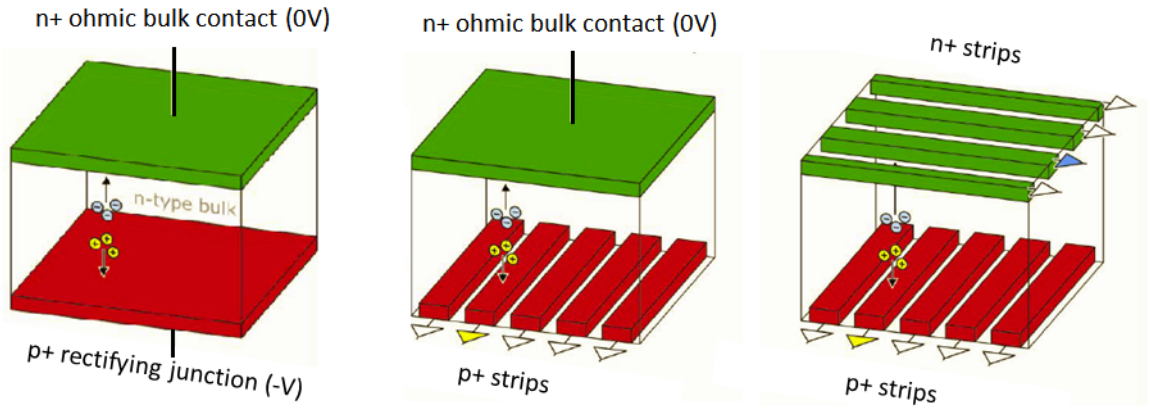

Figure 2.7: Sketch of an unstructured silicon detector (on the left), a single-sided strip detector (in the middle) and a double-sided strip detector (on the right) [56].

Semiconductor detectors usually exhibit small leakage currents, low noise in operation at room temperature, a good energy resolution, a high spatial resolution and high quantum and detection efficiency [56]. The reason why silicon was chosen over germanium for this

particular project of the Compton camera, is related to the scattering properties of silicon, which are favorable for our purposes, using the Compton scattering kinematics. The comparison between silicon and germanium properties is represented in Figure 2.8.

The DSSSD is a type of semiconductor detector which allows to detect the position of incident radiation (particles or photons) with a very high accuracy, via its 2D segmentation. Silicon is a semiconductor, that can be manufactured in two forms: n-type (with an excess of electrons), the most used, and the p-type (with a deficit of electrons). The bulk of the Silicon strip detectors (with typical thicknesses between 100 μm and 2 mm) is made of n-type material. In case of a 1D segmented single side strip detector, its back side is covered with an aluminum electrode along its complete surface, while its front face is segmented into p-type silicon strips. These strips are electrically insulated from each other, and an electric field is applied between the p-strips and the back-side contact. When ionizing radiation hits the detector, charge-carrier pairs (electrons and holes) are created in the depleted bulk of the detector. These free charge carriers drift in the externally applied electrical field towards the electrodes, where they are collected. The electrons drift towards the (grounded) n^+ contact (here consisting of the aluminum contact of the back side of the detectors) while the holes drift towards the p-strips. It should be noted that an electrical signal is generated at the cathode and anode contacts not just after arrival and collection of the charge carriers at their respective electrodes, but already during their drift time via induced charges. The interaction of a γ ray with the atoms of the DSSSD is shown in Figure 2.9, where an external voltage is applied.

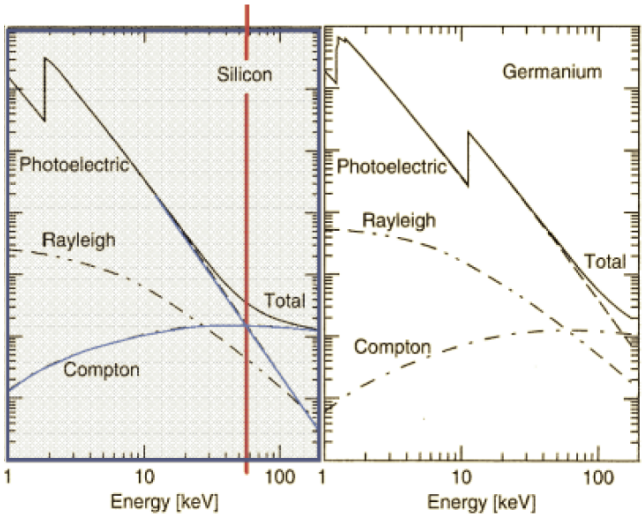

Figure 2.8: Comparison between Silicon and Germanium, for photoelectric and Compton processes probability [56].

The aluminum contact strips are connected to readout channels, which are very sensitive to charge changes. Analyzing the hit pattern of responding detector strips allows to derive the position of incidence of the primary radiation (charged particles or photons) impinging onto the detector. Segmenting also the n^+ back-side contact of the silicon detector into individual strips (with orthogonal orientation relative to the front-side segmentation), finally leads to the 2D-segmented double-sided silicon strip detectors (DSSSD) as used in our project, shown in Figure 2.10.

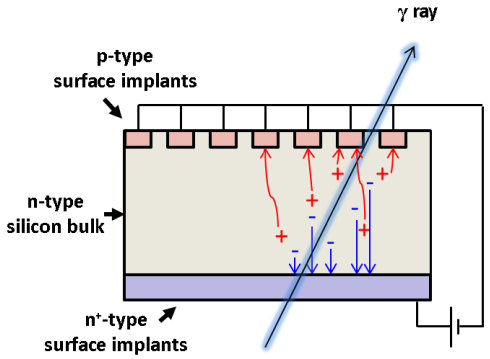

Figure 2.9: Sketch of the side view of a DSSSD, where an interaction of an incoming γ ray is visible inside the detector. The charge carrier generation and flow are also displayed [53].

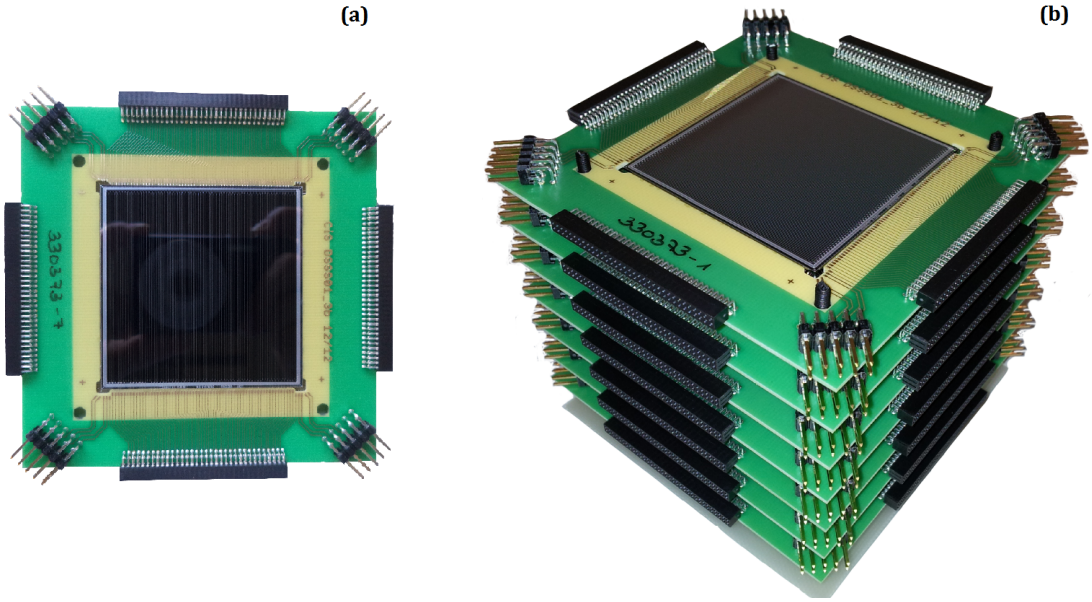

Figure 2.10: (a) Top view of one DSSSD module of the tracker array; (b) Tracker array consisting of 6 DSSSD modules (one extra spare detector is shown in the photograph), separated from each other by 1 cm.

Using double-sided silicon strip detectors allows to track charged particles or photons. Every time an incident particle or photon hits the detector, a signal is generated on one of the p-side and one of the n-side readout strips, thus enabling the reconstruction of the interaction point. While tracking is straightforward in case of single-hit events, in case of a higher occupancy

of the detector strips a more complex hit pattern analysis is required to distinguish between hits belonging to different primary interactions as distinguished from (Compton) scattered signals or even cross-talk between adjacent strips.

Analyzing the energy deposits can help to constrain the primary interaction position. In particular exploiting the energy correlation between the two signals, segmented in the n^+ and p^+ strips, respectively, can be used to resolve potential ambiguities. This includes the analysis (and whenever possible correction) of the charge sharing between neighboring strips. An overview of some commonly used semiconductor detector materials is shown in Table 2.1, where the ionization energy is the necessary energy to create an electron-hole pair.

Material	$\mathbf{Z}_{eff}$	ρ [g/cm^3]	ϵ [eV]
Silicon	14	2.33	3.6
Germanium	32	5.33	2.9
CdZnTe (CZT)	49	5.81	4.6
HgI_2	80	6.40	4.2

Table 2.1: Comparison between the properties of commonly used semiconductor detector materials, such as effective atomic number (Z_{eff}), density (ρ) and ionization energy (ϵ) [57].

From the practical point of view, the performance of semiconductor detectors, such as DSSSDs, is limited mainly by imperfect shielding, imperfect grounding that leads to pick-up of external high-frequency noise and ground loops or crosstalk between detector strips.

2.4.2 Scintillation Detectors: Absorbing Detector - $LaBr_3$

The principle of scintillation detectors is based on the conversion of individual energetic photons into a multitude of low-energy visible (or UV) photons: some organic or inorganic crystals doped with specific activator atoms ("color centers") that emit scintillation light (visible light or near-UV photons) when they absorb energetic radiation, are excited to a higher energy state and de-excite emitting a scintillation light. For inorganic scintillators, the capacity of emitting scintillation light is enabled by their crystal lattice structure, allowing only some electron bands (the valence and conduction bands), separated by a band gap, to be occupied (Figure 2.11).

These scintillation crystals with a high density for improved efficiency are used for γ ray detection, while plastic scintillation detectors are frequently used for β-particle measurements. Most scintillation detectors are solid and can be divided into two main categories: inorganic scintillators (such as NaI(Tl), CsI(Tl) —thallium-doped crystals or $LaBr_3$(Ce), where the color center is provided by the Cerium dopant) and organic scintillators (most liquid): anthracene or stilbene. These scintillation media are then coupled to a photodetector, typically a photomultiplier tube (PMT), which converts (and amplifies) the scintillation light into a measurable electric pulse [58].

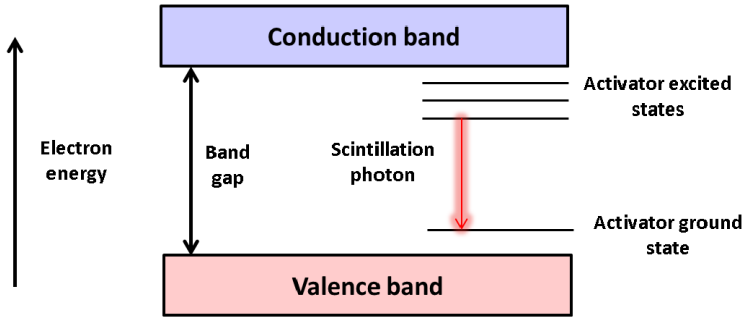

Figure 2.11: Sketch of the band structure for the electron energies in a scintillator material. The addition of activators to the crystal allows for the deexcitation of the electrons from the conduction band to the valence band with the emission of scintillation light [53].

Inorganic scintillators, such as Lanthanum (III) Bromide doped with Cerium ($LaBr_3$(Ce)), are characterized by good light yields, negligible self-absorption of the scintillation light and emission spectra that can be well matched to the sensitivity curve of photomultiplier tubes. However, some plastic scintillators show even better timing properties, with time resolutions well below 1 ns. A plastic scintillator is composed of a solid solution of organic scintillation molecules in a polymerized solvent. This type of scintillator is characterized by a relatively large light yield and a short decay time, which means that they are very fast, making these scintillators well-suited for fast-timing measurements or as trigger detectors [59]. Some scintillation detector materials are shown in Table 2.2.

Material	ρ [g/cm^3]	$\mathbf{Z}_{eff}$	τ [ns]	**Y** [ph/MeV]	**ΔE/E** [%]	**Hygroscopic** (yes/no)	**Org./Inor.**
NaI:Tl	3.67	51	230	38 000	5.6	yes	inorganic
$LaCl_3$:Ce^{3+}	3.79	60	28	46 000	3	yes	inorganic
$LaBr_3$:Ce^{3+}	5.29	47	26	63 000	3	yes	inorganic
$Bi_4Ge_3O_12$(BGO)	7.13	74	300	8200	12	no	inorganic
Lu_2SiO_5:Ce^{3+}(LSO)	7.40	66	47	25 000	10	no	inorganic
Gd_2SiO_5:Ce^{3+}(GSO)	6.71	59	60	9000	10	no	inorganic
Y_2SiO_5(YSO)	4.54	34	70	24 000	10	no	inorganic
BC-404, EJ 204, NE 104	1.03	-	1.8	$\sim$ 10000	-	-	organic
BC-408, EJ 200, Pilot F	1.03	-	2.1	$\sim$ 10000	-	-	organic
BC-418, EJ 228, Pilot U	1.03	-	1.4	$\sim$ 10000	-	-	organic

Table 2.2: Comparison of some scintillator materials and respective properties, where ρ represents the density, τ the decay time, Y the light yield in photons/MeV and ΔE/E the relative energy resolution at 662 keV [60, 48].

In view of properties listed in Table 2.2, $LaBr_3$ is an excellent scintillator for applications, where simultaneously good energy resolution and fast timing is required. $LaBr_3$ exhibits a high light output (63000 photons/MeV), good energy resolution (3—4% at 662 keV) and a very short decay constant of only 26 ns (more details will be given in section 3.1). These unique advantages come at the expense of a slightly lower density (compared, for example, to BGO) and as such results in a sightly lower detection efficiency [61]. These characteristics led to the choice of $LaBr_3$ as scintillator material used for the absorber component of the Compton camera (Figure 2.12 and Figure 2.17) [1].

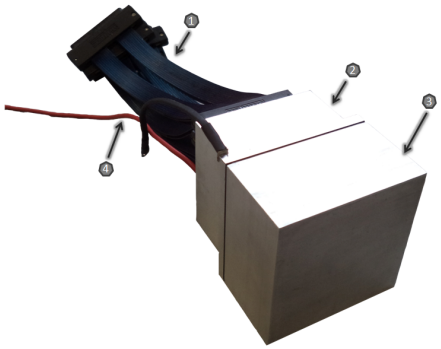

Figure 2.12: Photograph of the $LaBr_3$ detector, with the main components marked. (1) indicates the high-density cable to connect from the PMT to the readout board; (2) marks the PMT readout, caged by aluminum; (3) $LaBr_3$ detector, surrounded by an aluminum cage; (4) high-voltage cable.

$LaBr_3$ was specifically chosen due to its superb time resolution, which holds promise, together with the future fast trigger signal from the short-pulse laser generating proton beam to allow

for an efficient suppression of neutron background from proton-induced reactions. Time resolution is the central criterion for the quality of a time measurement, e.g., a time-of-flight measurement to distinguish between photons and neutrons. A detector that shows good timing resolution qualifies, e.g., as a fast trigger detector. The time resolution depends on the scintillator material itself, and on specific detector properties, such as the size and the surface conditions of the detector (if it is polished or not, or coated reflectively or absorptively). Other factors associated with the signal processing electronics can also cause variations of the time resolution [44].

When the gamma rays emitted from excited nuclei are collected in the absorbing scintillation detector of the Compton camera, data acquisition electronics will finally digitize the analog information and sort the resulting data into spectral histograms. Here, for example, the energy values of the registered photons will form the γ ray energy spectrum, where the characteristic transitions will show up as distinct peaks with a line width determined by the energy resolution of the detector. A high energy resolution allows for the separation of two gamma peaks that are close to each other, while in such a case, a low energy resolution returns a broad, unresolved spectral feature. Since the typical line shape of a γ transition is given by a Gaussian distribution, the energy resolution is usually reported as the corresponding Full Width at Half Maximum (FWHM).

Several factors influence the actually realized energy resolution, beyond the detector crystal properties, such as the number of photons registered in the detector, or an eventual non-linear scintillator response or sources of random noise. Assuming that the formation of each charge carrier is following a Poisson process, and assuming N to be the total number of charge carriers, according to the Poisson statistics of uncorrelated events, the standard deviation σ is $\sigma{=}\sqrt{N}$. However, this quantity only takes into account statistical fluctuations, and not further experimental factors.

Assuming a scenario, where a fixed experimental setup (electronics and detector readout system) is used, the contribution of the electronic noise should stay constant and can easily be subtracted. Considering the statistical noise to be the only source of fluctuations, one can write the Gaussian distribution in the following way:

$$G(E) = \frac{A}{\sigma\sqrt{2\pi}} \cdot \exp -\frac{(E - E_0)^2}{2\sigma^2} \tag{2.6}$$

where E_0 is the average pulse amplitude, E_0 = K N (K is a proportionality constant, and

A represents the area under the Gaussian. From the mathematical correlation between the FWHM and the standard deviation σ according to FWHM $= 2\sqrt{2\ln 2}\cdot\sigma$, a practical relation results as FWHM $\approx 2.35\sigma$, and also $\sigma = \mathrm{K}\sqrt{N}$ with K as a proportionality constant that describes the amount of energy needed to create a scintillation photon in the respective detector material [43]. The energy resolution R of the detector follows, according to the Poisson distribution, as:

$$R_{Poisson} = \frac{FWHM}{E_0} = \frac{2.35K\sqrt{N}}{KN} = \frac{2.35}{\sqrt{N}} \tag{2.7}$$

When the number of charge carriers is very high ($\sim$>55 000), which is the case for the semiconductor detectors such as silicon detectors, the total number of charge carriers cannot be described by simple Poisson statistics, because the semiconductor materials show a high mobility of charge carriers. The *Fano factor* (F) is a correction factor that corrects for the statistical fluctuations in the charge carriers that cannot be described using pure Poisson statistics. The Fano factor is defined as:

$$F \equiv \frac{\sigma^2_{observed}}{\sigma^2_{Poisson}} \tag{2.8}$$

where F ≈ 1 for most of the scintillation materials. However, for semiconductor materials the Fano factor is significantly lower than 1, for example the Fano factor for silicon is $\sim$0.115 and for germanium it is $\sim$0.13 [43]. Thus, the theoretical limit of the energy resolution is finally given by:

$$R \equiv \frac{\Delta E}{E} = \frac{2.35K\sqrt{N}\sqrt{F}}{KN} = 2.35\sqrt{\frac{F}{N}} \tag{2.9}$$

The energy resolution measurement of the $LaBr_3$ detector used in our Compton camera is described in detail in Section 3.4.

2.5 The Principle of a Compton Camera

Based on the kinematics of the Compton scattering process and subsequent photon absorption, one can reconstruct the source position of a primary photon on the surface of a

cone, known as "Compton cone" (Figure 2.13). The reconstruction of a 3D photon source distribution from Compton scattered data is usually performed by analyzing the measured observables (deposited energies and interaction positions) both from scatter and absorber components (detectors). If the position and energy deposition are detected in the scatter detector and subsequently in the absorber detector, then, via the Compton kinematics the direction of the primary photon can be localized in the surface of the so-called Compton cone [62], as the origin of the possible photon emission points[63]. From the superposition of several Compton cones from different events, their intersection is found and then, the position of the source can be localized.

Figure 2.14 displays the γ source position reconstruction for a conventional Compton camera (using a single scatter detector), where $N_\gamma = 1$, $N_\gamma = 2$ and $N_\gamma = 10$ represent the number of Compton events used for the reconstruction.

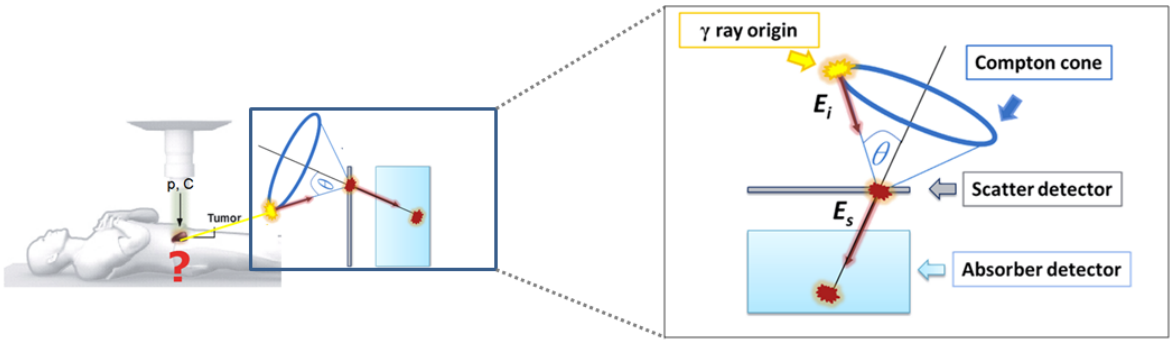

Figure 2.13: Sketch of a Compton camera using a single scatter detector allowing only for γ tracking, where θ is the scattering angle. The γ ray origin is shown in the Compton cone [53, 62].

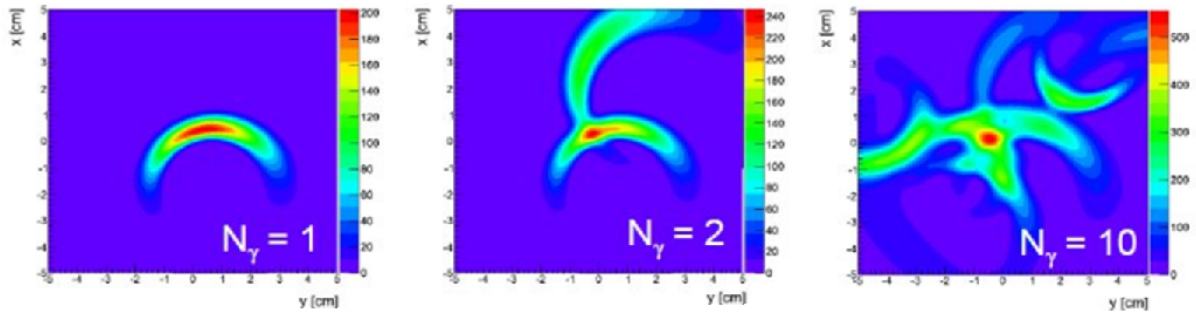

Figure 2.14: Simulated γ ray source position reconstruction for a Compton camera using a single scatter detector. N_γ represents the number of reconstructed Compton events [48].

As mentioned in Section 1.2.2, the typical Compton camera is composed of two components: the scatter detector and the absorber detector (some *double scattering* Compton cameras have two scatter detectors). The conventional Compton camera represented in Figure 2.13 allows for γ tracking, measures the energies and interaction positions in the respective detector modules. In this version, a single thick scatter detector is used, while the Compton (recoil) electrons will be absorbed in the scatterer and no kinematical information can be obtained.

However, if several layers of position-sensitive double-sided Silicon strip detectors (DSSSD) are used as tracker component, as shown in the Figure 2.13, one can additionally track the electrons, and this allows to restrict the Compton cone to an arc segment, thus improving the Compton camera reconstruction efficiency significantly, since it allows to use also incompletely absorbed photon events in the reconstruction process, which otherwise would have to be discarded. However, this requires the kinetic energy of the Compton electron to be large enough to penetrate at least one layer of the tracker array, which requires typically a minimum energy of the incident photon of about 1 MeV.

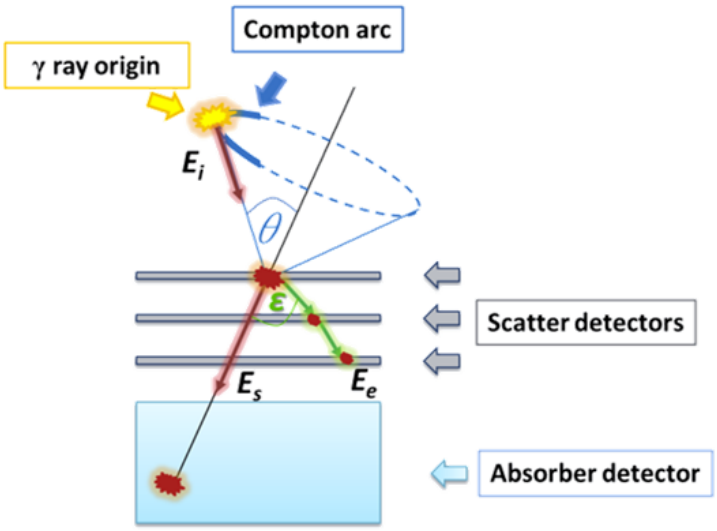

Figure 2.15: Sketch of the Compton camera principle using an array of several scatter detectors, designed for γ and electron tracking, where θ is the scattering angle.

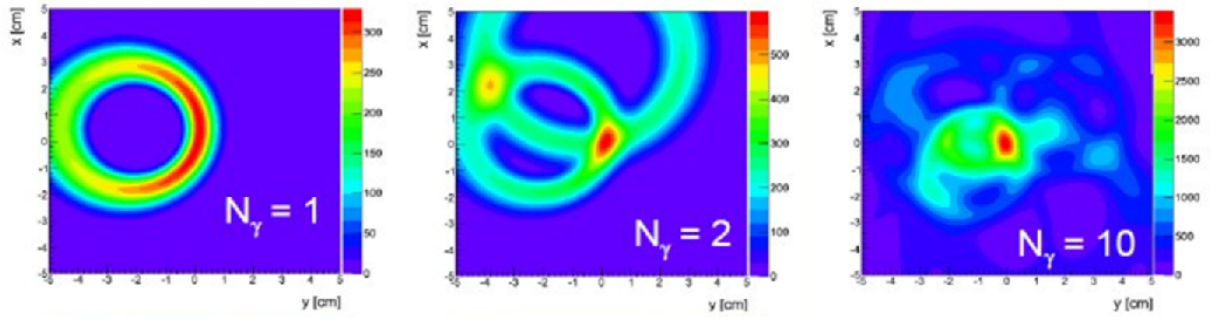

Figure 2.16: Simulated γ ray source position reconstruction for a Compton camera using an array of several scatter detectors. N_γ represents the number of reconstructed Compton events [48].

Figure 2.16 displays the γ source position reconstruction for a conventional Compton camera (using an array of several scatter detectors), where $N_\gamma = 1$, $N_\gamma = 2$ and $N_\gamma = 10$ represent the number of Compton events used for the reconstruction.

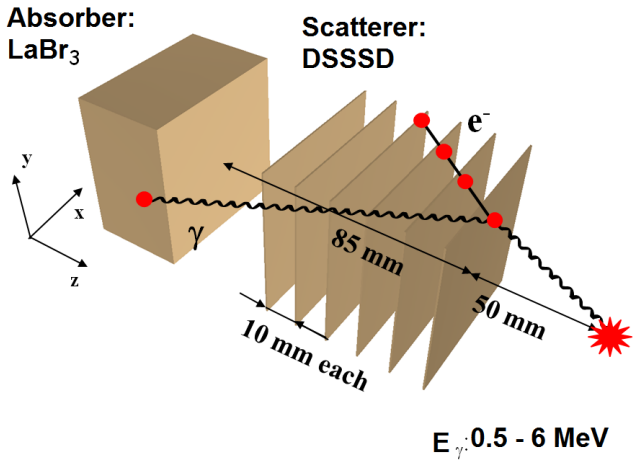

Figure 2.17: Sketch of the Compton camera prototype layout, studied here, designed for γ and electron tracking, to discriminate neutron background from prompt photon signals [48].

In the Compton camera project presented here, the reconstruction of events using the additional information from the position-sensitive scatter detectors is achieved by using the software MEGAlib, a GEANT4-based toolkit for simulations as well as event and image reconstruction (with maximum likelihood, expectation-maximization algorithm) [64].

2.6 Position determination: *k*-Nearest Neighbor Method

When it comes to the position-dependent detection of photons in medical imaging, as for example, via the PET technique, the conventional detection system relies on the use of a large multitude of individual, isolated, small scintillation crystals, typically with a front-face surface of only a few mm^2. This allows to derive the interaction position of an incident photon from the hit pattern on the detector block. Only recently, attempts were made to extract high-quality position information also from monolithic scintillation crystals [65]. Pioneering work in this field has been performed by the Delft group, where an algorithm has been developed, that allows to derive a position information of the photon interaction point from a precisely characterized monolithic scintillation crystal. The authors call this method the k-Nearest Neighbor Method (k-NN method), which will be briefly introduced in the following Section.

This method was developed by Fix and Hodges [66] and later studied by Maas et al. [67] for the determination of entry points of gamma photons in a monolithic crystal. This method is used for the position determination in monolithic crystals, which is a necessary prerequisite for the operation of a Compton camera based on a monolithic absorber crystal. It could already be demonstrated that this method offers an excellent spatial resolution for positron annihilation photons [65].

This method compares the light amplitude distribution for a certain isolated and unknown event with a reference dataset of light amplitude distributions I, in order to calculate the position of interaction. This reference dataset is unique for each crystal and has to be determined specifically by irradiating the crystal on a fine grid with a narrowly collimated photon source. For each irradiation position, a vector with the light amplitude distributions $\mathrm{I} = (\mathrm{I}_1, \mathrm{I}_2, \ldots, \mathrm{I}_N)$ is collected for a number of n_{ref} reference events (i.e., collected statistics in the photopeak of the respective calibration source). Considering N to be the number of readout segments of the photosensor used to generate the electronic signals from the crystal, the total number of n_{ref} reference points to be measured via an irradiation of $\mathrm{n}_{positions}$ on the scintillator surface can be calculated as:

$$n_{total} = n_{positions} \cdot n_{ref} \tag{2.10}$$

Generally, this reference dataset comprises a grid spanning the detector dimensions and

covering the whole surface of the detector with a pitch of 0.25-0.5 mm, where n_{ref} is about 100 (photopeak events) [53]. Hence, the unknown position of an interaction with coordinates *(x,y)* can be estimated according to the equation of the Euclidean distance:

$$D = \sqrt{\sum_{i=1}^{N} (I_{test,i} - I_{ref,i})^2} \tag{2.11}$$

where I_{test} is the measured light distribution for pixel i, I_{ref} is the member of the reference dataset for the pixel i, and N is the number of readout segments of the crystal. Afterwards, a subset containing the smallest values of D, the so-called nearest neighbors, is selected from the dataset of values D, and a histogram with these values and its coordinates (x,y) is produced. A typical histogram for the nearest-neighbor distribution can be seen in Figure 2.18, clearly indicating via its centroid the initial position of the incident primary photon.

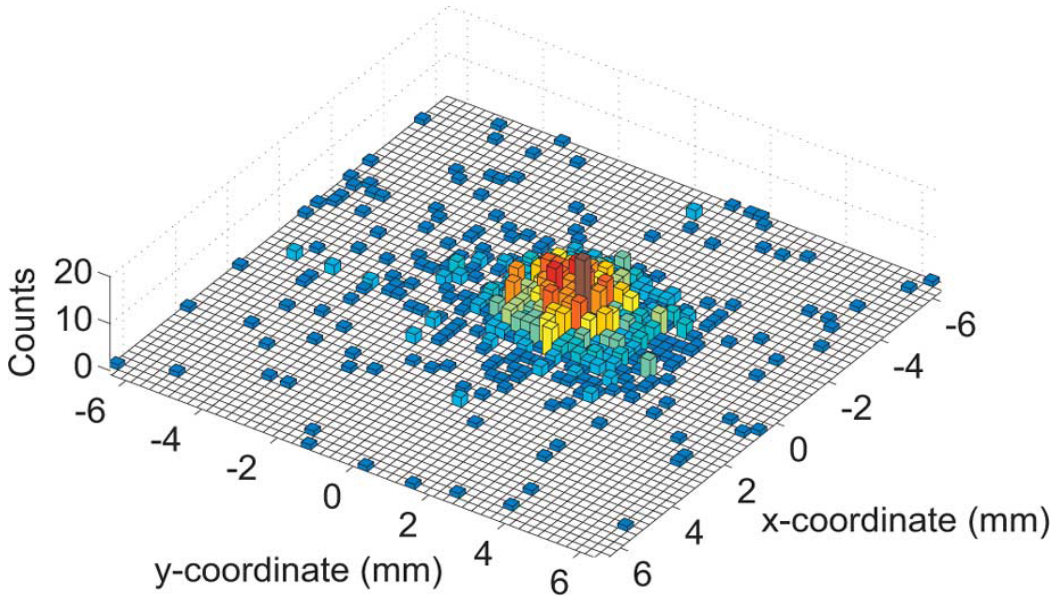

Figure 2.18: Example of a histrogram containing the γ source coordinates of the nearest neighbors taken from the reference dataset as selected by the k-NN method [65].

The improved k-NN method includes some new steps comparing to the standard method, such as smoothing and fitting. Typically, the histogram (similar to the one shown in Figure 2.18) is smoothed using a moving average filter, before attributing the coordinates of the histogram centroid as the primary photon interaction position for that event. Some other smoothing and fitting methods are discussed in more detail by H.T. van Dam et al. [65].

Finally, an error histogram is created, in order to enable a determination of the position accuracy.

Aiming for the creation of such a reference dataset, a collimator with a diameter of 0.5 mm was built by the Delft group to validate their method experimentally. In their measurements, a fine grid of 0.25 mm was used for scanning a (rather small) scintillation crystal of $13\times13\times10$ mm^3 size. In the Delft measurements, a position resolution of about 1.5 mm could be realized in the center of the crystal [65], motivating us to consider this technique as an option for our Compton camera prototype and its monolithic $LaBr_3$ crystal.

3

Experimental setup and offline characterization measurements

3.1 Specifications of the $LaBr_3$(Ce) detector

The $LaBr_3$ scintillation crystal is operated as absorbing detector of our Compton camera prototype. In this section, its specifications and the design of the detector will be presented.

For the presented detector setup, a $50.8 \times 50.8 \times 30$ mm^3 $LaBr_3$ monolithic crystal was used. BrilLanCe^{TM}380 $LaBr_3$:5%(Ce) (referred simply as $LaBr_3$ in this Master thesis) from Saint-Gobain [68] is a transparent scintillator material that shows a very fast response (26 ns primary decay time, due to the dopant ion Ce^{3+}), a high light yield of 63 000 photons/MeV, and also an excellent energy resolution (2.9% at 662 keV, reaching even 1.6% at 2615 keV) [69]. In fact, this detector qualifies as an ideal choice for gamma detection, in particular in a Compton camera, because of its short decay constant, which is significantly shorter than the one of commonly used LYSO:Ce detectors. Its good absorbing properties make it a promising choice for this experiment, because the high effective nuclear charge $Z_{eff} = 47$ provides a high density ($\rho = 5.06$ g/cm^3) and this allows for a high photoabsorption probability. A complication of the detector handling is given by the hygroscopic behavior of $LaBr_3$, which requires a tight encapsulation of the crystal, for example, an aluminum housing.

The very fast response, and therefore very good timing properties of this scintillator, allow for distinguishing the relevant prompt gamma photons from background signals, originating,

e.g., from neutrons created in proton induced nuclear reactions.

3.1.1 Intrinsic radioactivity of the $LaBr_3$ crystal

A property of the $LaBr_3$ crystal is its intrinsic radioactivity of about 2 Bq/cm^3 [48]. The natural intrinsic radioactivity of the crystal results in a constant count-rate of ∼140/s for our crystal with the dimensions mentioned above. This small, but not negligible, activity results from the presence of radioactive isotopes such as ^{138}La and ^{227}Ac and respective daughter products.

This intrinsic radioactivity is a characteristic of all ^{138}La halide scintillators, as shown by F. Quarati et al. [70]. A summed γ ray energy spectrum of the $LaBr_3$ intrinsic radioactivity is shown in Figure 3.1, measured for 1 hour.

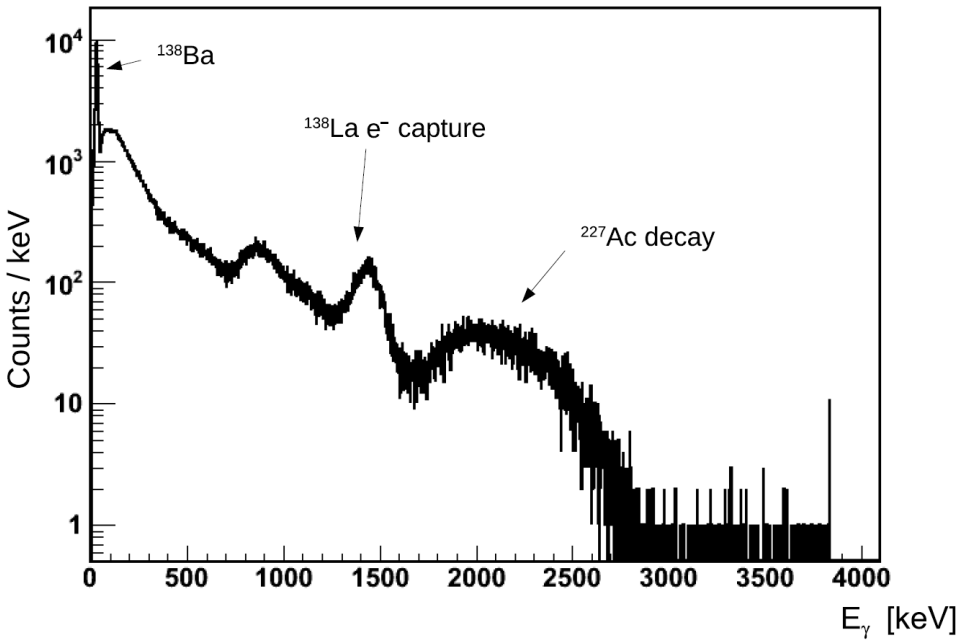

Figure 3.1: Energy spectrum from the intrinsic radioactivity of the $LaBr_3$ crystal, measured by C. Lang [48]. Three main reaction channels are observed, predominantly resulting from ^{138}La and ^{227}Ac decay.

The energy spectrum from the $LaBr_3$ crystal shows a strong line at ∼37 keV, which originates from the ^{138}Ba X-ray emission after the ^{138}La decay into ^{138}Ba by electron capture. The peak around 1450 keV results from a contribution of the ^{138}La decay by electron capture into ^{138}Ba,

emitting a γ ray. The broad contribution between ∼1500 keV and ∼3000 keV is due to the ^{227}Ac decay, producing α particles with a γ ray equivalent in the same range. This intrinsic radioactivity signal is added on top of the measured signals, however, it could also be used as a part of the energy calibration or online gain monitoring.

3.2 LaBr$_3$(Ce) characterization

Having described the design specifications of the $LaBr_3$ crystal, in the next section the characterization of the absorber detector will be described. Several measurements were performed and, in each of them, some challenges were faced. In the next pages, the signal processing electronics will be described, as well as the energy calibration measurements, time resolution and spatial resolution experiments.

3.2.1 Signal processing electronics

The $LaBr_3$ scintillator is read out by a multi-anode PMT (Hamamatsu H9500, 3×3 mm^2 pixel size, with 16×16 = 256 pixels), with a bias voltage set to -830 V. In a preliminary setup, a reduced segmentation of the readout was used by combining each 4 PMT segments into one readout channel, fed to the subsequent signal processing electronics. This way, effective 64 pixels with 6×6 mm^2 area were used, allowing for position measurements on an 8×8 pixel grid.

Each multi-anode PMT readout channel is individually connected via an adapter board (converting the 4×64 pin high-density ribbon cable connections to a 256× 10 ns single LEMO cable, shown in Appendix B) a 16 channel amplifier/ Constant Fraction Discriminator (MCFD-16) NIM module [71](from Mesytec). This requires a total of 16 (1 extra for the sum signal) MCFD-16 modules for the full setup with 256 readout channels and 4(1 extra for the sum signal) MCFD-16 for the reduced 64-channel setup. One additional MCFD-16 module is used for the sum dynode signal, which provides the summed energy signal of the full detector.

The MCFD-16 module features a built-in fast preamplifier, with adjustable gain of 1, 3 or 10. Gain 3 was used (except for the sum signal, which was operated with gain 1), and positive polarity was chosen. The gain was initially chosen on the basis of (first) a pulser calibration,

followed by a γ calibration source measurement. Placing a ^{60}Co calibration source (E_γ=1172 keV and 1332 keV emitted in coincidence) in front of the detector, one obtains an amplitude of 300 mV for the sum signal. Then, in order to realize the desired dynamic range of 8 MeV prompt γ ray measurements, corresponding to an amplitude of 1.9 V, the gain could not be chosen to be 3, as the setting is limited to a dynamic range from 0 to only $\pm$ 1.2 V. Thus a gain setting of 1 was chosen, despite the fact that in this case the dynamic range is from 0 to $\pm$ 3.5 V. Consequently, the full dynamics of the Charge-to-Digital-Converter (MQDC) (explained in the next pages) covers about 13 MeV of photon energy, which will be exploited, once measurements with higher-energy proton beams are performed (see the γ spectrum of Figure 2.5).

For the individual readout channels, also 8 MeV dynamic range was targeted: taking into account that E_γ=1.4 MeV corresponds to an amplitude of 80 mV, for the full range of envisaged γ ray energies to be measured, at least an amplitude of 400 mV is necessary. Hence, since the dynamic range of gain 3 reaches from 0 to $\pm$ 1.2 V, while the dynamic range of gain 10 only spans from 0 to $\pm$ 350 mV, gain 3 was chosen for the MCFD-16 modules in the case of the 256 individual readout channels.

Another favorable feature about the MCFD-16 modules is the fact that the output can be configured via jumper settings to be either unipolar or differential. Moreover, the module also contains a built-in gate generator, selectable polarity and all the parameters can be set through remote control. For the subsequent constant fraction discriminator settings, one can select and adjust:

- Output pulse width: from 6 ns to 660 ns (100 and 105 ns were chosen for the individual signals and sum signal, respectively);
- Dead time from 20 ns to 660 ns, we used 300 ns;
- Fraction (attenuation): 20% or 40%, in our case 20%;
- Delay from 4 ns to 20 ns, our specifications were 3 ns for the sum signal and 5 ns for the individual signals;
- Threshold (from 0 to 255), chosen to be 3 for the individual signals and 2 for the sum dynode signal;

All MCFD-16 modules were calibrated for low (50 mV) and high (150 mV) amplitudes. A rise time of 0.05 μs and a fall time of 0.05 μs was chosen for the signal shape adjusted

at the pulser module. Each measurement was taken for 10 seconds. A signal from the pulser generator was connected to each individual channel and the raw energy spectrum of the corresponding channel was checked. Thus the threshold for each channel was chosen manually, in order to suppress electronic noise signals (visible in the energy spectrum for the corresponding channel). Also, this pulser calibration allows for determining if any of the 256 channels is not working as expected. Then, with the pulser calibration measurement, the MCFD-16 thresholds were adjusted in order to discriminate the electronic noise without cutting into the signal. If we verified that the level of electronic noise was too high in the spectrum, we would increase the threshold in the MCFD-16 module.

For our experiments, first with the 64-channel setup and then with the 256-channel setup, we used the same parameters, except for the threshold. We started out by using threshold values between 2 and 4 with the reduced setup, where these values were all checked individually using the pulser calibration described above. For the 256-channel setup, the threshold value was set to 3 for all the individual signals and 2 for the sum dynode signal. The output pulse width chosen for the individual signals was 105 ns and 100 ns for the sum signal. The dead time of the MCFD-16 is the conversion time or the "recovery time", and this value needs to be set between 250 ns to 300 ns for all channels, including the sum signal channel, since the conversion time of the MQDC is 250 ns. Thus, this value was set at 300 ns to have a safety margin. The rise time of the 256 channels was found to be 6.4 ns, and the MCFD-16 delay of these 256 channels should be ∼70% of the rise time, resulting in ∼5 ns. The rise

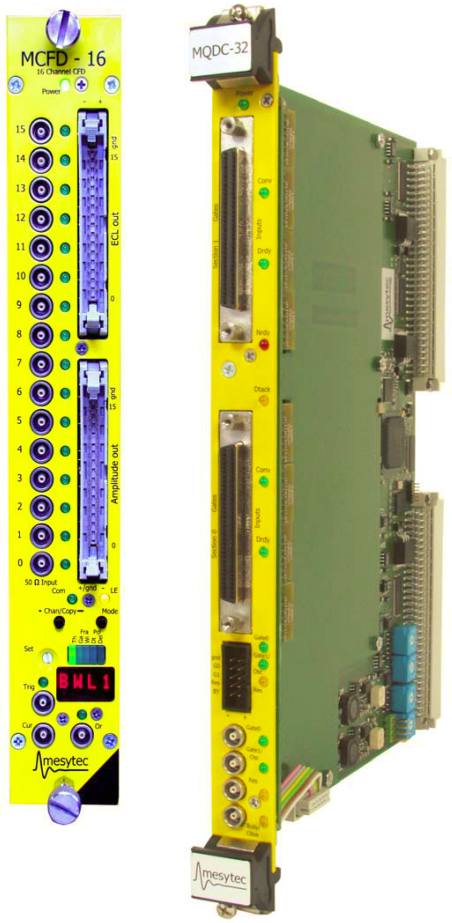

Figure 3.2: Front view of the amplifier/Constant Fraction Discriminator module MCFD-16 (left) and VME-based Charge Digitizer module MQDC-32 (right) signal processing modules. [71, 72].

time of the sum signal is about 4 ns, so a delay of 3 ns was chosen. The fraction was set to a value of 20%.

Thus having configured the MCFD-16 modules, they are ready to receive the 16 LEMO cable inputs with the individual signals from the PMT segments (as can be seen on the left side of Figure 3.2). The modules provide two types of output: first the amplified energy signal (in the left part of Figure 3.2, visible as "Amplitude out") and 16 individual gates (labeled "ECL out" in Figure 3.2). These 16 amplified energy signals and the 16 individual gates are provided by a multi-pin flat ribbon cable connector. The corresponding signals are fed to the subsequent modules via 34-pin ribbon cables (3M^{TM}Twisted Pair Flat Cable, 3782 Series, 4.99 ns/m propagation delay) [73].

The energy signals are then directly fed to charge integrating ADC modules, commonly known as MQDC (Charge-to-digital converters). In our case, we use the MQDC-32 modules from Mesytec [72]. Each MQDC is able to process 32 individual channels, accepting 2×32 input signals, provided through 34-pin ribbon cables. Each of these 32 input signals entering one high-density connector contain 16 energy signals and 16 gate signals generated by one MCFD-16 module. They are combined via an adapter (which is shown in Figure 3.3). Thus, each MQDC is able to read the information from two MCFD-16 modules.

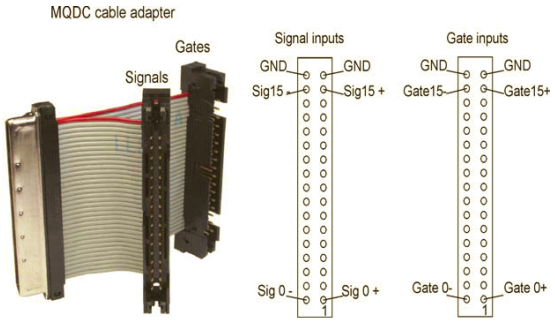

Figure 3.3: MQDC-32 adapter cable from Mesytec [72], combining two 16-channel, output signals (16× energy, 16 × individual gates) from the preceding amplifier/CFD module MCFD-16 into one 32-channel input for the charge digitizer MQDC-32.

The sum dynode energy signal is digitized in a separate MQDC module. The logical OR signal from the MCFD-16 module is used as trigger signal for the data acquisition process. This signal is delayed by 500 ns, which is required by the shaping time of the amplifiers used to operate the DSSSDs of the Compton camera. The MQDC modules are read out by a VME-based data acquisition system [74], controlled by a trigger unit (TRIVA 5 from GSI),

combined with a RIO-3 Power-PC (PPC) from CES [75].

In summary, each MCFD-16 module amplifies the signal from 16 PMT segments and creates an individual gate for each of these signals. Afterwards, the amplified energy signal and the respective individual gate are fed to a MQDC through a ribbon cable with 13 m and 8 m length, respectively. In the case of the sum signal, the MCFD-16 creates the master gate and the OR output of the MCFD-16 module is connected to a Logic Unit (Quad Coincidence Logic Unit, C.A.E.N, Module N455) that splits the signal to be connected to all the MQDC modules to provide a master gate. The master gate allows to assure that all the channels are read out simultaneously, event per event. A sketch of the signal processing electronics is represented in Figure 3.4.

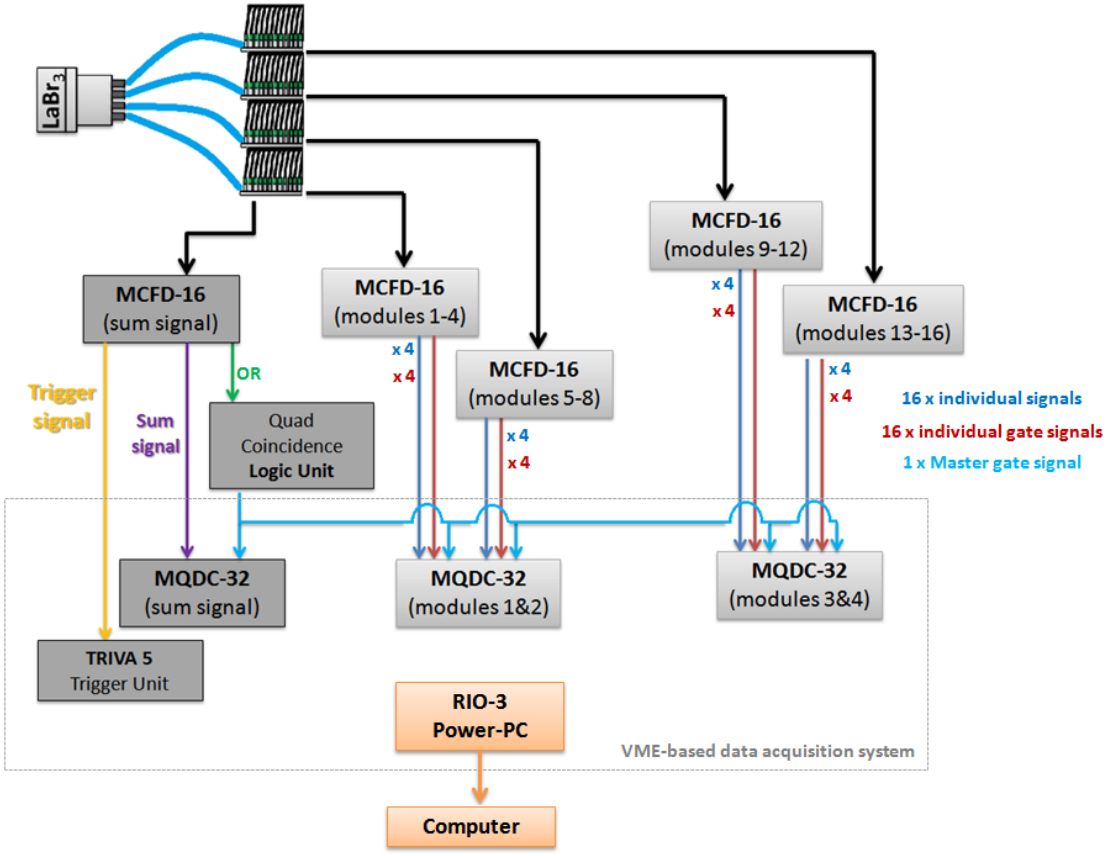

Figure 3.4: Block diagram of the signal processing electronics.

However, the MQDC module requires a certain time interval between the signal, the individual gate and the master gate, thus one has to be sure that the master gate is covering the individual gate signal (and obviously the signal), fulfilling the timing requirements shown in

Figure 3.5.

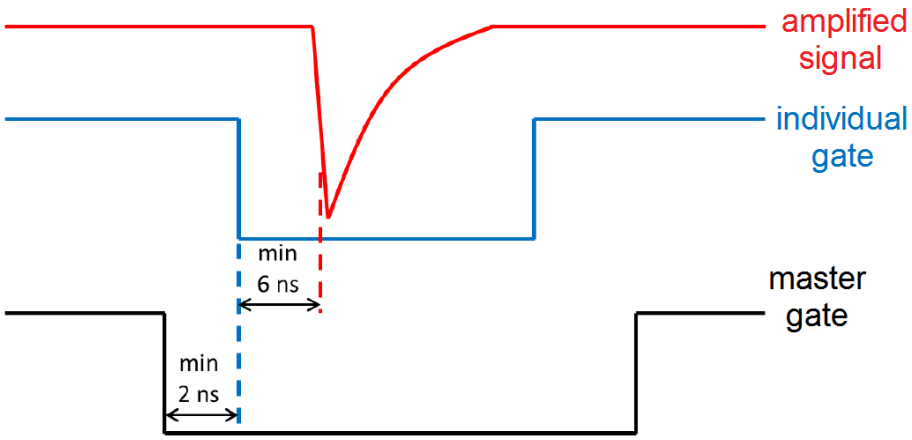

Figure 3.5: Sketch of the timing requirements of the MQDC. Adapted from [53].

The cable length required for the two delay path for the signal and gate can be calculated the following way [72]: L0 is the LEMO cable length that connects the MCFD-16 OR-output to the MQDC (1 m), L1 is the length of the ribbon cable that connects the individual gate signal output to the MQDC (L1 = L0 + 2m) and L2 is the length of the ribbon cable that connects the amplified energy signals to MQDC signal inputs (L2 = L1 + 2m+ delay[ns] × (1 + fraction)/5 [m/ns]). Therefore, a length of 3 and 7 meters for the individual gates and amplified signals should be sufficient. In fact, for the reduced setup with 64 channels, these cable lengths were used. However, we used the inhibit method using a Logic Fan-in/Fan-out module (C.A.E.N. Module N454), that provides copies from the gate of the sum dynode to send them to all the MQDC modules as a master gate. Obviously, the use of additional modules and LEMO cables to transport the signals also introduces some additional delay. Thus the trigger and the master gate signals were compared on the oscilloscope and the resulting optimum values for the delay cable lengths were calculated. Instead of the previously used 3 m, at least 7 m length cable were needed, so we chose 8 m to have a safety margin, and instead of 7 m at least 12 m were necessary, so we chose 13 m for the same reason. Therefore, using 13 m (respectively 8 m) ribbon cable for the amplified energy signal, the necessary time delay between the master gate and the individual gate (respectively the individual gate and the signal) is guaranteed, and no signals are truncated or lost.

Two delay boxes were designed to house the ∼5 km of ribbon cables. These two shielded rack-mounted delay boxes have 2×16 ribbon cable connections and enough space inside to

place the cable rolls. The signal from the MCFD-16 module is connected to the input of the delay box (via a 50 cm ribbon cable), inside which there are 12 m (respectively 7 m) of ribbon cable, and then the output connection requires another 50 cm of ribbon cable that is connected to the MQDC. A delay box and respective connections are shown in Figure 3.6.

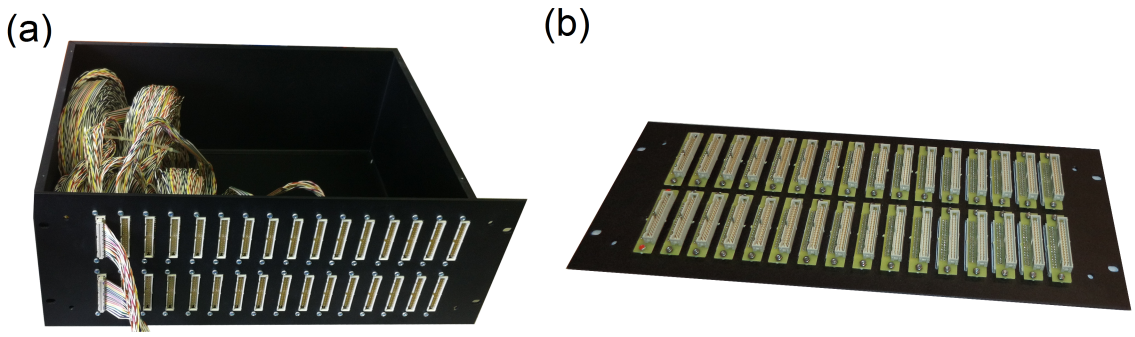

Figure 3.6: Photographs of the delay box containing the ribbon cables providing the time delays for signals (13 m) and gates (8 m); (a) seen from the outside with cable rolls inside, (b) inner connections, that connect to the rolls with 12 m length (respectively 7 m), where each 4 connection lines are associated to one (differential) MQDC channel input (2 for the energy signal and 2 for the gate signal).

3.3 Data analysis tools

Several computer-based tools were used for the data analysis, manipulation steps of the raw data and graphical visualization. These tools allow the user to manipulate the raw data collected from the data acquisition electronics in the most convenient way. Obviously, the raw data cannot be directly used to evaluate the results from the experiments, since they do not take into account several correction steps, for example, efficiency, dead time, solid angle, as well as the parameters to be implemented for the energy and time calibration procedures.

Data acquisition was performed via VME-based readout CPU (RIO 3 from CES) [75, 76], controlled by the MARABOU data acquisition monitoring, storage and visualization system. In summary, " MBS and Root Based Online/Offline Utility (MARaBOU) is a system for data acquisition and evaluation (...) that consists of a front-end system for data readout, event building, and data transport based on the Multi-Branch System (MBS)[75], and a back-end system responsible for setup, run control, histogramming, data analysis, and storage written within the ROOT framework" [74]. The acquisition process running on the DAQ PC is *M_ Analyze*. This process receives the input data from the front-end VME modules

via MBS, converts the MBS events to ROOT objects, allows for online monitoring and histogramming, and then stores the acquired data in ROOT format for posterior offline data analysis.

In order to facilitate the ROOT-based data monitoring and offline analysis, in the course of the present work, a presentation and manipulation tool called *HistPresent* was used [74], that provides the user with a subset of practically required ROOT functionalities. *HistPresent* is a histogram presenter program, and it "provides tools typically needed in an online monitoring environment of nuclear physics experiments". This program works also with ROOT objects, stored in memory-mapped areas or normal ROOT files. It is able to perform several tasks, such as histogramming in 1,2 or 3 dimensions, arithmetic operations (such as adding, multiplying, dividing), and some specific tasks such as scaling, re-binning, fitting and others.

As mentioned, for both online and offline analysis, several codes were modified and implemented in order to analyze the data from the experiments. The data manipulation procedures based on the implemented codes will be briefly described here. *HistPresent* allows to visualize and manipulate the raw data collected during the measurements, where a user-defined C++ code defines calibration procedures, analysis conditions and (multi-dimensional) histograms. These histograms are provided by *HistPresent* to the user for further processing.

3.4 Energy calibration and energy resolution

The energy calibration of the $LaBr_3$ absorber detector was performed using ^{60}Co and ^{152}Eu radioactive calibration sources. The distance between the detector surface and the source was approximately 13.5 cm.

Energy spectra were obtained for each of the calibration sources, and are represented in Figure 3.7.

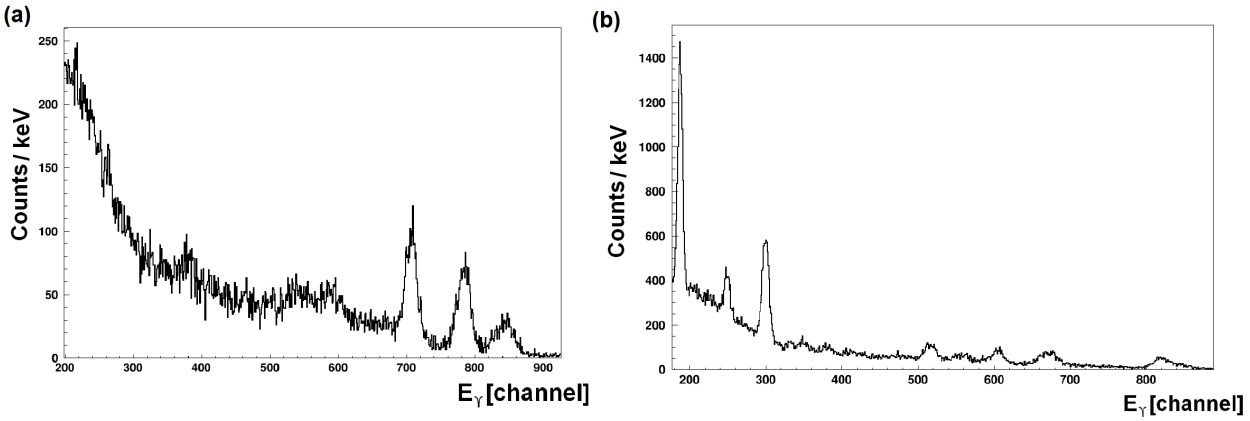

Figure 3.7: Uncalibrated γ ray spectra from ^{60}Co (a) and ^{152}Eu (b) sources. The peaks from these spectra were fitted and used as basis for the determination of the energy calibration parameters for the Tandem accelerator experiments in June 2014.

The centroid of each peak chosen for the calibration was determined by a Gaussian fit and subsequently the energy calibration, i.e., the correlation between a measured MQDC channel value and its corresponding γ ray energy, was performed by applying a linear fit function to generate the calibration curve. The ROOT toolkit [74] was used for the fitting procedure, applying a fit function according to:

$$E_\gamma[keV] = p_0 + p_1 \cdot E_\gamma[ch.] \tag{3.1}$$

where E_γ [keV] represents the calibrated energy of the photon in keV, while E_γ [ch.] represents the uncalibrated channel number in the MQDC where the photon was detected. The result for the ^{60}Co source is displayed in Figure 3.8, where the peak fits (indicated in the figure) prove the quality of the energy calibration with a deviation of merely 0.2-0.5%.

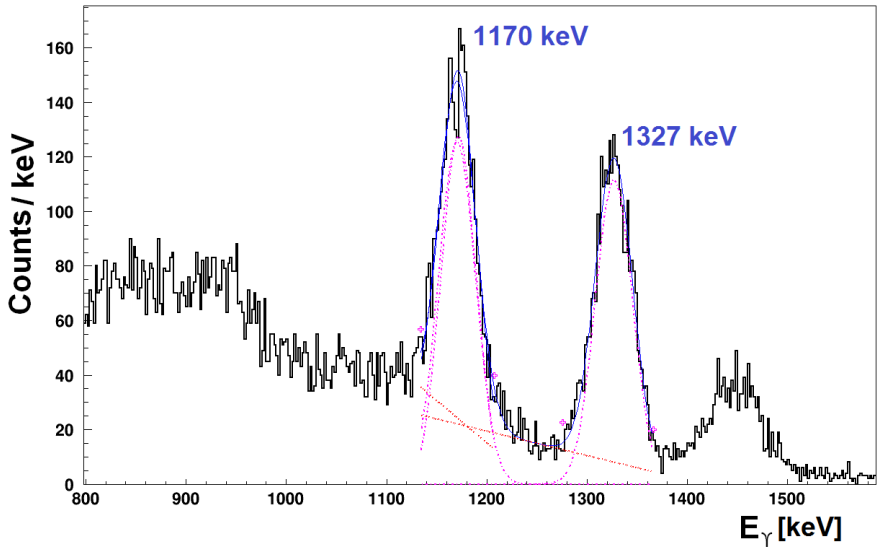

Figure 3.8: Calibrated spectrum for the ^{60}Co calibration source, where the peak fits are indicated. The centroids are 1170 (±0.5) and 1327 (±0.5), respectively. This corresponds to a deviation from the nominal values of 1173 keV and 1333 keV of less than 0.5%.

The energy calibration was repeated each time before an online experiment at the Tandem accelerator, because in particular temperature changes can lead to changes of the calibration constants over time.

In Table 3.1 the peak positions determined for the γ transition from ^{152}Eu and ^{60}Co used for the $LaBr_3$ energy calibration performed in April 2014 are shown. These values were then used to plot the calibration curve displayed in Figure 3.9, and to derive the corresponding calibration constants:

E_γ [keV]	121.78	244.70	344.28	778.9	1173.2	1332.5
E_γ [Channel]	169.3	229.8	277.2	480.0	658.7	730.0

Table 3.1: Peak positions of ^{152}Eu and ^{60}Co γ-transitions determined during the $LaBr_3$ energy calibration performed prior to the Tandem accelerator experiment in April 2014.

The obtained result for the $LaBr_3$ energy calibration in April 2014 is displayed in Figure 3.9:

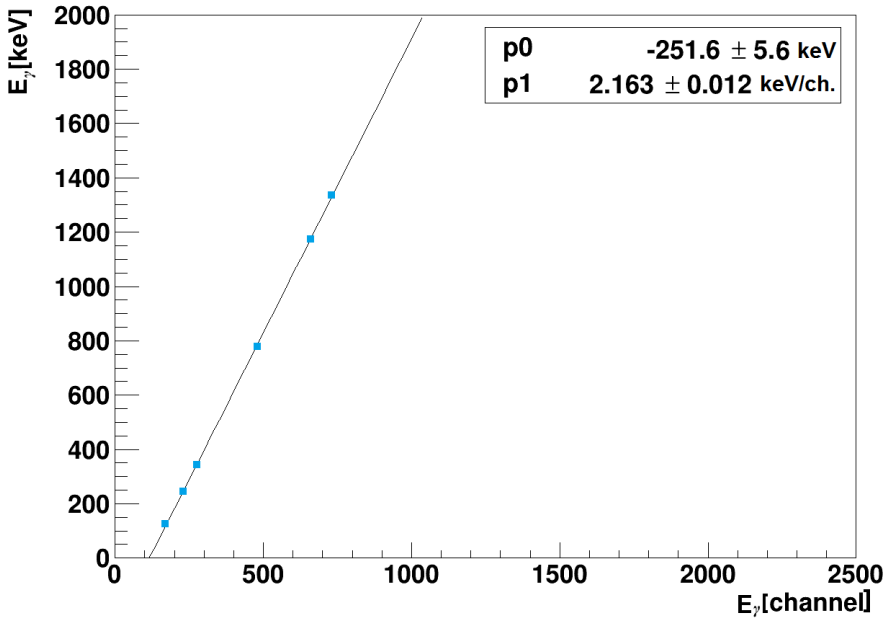

Figure 3.9: Energy calibration curve for the $LaBr_3$ absorber detector derived in April 2014 with a ^{152}Eu and a ^{60}Co calibration source. The calibration parameters of the linear fit curve (solid line) are shown in the plot.

From the linear fit to the calibration points shown in Figure 3.9 by the solid line, the following energy calibration parametrization could be determined:

$$E_\gamma[keV] = -251.6\text{keV} + 2.163\text{keV/ch.} \cdot E_\gamma[\text{ch.}] \tag{3.2}$$

In order to demonstrate the need of a specific energy calibration repeated for each measurement campaign, the comparable calibration procedure is also presented for the beamtime performed at the Garching Tandem accelerator in June 2014.

Here, Table 3.2 lists the peak positions of the calibration points from ^{152}Eu and ^{60}Co similarly to Table 3.1. In a similar way as described before the calibration curve (shown in Figure 3.10) was plotted and the corresponding calibration parameters were determined (included in the plot and in Equation 3.3.

E_γ [keV]	121.78	244.70	344.28	778.9	1173.2	1332.5
E_γ [Channel]	143.7	207.8	259.1	480.2	675.9	735.6

Table 3.2: Calibration values determined in the experiment in June 2014.

The obtained result for the linear energy calibration is shown in Figure 3.10:

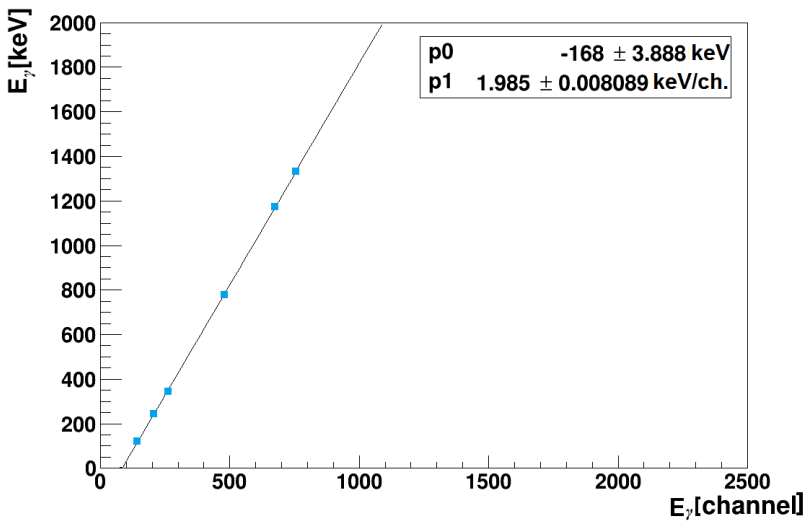

Figure 3.10: Energy calibration curve for the absorber detector determined in June 2014 with a ^{152}Eu source and a ^{60}Co source. The calibration parameters are shown in the plot.

Then, the equation of the calibration curve is:

$$E_\gamma[keV] = -168\text{keV} + 1.985\text{keV/ch.} \cdot E_\gamma[ch.] \tag{3.3}$$

As can be seen from the calibration curves shown so far, the assumption of a linear energy calibration characteristics seems to be well justified. However, one has to concede that it was only derived from the calibration points below $\sim$ 1.3 MeV, while the interesting part of the prompt γ energy spectrum lies between 4 and 6 MeV, respectively. Therefore, it was not surprising to encounter during the proton-induced online measurements significant deviations in the calibrated γ ray energy spectrum for the strongest peaks, expected to originate from deexcitations in ^{12}C, ^{14}N and ^{16}O (see Figure 2.5). Without a proper high-energy calibration (which in the meanwhile was performed in August 2014 at the Tandetron facility of the HZDR in Rossendorf with 4.44 MeV photons), the only solution was to refer to the simulated energy spectrum from Figure 2.5 as a guideline to the interpretation of the actually measured prompt γ spectrum, using the identical electronics settings as for the offline source calibration with ^{152}Eu and ^{60}Co. Table 3.3 lists the resulting calibration points, reaching up to 6130 keV, originating from the first excited state of ^{16}O. Moreover, in order to include also potential nonlinearities of the calibration curve, the data points from Table 3.3 were fitted by a second order polynomial according to:

$$E_\gamma[keV] = p_0 + p_1 \cdot E_\gamma[ch.] + p_2 \cdot (E_\gamma[ch.])^2 \tag{3.4}$$

Table 3.3 lists the calibration points used for the quadratic energy calibration of the $LaBr_3$ detector, including 3 data points from photopeak, single-escape and double-escape of the 6.13 MeV ground-state transition in ^{16}O.

E_γ [keV]	121.78	244.70	344.28	511	778.9	1173.2	1332.5	5109	5619	6130
E_γ [Channel]	187.5	249.5	300	382.8	515.8	706.8	783.5	2438	2643	2839

Table 3.3: Peak positions of ^{152}Eu, ^{60}Co and $^{16}O^*$ deexcitation, determined during the beamtime in June 2014. The 3 data points above 5 MeV were taken from the prompt γ spectrum measurement during the experiment (see Figure 4.15), with the peak assignments verified by GEANT4 simulations.

Figure 3.11 displays the calibration curve derived from the calibration data specified in Table 3.3, while Equation 3.5 specifies the corresponding quadratic parametrization.

$$E_\gamma[keV] = -239\text{keV} + 1.913\text{keV/ch.} \cdot E_\gamma[\text{ch.}] + 0.0001156(\text{keV/ch.})^2 \cdot (E_\gamma[\text{ch.}])^2 \tag{3.5}$$

It is obvious that the quadratic term contributes significantly to the accuracy of the energy calibration. This calibration was finally used for the measurements during the beam experiment in June 2014. The calibration curve given by this equation is shown in Figure 3.11:

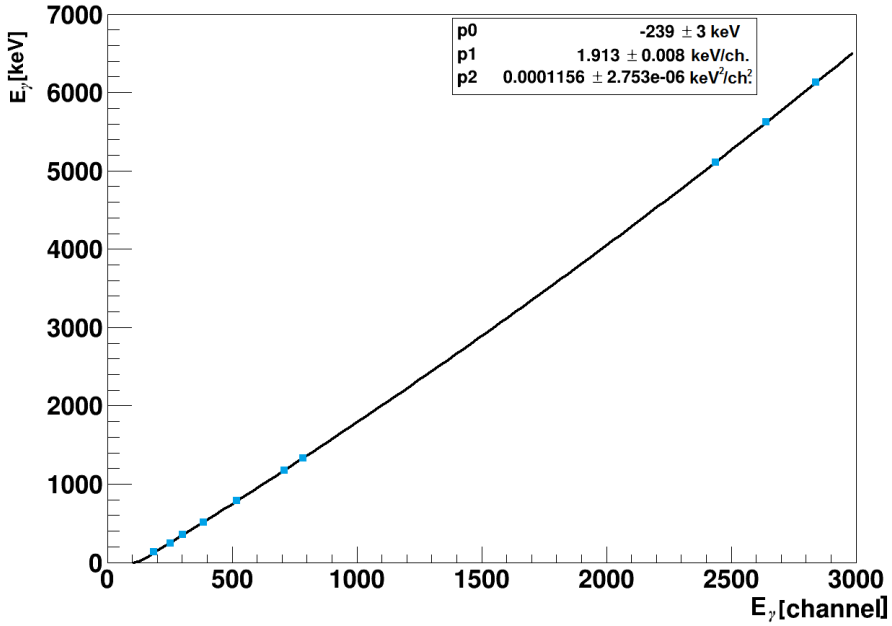

Figure 3.11: Energy calibration curve for the $LaBr_3$ absorber detector as obtained for the beam experiment in June 2014 with ^{152}Eu and ^{60}Co sources and including high-energy data points from the measured prompt γ energy spectrum (see Figure 4.15). The calibration parameters (from a quadratic fit function) are included in the plot.

Energy resolution

The energy-dependent energy resolution was calculated from the energy calibration data by analyzing the peak widths obtained from the Gaussian fits to the calibration peaks. Moreover, the new cable-delays (in total 8 m twisted-pair ribbon cable connected to each readout channel between the MCFD-16 and MQDC-32 modules, already introduced in section 3.2.1), were tested in view of their influence on the energy resolution.

Comparative measurements were performed, first with the initial cable delay, where a roll of 8 m ribbon cable was openly and directly connecting the MCFD-16 and the MQDC-32 modules, and second with the new, shielded rack-mounted delay boxes, which left only 2×50 cm open ribbon cable connections to and from the delay box. Better energy resolution was found for the modified cable delays inside the shielded rack-mounted boxes. For the modified cables, 3.4(8)% and 3.46(57)% energy resolution (ΔE/E) was found, respectively, for the 1173.2 and 1332.5 keV calibration lines from ^{60}Co.

Before, with the openly running signal cables, these values amounted to 4.7(10)% for 1173.2

keV and 4.2(11)% for 1332.5 keV. Thus a significant improvement around 25% for the relative energy resolution could be achieved by realizing a proper shielding of the long cables, carrying the analog signals to the digitizer modules.

During the beam measurement in June 2014, these delay boxes together with the modified cables arrangement were used for the first time. From this final setup, the energy resolution was calculated as a function of the γ ray energy, using the peak widths σ of the Gaussian fits to the calibration lines from ^{152}Eu and ^{60}Co sources. The results are listed in Table 3.4. The last column gives the relative energy resolution ΔE/E.

E_γ [Channel]	ΔE [Channel]	E_γ [keV]	ΔE/E [%]
187.5	7.283	121.78	3.9
249.5	8.453	244.70	3.4
300	10.211	344.28	4.1
382.8	13.078	511	3.4
515.8	18.689	778.9	3.6
706.8	20.123	1173.2	2.9
783.5	23.213	1332.5	3.0

Table 3.4: Relative energy resolution (ΔE/E) as a function of the γ ray energy of the calibration transitions in ^{152}Eu and ^{60}Co.

As can be seen from Table 3.4, ΔE/E drops from about 4% at the lowest energies to about 3% at 1.3 MeV. Since the resolution is expected to have an hyperbolic behavior, its value drops for higher energies.

3.5 Spatial resolution

Besides the energy resolution, the achievable position resolution of the primary photon interaction in the $LaBr_3$ absorber is a prerequisite of its operation in the Compton camera. Therefore, several measurements were performed in order to characterize the spatial properties of the $LaBr_3$ detector. The first measurements were performed still using the reduced setup with only 64 readout channels. The objective of these measurements was to investigate the correlation between the irradiation position and the acquired light distributions for the crystal, in order to obtain a grid of reference light amplitude distribution for each position.

It is important to notice that, in this detector, the adjacent readout segments are not light-isolated. This means that, if one PMT segment collects scintillation light, simultaneously practically all the other segments will also detect photons, due to the propagation of the scintillation photons within the crystal.

The method of choice to characterize the position-dependent response of the $LaBr_3$ crystal with the multi-anode readout to incident γ radiation is to scan (in x and y directions) the detector with a collimated photon source. In our case, we used a calibration ^{137}Cs source (E_γ=662 keV, with about 85.3 MBq) available at the Physics Department E12 of the Technische Universität München (TUM), shown in Figure 3.12. All the spatial resolution measurements were performed in the Gamma-Labor of the Physics Department E12 of the TUM.

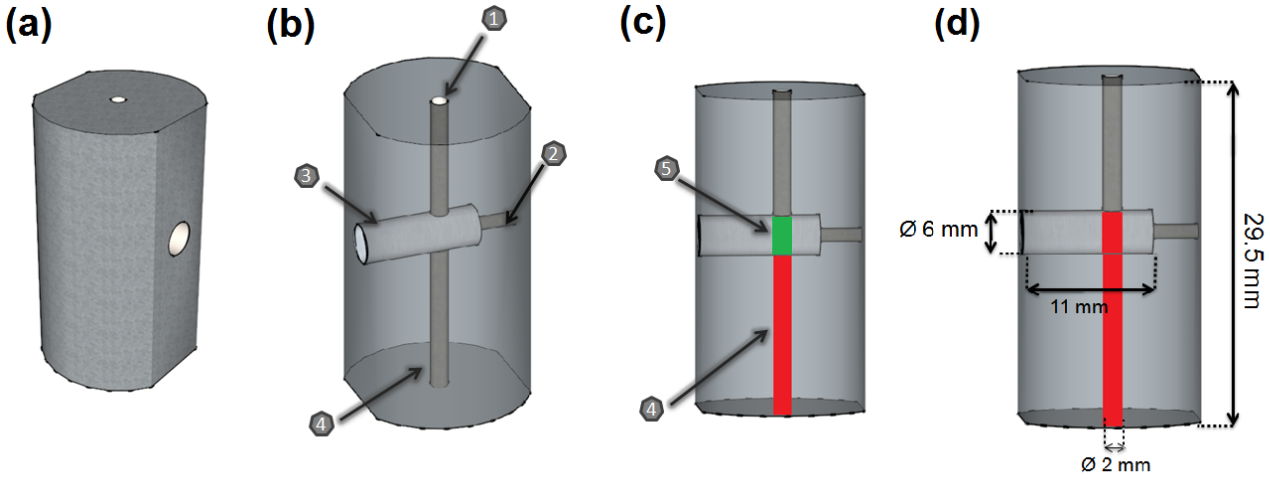

Figure 3.12: (a) Solid cylinder made of tantalum. (b) translucent view of the calibration source, where "1" represents the opening for the screw that fixes or allows to move the source cylinder, "2" is the channel that allows to push and pull the source cylinder and move the active source area ("5") to the left or right, "3" represents a channel housing a stainless steel cylinder with the ^{137}Cs source, and "4" represents the channel through which the beam goes from the source to the collimator. (c) "5" (green rectangle) is the active area of the source, which provides the collimated photon beam leaving the collimator assembly through the channel highlighted in red ("4"). (d) Source container dimensions, where the depth of the stainless steel cylinder is shown (11 mm), as well as its diameter (6 mm) and the height of the tantalum cylinder (29.5 mm).

In order to realize an optimum characterization, which is required to obtain the reference dataset for the k-NN method discussed in Section 2.6, a well-collimated photon beam is needed. Therefore we started out from using the existing collimator setup in the TUM

laboratory, consisting of a 48 mm collimator block made of DENSIMET® (a tungsten alloy, whose composition is 95% tungsten + 3.5% nickel + 1.5% iron) with an open diameter of 1 mm, complemented by an arrangement of lead bricks to shield the ^{137}Cs source from emitting anywhere else but into the 1 mm collimator channel, shown in Figure 3.16). With an attenuation coefficient of DENSIMET® of μ_{DENSI} ~1.86 cm^{-1}, this high-Z alloy is an excellent shielding material, while for lead the value is μ_{Pb} ~1.41 cm^{-1}.

The principal setup is shown in Figures 3.13, 3.14 and 3.15, where the radioactive source is mounted behind the opening of the collimator block, while on the other side the $LaBr_3$ crystal with its PMT is visible.

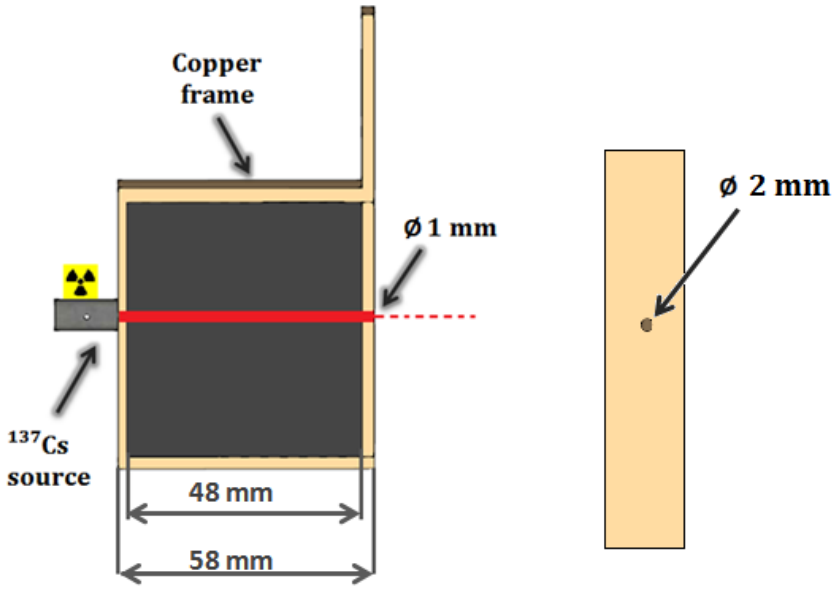

Figure 3.13: Design specifications of the 1 mm (diameter) collimator assembly, with the ^{137}Cs source on the back side, and a front view of the collimator frame (with a 2 mm hole in the surrounding copper frame), behind which the collimator block with its 1 mm channel is positioned.

The source on the back side of the collimator block is mounted to the copper frame using screws (the drawings of the frame can be found in Appendix A), in order to be aligned to the frame hole on the back side, which is also aligned to the collimator channel. Both holes in the frame (front and back side) have a diameter of 2 mm. The source collimation channel also has a diameter of 2 mm. The frame holds the collimator, but which, however, is not fixed to the frame. So the collimator block slides sideways, what could introduce some lateral

alignment uncertainty, which is planned to be removed in a re-design of the assembly.

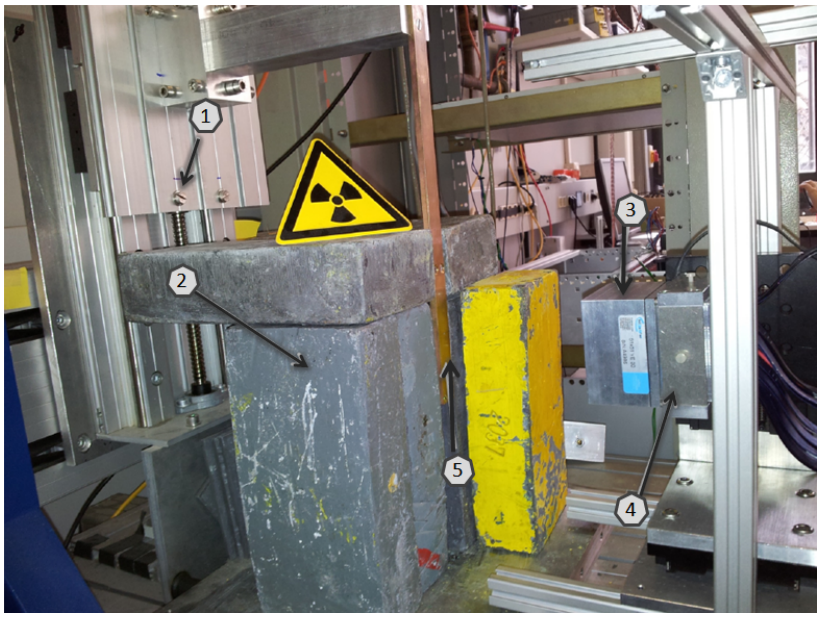

Figure 3.14: Photograph of the laboratory setup used for determining the spatial resolution of the $LaBr_3$ scintillation detector using the ^{137}Cs source. (1) represents the vertical positioning mechanism, (2) some lead bricks surrounding the detector (later more lead bricks were added), (3) the $LaBr_3$ crystal inside the aluminum housing, (4) shows the PMT inside the detector holder, (5) is the copper frame, surrounding and supporting the DENSIMET® collimator block.

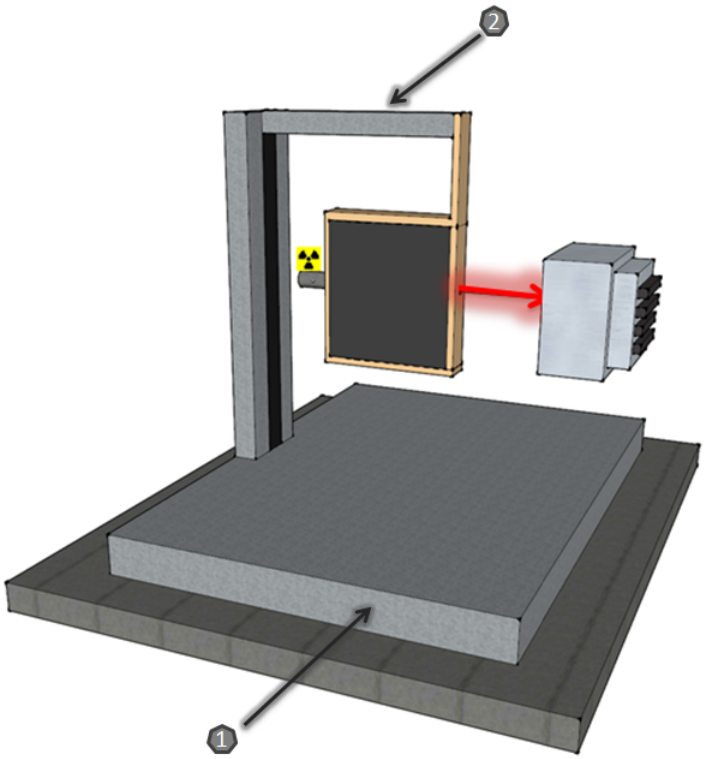

Figure 3.15: Setup of the collimated ^{137}Cs source without any surrounding lead bricks, with the radioactive source on the back side of the 1 mm collimator block. Components (1) and (2) can move in x and y direction, respectively, via computer-controlled stepping motors.

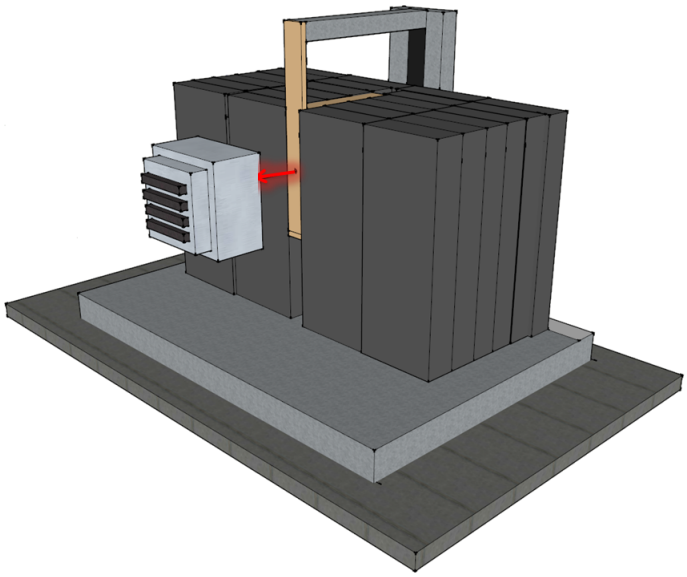

Figure 3.16: Full setup of the collimated ^{137}Cs source, with some lead bricks surrounding the source and the collimator.

The described collimator assembly can be moved in x and y directions. The grey plate labeled 1 in Figure 3.15 is able to be moved in x direction, while the grey arm labeled 2 in Figure 3.15, holding the collimator and frame, is movable in y direction. Hence, the $LaBr_3$ detector position is fixed and the collimator assembly is moving relative to the detector. The movable plate and arm (isel Electronics [77]) are controlled using a step motor controller software (isel-Controller C 10C-E/-A [78]) and allow to move the collimator and source in x and y axis in a limited range of 83 mm in x axis and 80 mm in y axis, enough to cover the complete detector surface. Using this software, the user can define an irradiation grid with as many positions as desired, by defining the starting point (0,0), the end point (x,y), the number of steps between these two positions or the distance interval between each irradiation position, and the time of irradiation (in each position).

The usage of the first setup (with the 1 mm collimator) will only briefly be described in this Master thesis, since it has already been studied by H. van der Kolff [53], where more detailed information can be found. For the spatial resolution measurements reported here, we started irradiating the detector with the collimated ^{137}Cs source using the collimator block with ø1 mm, 48 mm long, made of DENSIMET® shown in Figure 3.12. For these measurements, since the reduced setup was in use (with 64 channels), an 8×8 grid scan was realized by H. van der Kolff [53], as a starting point to characterize the spatial behavior of the $LaBr_3$ crystal. However, in order to apply the k-NN method to our scintillator, a much larger reference set derived from a 2D scan with a fine grid size would be needed in order to allow for a precise position reconstruction. This can only be achieved on the basis of a reference data set of light amplitude distributions that represent distances of the successive irradiation positions much smaller than the envisaged spatial resolution of $\sim$ 1-2 mm.

Consequently, a new collimator was built with a diameter of the collimation channel of 0.5 mm. This collimator is not a solid block of DENSIMET® as for the ø1 mm collimator, since it is not possible to drill such a small opening into a 48 mm thick block. Hence, twelve 0.4 mm thick DENSIMET® slabs were locally manufactured, drilled and aligned through two internal steel positioning rods (with an estimated relative tolerance of about 10-30 μm), as displayed in Figure 3.17. The alignment of the holes was verified with a 0.3 mm steel wire, able to slide freely through the hole in the stacked DENSIMET® slabs.

The methods for mounting the source and the collimator inside the frame are the same than described for the assembly displayed in Figure 3.13, where only the collimator block of ø1 mm was replaced by the ø0.5 mm collimator with 12 slabs.

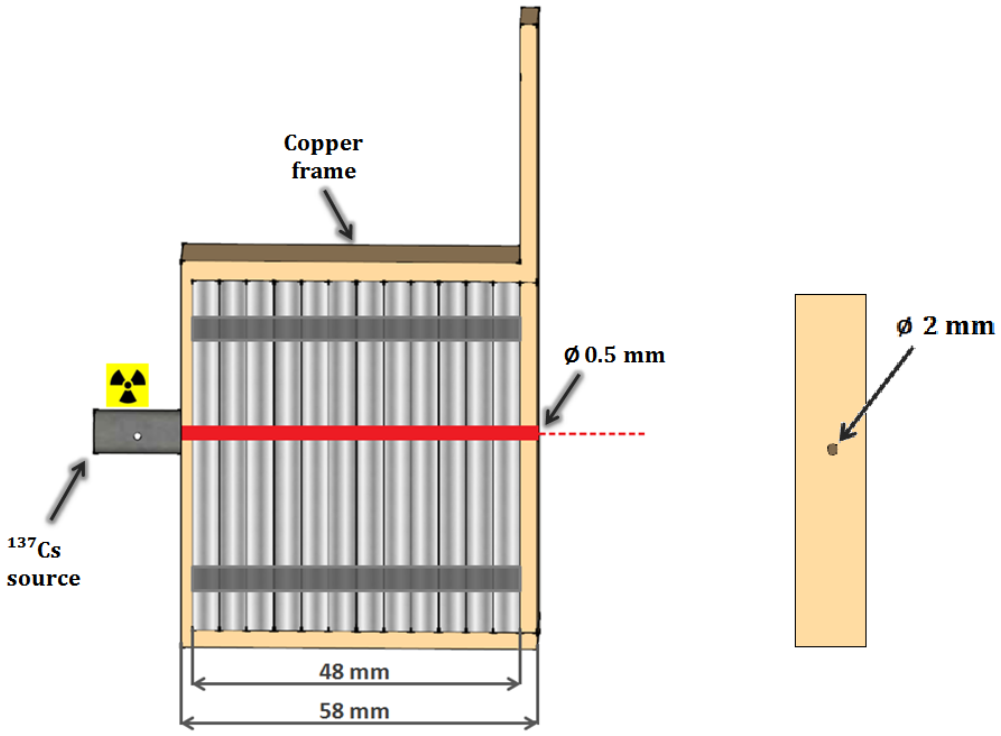

Figure 3.17: 0.5 mm (in diameter) collimator design specifications, with the ^{137}Cs source on the back side, and a front view of the collimator frame (with 2 mm diameter).

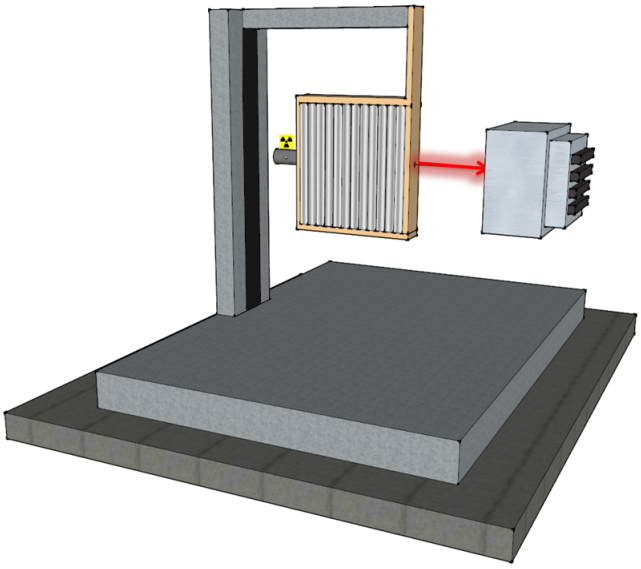

Figure 3.18: Setup of the collimated ^{137}Cs source without any surrounding lead bricks and with the radioactive source mounted at the back side of the 0.5 mm collimator block. Also here, the bottom plate and the arm are able to move in x and y directions in order to perform the 2D scan.

The same procedure as reported in [53] was repeated for the 1 mm collimator during this Master thesis, with a step size of 1 mm, because this collimator was only used to verify that the setup was working as expected, with the main objective being to start using the ø0.5 mm collimator.

For these measurements, the PMT supply voltage of the $LaBr_3$ was set to -830 V, in order to be able to reach a dynamic range of 8 MeV in the MQDC, applying individual gates for the MQDC channels. The starting point of the scan was defined at ∼5 mm before the edge of the detector, and the end point as lying ∼5 mm after the edge of the detector. Since the hygroscopic scintillation crystal is encapsulated in an aluminum housing, with dimensions indicated in Figure 3.19, these measurements also allowed to confirm the dimensions of the crystal, and to verify if the crystal was aligned with the center of the housing. Each position was measured for ∼ 20 seconds, in order to obtain enough statistics in the photopeak. In this way, we end up with a full-edge scan (in x direction) for the $LaBr_3$ absorber detector. The results obtained with the ø1 mm collimator are shown in Figure 3.20.*

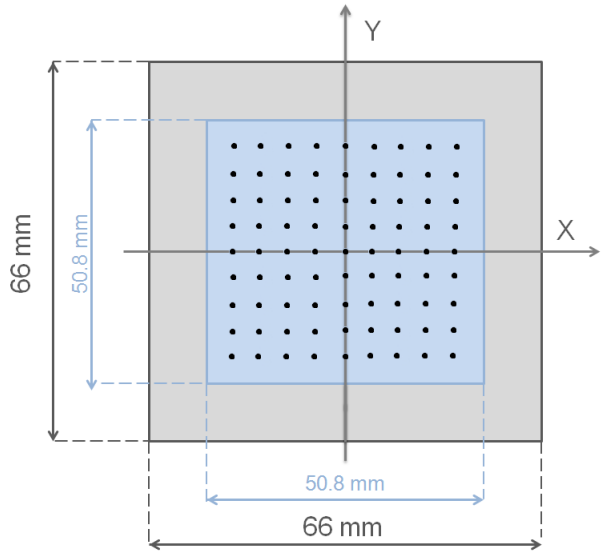

Figure 3.19: Front view of the $LaBr_3$ crystal (thickness = 30 mm), where the surrounding aluminum housing is indicated in grey. Drawn are the irradiation points for an 8×8 irradiation grid scan, where the irradiation points represent the collimated beam from the ^{137}Cs source.

*In this thesis, a scan of the border area of the crystal in one direction (either x or y) will be called "edge scan", while a scan of the full crystal dimension from one side to the other (either x or y direction) will be referred to as "full edge scan".

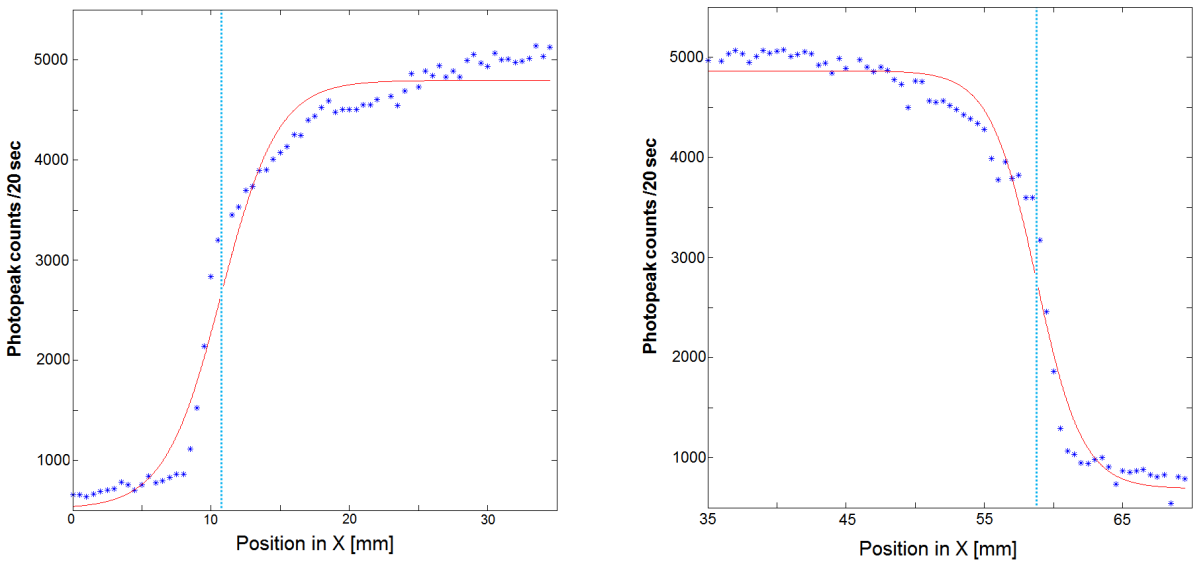

Figure 3.20: An inverse Fermi- and a Fermi-function were fitted to the rising and falling edge of the count-rate profile from a scan in x direction, respectively, using the ø1 mm collimator. The measurement was performed before the elaboration of this Master project [53]. The points of inflection are marked with the blue dashed lines, with a value of x = 10.73 and x = 58.76 mm.

The result meets the expectations, where the 662 keV photopeak count-rate starts with a flat distribution and a subsequent steep rise at the edge of the crystal, inside the aluminum cage. Then follows a plateau while irradiating the crystal. When the side edge of the crystal is reached, a corresponding steep drop of the count-rate is observed, as expected. The count-rate profile in both x and y directions is expected to follow approximately a Fermi-function (and inverse Fermi-function) distribution.

As mentioned above, the ø1 mm collimator will not be able to provide adequate data for the k-NN method with the envisaged spatial resolution, resulting in the need of a finer 2D scan step size and collimation diameter. A side-edge scan performed during this master thesis is represented in Figure 3.21.

With the new collimator (ø0.5 mm), we repeated the procedure that was used before. The result using the 12×0.4 mm DENSIMET® slabs is shown in Figure 3.22. Surprisingly, instead of an improved detection of the crystal edge, an even less clear edge profile was found.

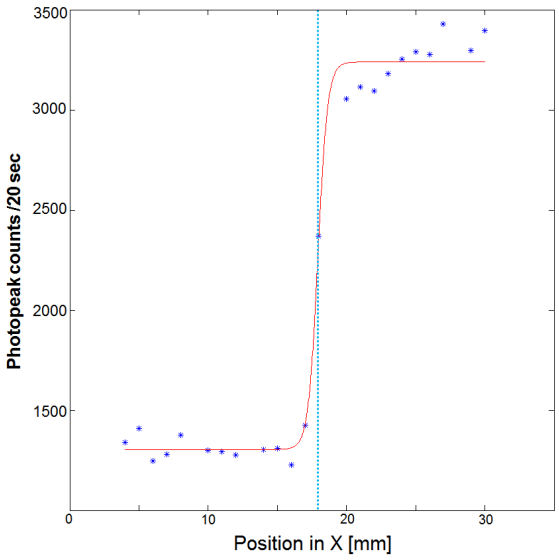

Figure 3.21: Inverse Fermi-function fitted to the rising edge of the count-rate profile of a 1 mm stepsize edge scan, crossing half of the detector width in the x direction, using the ø1 mm collimator. The inflection point is x = 17.93 mm.

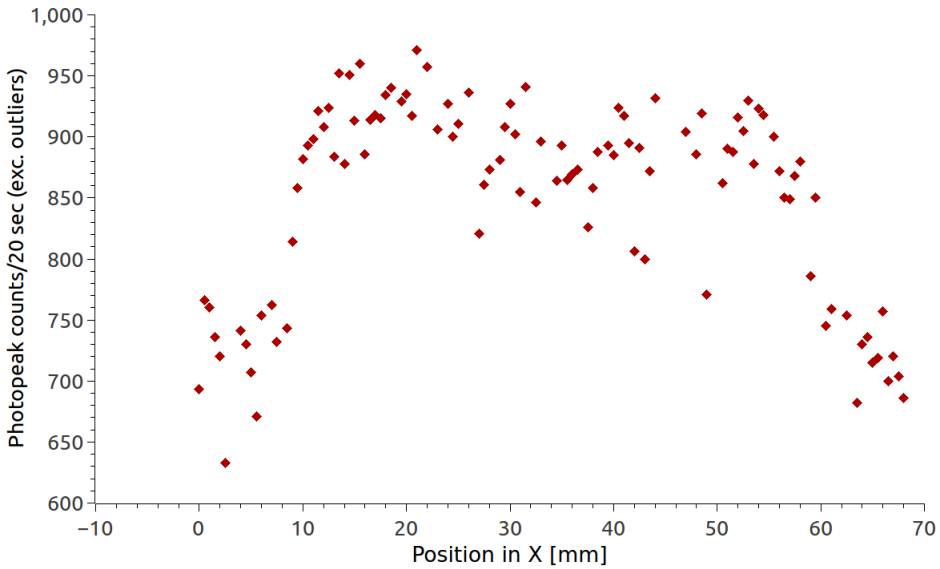

Figure 3.22: Count-rate profile of a 0.5 mm stepsize scan, crossing the detector in the x direction, using the ø0.5 mm collimator. The Fermi-function fit is not applicable to this distribution, since no clear correlation can be seen due to obvious scattering effects arising from the narrow collimator assembly for potential source misalignments.

As shown in Figure 3.22, no clear correlation between the irradiation position and the shape

of the detected count-rate profile could be seen, unlike with the ø1 mm collimator . In order to clarify the reason for this blurring of the measured count-rate profile, both the source and the properties of the new collimator had to be checked. First, the previous setup using the ø1 mm collimator was used to investigate the alignment of the source position.

The position of the active source area inside the tantalum cylinder was not precisely known, because the active area is encapsulated in the stainless steel cylinder and is not visible from the outside. So we decided to check if the active area was aligned to the collimation channel (2 mm in diameter) in the tantalum cylinder, where the photon beam was supposed to pass through. In Figure 3.12,(3) represents the channel housing the stainless steel cylinder where that surrounds the source. This cylinder can be moved inside the channel to the left and right. The aim is to align the active area of the source ((5) in Figure 3.12) with the collimation channel (4). Figure 3.23 illustrates this procedure of moving and flipping the source. The results from these measurements moving the source to the sides are listed in Table 3.5 and displayed Figure 3.24.

Figure 3.23: Sketch of the approximate displacement of the source. (a) positions 1/3/5; (b) positions 1/3/5 after flipping the source by 180°. As visible in the figure, in the initial position the active source area is aligned to the collimation channel.

Photopeak counts/20 sec	Position of the source
68	No source
2737	1
2600	2
2434	3
2263	4
1713	5
610	Flipped - 1
908	Flipped - 2
1008	Flipped - 3
1123	Flipped - 4
1500	Flipped - 5
2253	1
2110	2
2085	3
2071	4
1611	5

Table 3.5: Photopeak count-rate for each source position, where position 1 is the when the cylinder is in its maximum x position inside the tantalum shielding, 2-5 correspond to successive horizontal shifts by $\sim$1 mm towards the outside edge. For the flipped positions, the stainless steel cylinder was removed and flipped by 180°, and the same procedure was repeated. The last 5 positions were measured in the same conditions than applied for positions 1-5, in order to check the reproducibility of the first measurement series. A background measurement with the source removed was also performed.

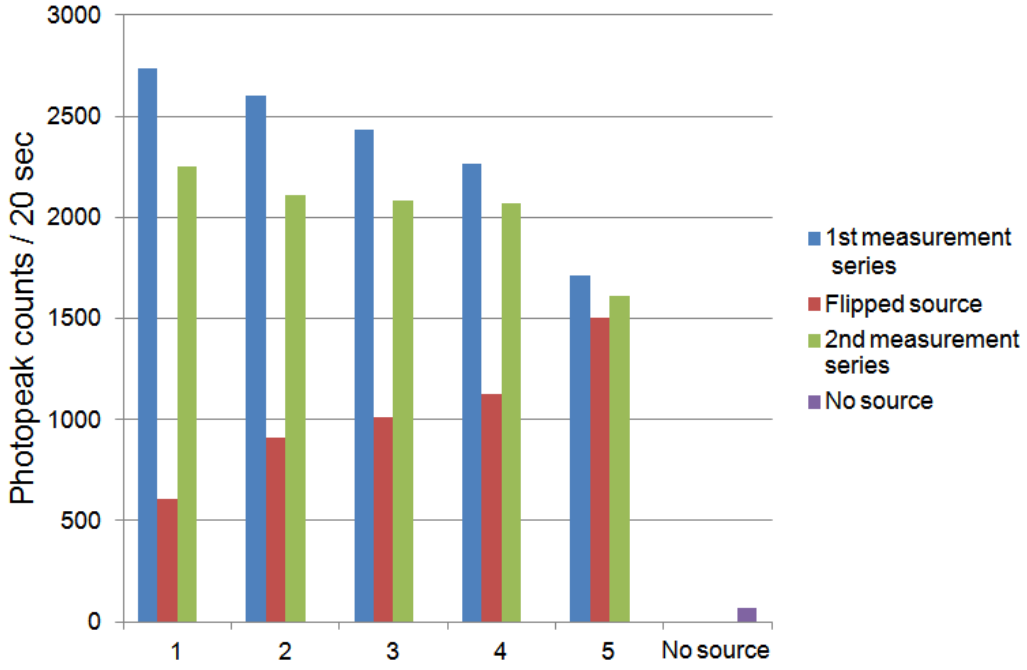

Figure 3.24: Photopeak count rates for different horizontal positions of the ^{137}Cs source, including the source flipped. Also a background measurement was performed, where the source was removed.

From these measurements, one can see that the optimum active source area is the initial position (position 1), since the photopeak counts/20 seconds are higher than for the other positions (2-5 and Flipped 1 - flipped 5), as it can be clearly seen in Figure 3.24. In fact, when flipped, the photopeak counts/20 seconds decrease drastically, since the active area of the source is then far from the collimation channel inside the tantalum cylinder. After taking a second measurement, as shown in Table 3.5 and Figure 3.24, this hypothesis is verified and we assumed that the initial position is the correct position for the active area of the source, and we continued the spatial resolution measurements accordingly. However, this second measurement showed that the count-rate values are significantly lower than during the first measurement. Since they are lower than $\sqrt{N}$, than can be assumed as fluctuation, one can only conclude that there should have been a slight displacement of the source relative to the first measurement. Nevertheless, since there was no direct way to measure the correct source position, the source was pushed to the maximum x position inside the tantalum shielding and assumed to be in the correct position.

Once having determined the correct source position, we decided to work with the ø1 mm collimator, but to add in front of it several slabs from the 12×0.4 mm collimator setup with 0.5 mm in diameter. So, we started out from using 1 slab, and gradually added slabs until 4. The arrangement (displayed in Appendix B) was the same as before, but the ø1 mm collimator was placed at the back side, with the slabs of ø0.5 mm collimator added in front of it, in order to achieve a better photon collimation. As before, the collimators were supported by the copper frame. The results (from 1 to 4 slabs) are shown in Table 3.6.

	Background [counts]	Photopeak counts	P/B (%)
1 slab	290	124	42.8
2 slabs	287	80	27.9
3 slabs	180	60	33.3
4 slabs	213	27	12.7

Table 3.6: Peak-to-background ratio (P/B), calculated using the background counts and the photopeak counts, for a collimated ^{137}Cs source, where successively 1-4 with 4 mm thickness DENSIMET® slabs with a 0.5 mm hole were added in front of the 48 mm thick collimator (with 1 mm collimation diameter). The measurements were done for 20 seconds.

The results shown in Table 3.6 were obtained from the measured energy spectra using the $LaBr_3$ detector. Using *HistPresent*, the integral of the peak was determined (from where the photopeak counts were obtained), as well as the number of background counts (to the integral of the total spectrum, the photopeak counts were subtracted). These results allow to conclude that from 1 to 4 added 0.5 mm collimator slabs, the peak-to-background ratio of the ^{137}Cs photopeak gradually degraded when more slabs were added in front of the ø1 mm collimator.

The count-rate profile for 1 and 4 slabs is displayed in Figures 3.25 and 3.26, with the respective Fermi- and inverse-Fermi function fits superimposed to the data (alternative measurement results for 2 and 3 slabs can be found in Appendix C).

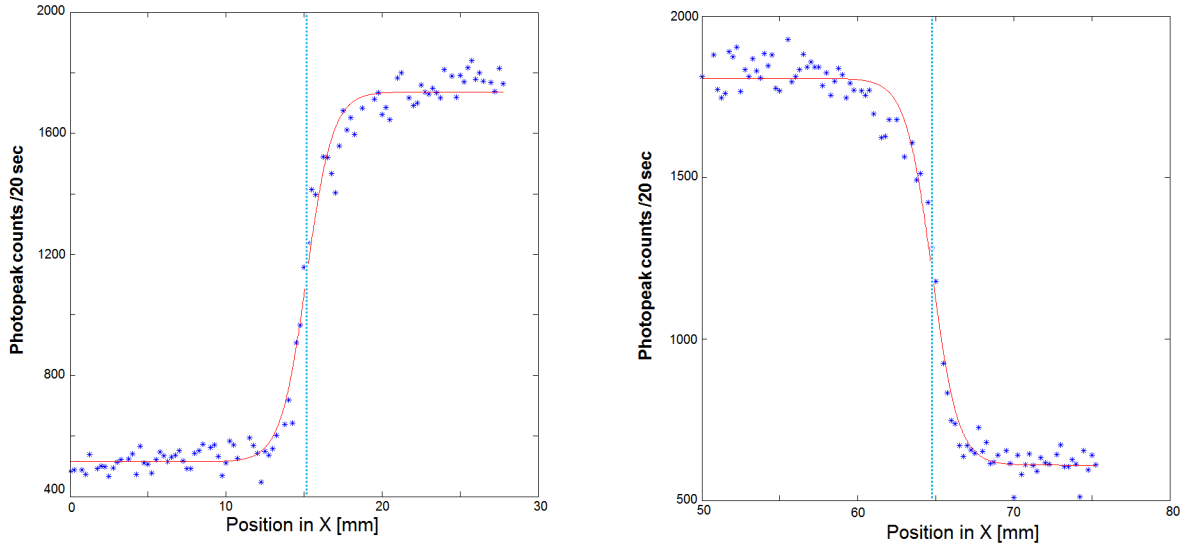

Figure 3.25: An inverse Fermi- and a Fermi-function were fitted to the rising and falling edge of the count-rate profile from a scan in x direction, respectively, using the ø1 mm collimator and 1 additional slab of the ø0.5 mm collimator. The points of inflection are marked with the blue dashed lines, with a value of x = 15.16 and x = 64.75 mm.

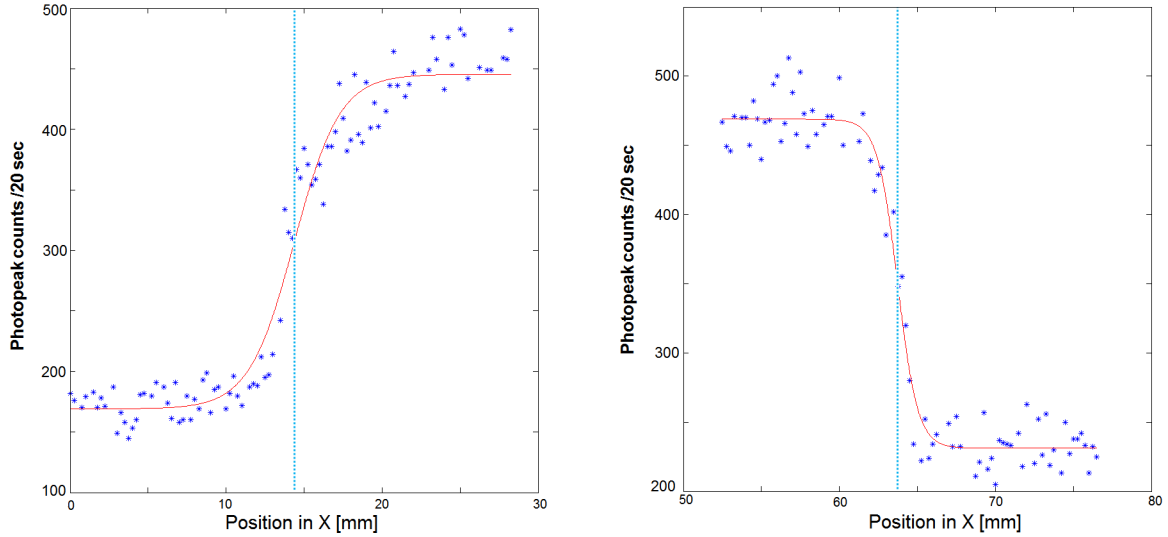

Figure 3.26: An inverse Fermi- and a Fermi-function were fitted to the rising and falling edge of the count-rate profile from a scan in x direction, respectively, using the ø1 mm collimator and 4 slabs (i.e. 16 mm thick) of the ø0.5 mm collimator in front of it.

The inflection points of the Fermi and inverse-Fermi fits are used to calculate the dimensions of the crystal, since these should be the x coordinates where the crystal starts (x_1) and ends

(x_2). This function fit is the best fit that could be done to this type of data, however, so far, the results are not according to the expected dimensions of the crystal. This may be due to the scattering caused by the 0.5 mm collimator slabs, that worsen the accuracy and therefore lead us to unexpected results.

The fits were done using the Fermi function equation parametrization, which is derived from the Fermi-Dirac distribution function:

$$f(x) = \frac{1}{1 + exp\left((x_i - x)\right)/(K))} \tag{3.6}$$

where x_i represents the inflection point, and K is a constant that represents the slope [79]. The parameterizations are, accordingly:

$$x1 = A + \frac{B}{\exp\left((x_0 - x1)/K\right) + 1} \tag{3.7}$$

and respectively, the Fermi function equation:

$$x2 = A + \frac{B}{\exp\left((x2 - x_0)/K\right) + 1} \tag{3.8}$$

where A corresponds to the offset of the Fermi and inverse-Fermi function, B is the yield value corresponding to x1 (respectively x2), K is a constant that represents the slope and x1 (respectively x2) is the inflection point of the function. The results from these Fermi function fits are represented in Table 3.7.

Number of 0.5 mm slabs in front of the 1 mm collimator	x_1 [mm]	x_2 [mm]	Crystal size (x_1 - x_2) [mm]
1 slab	15.16 ±0.12	64.75±0.13	49.59±0.3
2 slabs	14.8±0.15	64.25±0.15	49.45±0.3
3 slabs	12.09±0.14	61.45±0.20	49.36±0.3
4 slabs	14.38 ±0.20	63.74±0.18	49.36±0.4

Table 3.7: Results of the Fermi and inverse-Fermi function fits for 1-4 slabs of 0.5 mm (in diameter) in front of the ø1 mm collimator. It can be seen that, since the crystal dimensions are close to ∼50 mm, adding more slabs accuracy of the crystal edge definition is lost and the results from calculating the crystal dimensions deviate from the expected value.

One direct indicator of the accuracy loss is the error, which is increasing when adding more slabs (from 1 to 4). Also, since the dimensions of the crystal are given by the manufacturer as 50.8×50.8 mm^2, the values derived here significantly underestimate these dimensions. So one may conclude, that during the polishing procedure the crystal had undergone during a repair period at Saint-Gobain, a thin layer of the crystal material had been removed, at least partly accounting for the difference observed from the crystal dimensions determined here and the data sheet values of the manufacturer.

When adding more than 4 slabs, the result becomes similar to the result from Figure 3.22. However, using only 16 mm of 0.5 mm collimation is not enough to achieve a well collimated γ beam with 0.5 mm diameter. Moreover, another source of alignment uncertainties was attributed to the copper frame, which is, as mentioned before, not firmly attached to the collimator, thus slight sideways movements cannot be excluded. So a new frame was designed, which allows to attach the collimator to the frame, in order to have more stability and minimize a possible source of error. For the near future also the construction of a new collimator is foreseen, using a different manufacturing technique, to avoid potential misalignments between the 12 DENSIMET® slabs by using a monolithic design (potentially 2 horizontally aligned halves). Further investigation of the ø0.5 mm collimator using the new frame is still ongoing work.

3.6 Scatter detectors: DSSSD and Gassiplex readout system

After having described the absorber detector of the Compton camera, the following section will be dedicated to the description of the scatter component, which in our case consists of an array of DSSSDs, conceptually introduced in Section 2.4.1. In this section, the design specifications of the DSSSD and their readout system are explained, as well as the characterization of the DSSSD and preliminary results obtained from these particle detectors.

3.6.1 Design and readout of the DSSSD

For the Compton camera setup, a stacked array of six of such position-sensitive detectors was used, motivated by the aim to enable a tracking of the Compton-scattered electrons

across the various layers of silicon detectors. The 6 DSSSD modules are each separated by a distance of 1 cm. This distance was chosen from results obtained through Monte-Carlo design specification simulations for a realistic scenario, such as the imaging of a small animal, with a distance of 5 cm between the source and the first detector layer [48]. If the Compton-scattered electrons cross more than one detector layer, when their energy deposits and interaction positions are detected, this allows for a more efficient γ-source reconstruction, reducing the Compton cone to an arc segment (as shown in Figure 2.13). This allows for incompletely absorbed photon events to be included in the reconstruction process, whereas a pure γ tracking relies on complete photon energy absorption in the $LaBr_3$ crystal.

The silicon detectors were manufactured by the company CiS (CiS Forschungsinstitut für Mikrosensorik und Photovoltaik GmbH) [80], according to user specifications, based on simulations using the MEGALib event and image reconstruction code package [48]. The resistivity of the wafer material has been specified to be > 10 kΩcm, with a depletion voltage of $\approx$ -50 V. The specified leakage current is $< 1\mu$A at the depletion voltage of -50 V [48]. Even when the depletion voltage is increased to -75 V, the leakage current in all the detector modules is expected to stay below 1μA for ambient temperatures. The detectors have an active area of 50×50 mm^2 and a thickness of 500 μm ($\pm$25 μm). The sides of the silicon detectors are segmented into 128 strips on the n-side and 128 orthogonally oriented strips on the p-side, with a pitch size of 390 μm[48]. Therefore, each detector exhibits a total of 256 readout channels. As can be seen of Figure 2.10, these 256 signal readouts are organized such that the 128 strip contacts of each side are fed to 64-pin connectors at opposite sides of the printed circuit board housing the Si sensor chip. Odd and even channel numbers, respectively, are read out at the opposite sides. In the corners of the detector boards contacts are foreseen for the bias supply and for the guard ring of the detectors.

Obviously, a large amount of $6\times256=1536$ readout channels cannot be processed by individual electronics modules anymore, as it is done for the absorber crystal. Due to the complexity of the DSSSD array, a highly integrated Application-Specific Integrated Circuit (ASIC)-based readout system was chosen for the DSSSD signal processing. In 1995, "a family of integrated circuits (AMPLEX, GASPLEX and GASSIPLEX) has been developed for the readout of various types of detectors. The programmable VME readout can be used in conjunction with these chips" [81]. For our scatter/tracker array, the readout system is based on the GASSIPLEX chip. The GASSIPLEX chip, able to process 16 signal channels, is composed of several functional blocks, comprising for each channel a Charge-sensitive pre-amplifier (CSA) that collects the largest part of the detector signal, a shaping

filter amplifier, that provides a semi-Gaussian signal and, a track-and-hold circuit that has as the functionality to store the analog information and multiplexes this information to the subsequent digitizer stage before sending the final digital information to one of the 64 output channels of the front-end readout board. Hence, the output of this chip is a signal from one of its 16 channels, that was previously amplified, shaped, processed, stored and digitized [82] in a 10-bit multiplexed analog-to-digital converter.

The readout boards are connected to the 64-pin connectors of the detector board via AC couplers and each 6 readout boards at one side of the sixfold detector stack are connected to a motherboard that collects the data and transfers them to the VME-based readout controller.

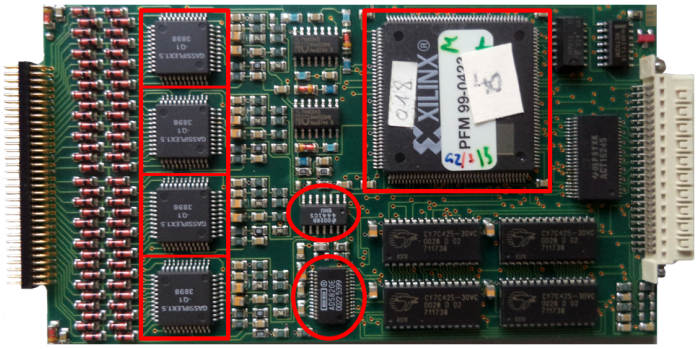

Figure 3.27: 64-channel readout board based on the GASSIPLEX chip. From left to right, one can see GASSIPLEX chips (marked with the red squares), the multiplexer and shaping amplifier stage, and ADC (marked with red ellipses), and the field-programmable gate array (FPGA) (in the red square). Figure adapted from [48].

One front-end readout board that is shown in Figure 3.27 contains 4 GASSIPLEX chips (indicated by the red squares), where each one is able to read out 16 channels, thus a total of 64 channels can be processed per readout board. The boards are connected to the DSSSD through an AC coupler that isolates the circuit from the bias voltage applied to the detectors, thus protecting the electronics. This AC coupler contains a 10 MΩ input resistor for each of the 64 channels and a 10μF coupling capacitor that protects the circuit from the reflux current of the bias voltage. The detector is protected by a 1 MΩ resistor, that restricts the maximum current to the range of μA [48].

In general, the reverse bias potential, which is necessary to fully deplete the silicon detector, can be applied in several ways [83]:

- By applying a positive high voltage on the n-side and ground potential to the p-side;
- By applying a negative high voltage on the p-side and ground potential to the n-side;

- By applying a splitted bias voltage, sharing the total potential between both sides.

In our case, the n-side is coupled to ground potential, while the p-side is coupled to the negative bias voltage.

4

Online characterization of the Compton Camera

The components of the Compton Camera were set up, tested and calibrated independently. The full Compton camera setup consists of the combination of the 6 DSSSD layers as scatter/tracker detector, the $LaBr_3$ as absorber detector, together with their associated signal processing electronics. The integration of this camera prototype will be introduced in the forthcoming chapter, together with first online characterization measurements.

4.1 The Compton Camera Setup

The current prototype setup of the Compton Camera has been completed to have its full operational capability by integrating the detector components, adding parts for support, shielding and thermal control. This full setup, including the 6 layers of DSSSD and the $LaBr_3$ absorber detector, is shown in Figure 4.1(left panel). All detector components were mounted to a support structure assembled from a modular aluminum profile system (further information can be found in [84]). Here, the flexibility of the geometrical positioning is high, allowing for different geometries, with the $LaBr_3$ detector and the DSSSD being mounted with position millimetric precision. This support structure was finally used as the basis of the setup operated also during online characterization experiments at the Garching Tandem accelerator. Figure 4.1 shows the arrangement used during the beamtime in April 2014, where the aluminum bars are visibly holding the six DSSSD layers.

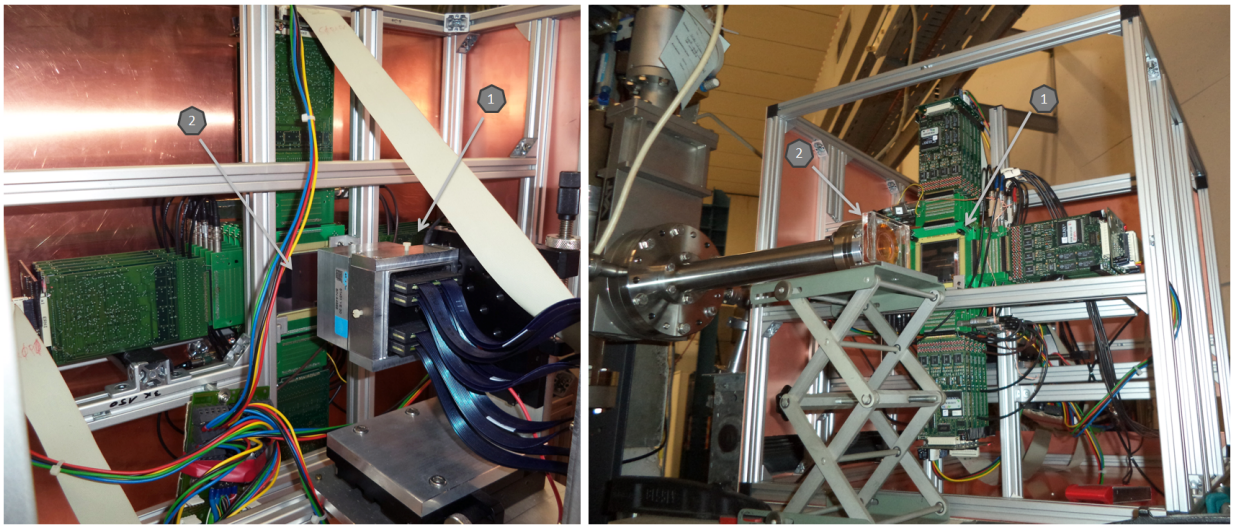

Figure 4.1: Left: $LaBr_3$ absorber detector (1) is carefully placed behind the DSSSD, and the DSSSD array (2) precisely positioned inside the shielding cage, in front of the entrance window. Right: A modular aluminum profile system supports the DSSSD array on the front side (1) and $LaBr_3$ detector mounted behind the DSSSD (not visible). (2) represents the rectangular water phantom, used in the Tandem accelerator experiment in April 2014.

After mounting the detectors in the aluminum frame, all Compton camera components were housed in a light-tight container box, which can be seen in Figure 4.2, and its interior in Figure 4.1. The primary purpose of the light-tight cage is to shield the light-sensitive silicon detectors from external light, which would immediately drive them into saturation. In addition, the camera cage serves as Faraday cage, which allows to block external electric fields, providing constant potential on all sides of the cage and banning electromagnetic fields from entering inside. The Faraday cage was composed of copper-coated epoxy boards (1.6 mm thick), taken from standard printed-circuit board material, except the front plate, which is entirely made of copper.

Figure 4.2 shows the most recent setup, from the proton beamtime experiment realized in June 2014, including the rack with the signal processing and data acquisition electronics, as well as the support stand, where the Compton camera is placed on the top. This support stand gives some flexibility, since it exhibits 3 sub-stands, that can be adjusted along the vertical axis, allowing for placing the Compton camera in the right height for various experimental requirements (for example, at different accelerator facilities).

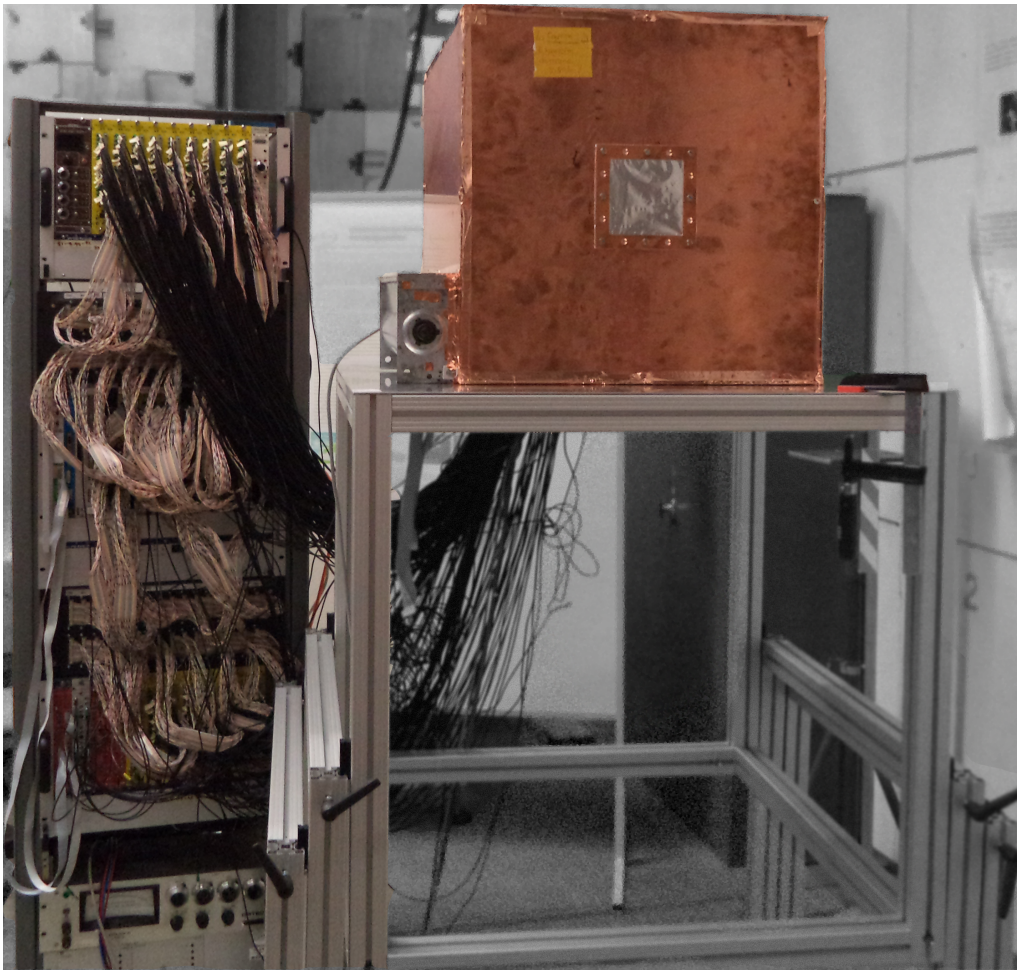

Figure 4.2: Compton camera prototype (housed in a light-tight Faraday cage) together with its signal processing and data acquisition electronics.

As visible, the Faraday cage is a cube (dimensions $61\times54\times54$ cm^3), with an entrance window on the front side mounted to a copper frame (and closed with an aluminum foil of $\sim$500 μm). This window was introduced in front of the DSSSD detector surface to minimize any potential scattering distortions of the incident photons. Furthermore, the cage contains two more openings: one on the left side, where a fan unit is attached (explained below) and another one to send the signal cables to the subsequent electronics. These openings have also been carefully sealed to be light-tight. The edges of the cube, where the epoxy boards touch each other, were all sealed with a copper tape with conductive adhesive, such that the Faraday cage was closed on all sides.

Another critical issue that needed to be addressed concerns the temperature inside the Faraday cage, taking into account that the leakage current of any detector system depends

on the ambient temperature [85]. With its 256 channels for the scintillator and the 1536 signal channels of the DSSSD array, the complex readout system potentially leads to a heating problem inside the cage, due to the high amount of electronics. Two PT-104 temperature sensors were installed inside the cage, on the left and right sides. The data from these temperature sensors are read by a four-channel data logger (PT-104 Platinum Resistance Data Logger from pico® Technology). This high-accuracy (0.015 °C) and resolution (0.001 °C) device allows to measure temperatures from -200 °C to +800 °C [86]. With these two temperature sensors, the temperature development inside the camera cage was continuously monitored as a function of time, and the resulting temperature curves are displayed in Figure 4.3 (a). The leakage current was also registered for the same time intervals, in order to observe the relationship between temperature increasing and leakage current. The leakage current was measured for the first DSSSD layer, and is represented in Figure 4.3(b).

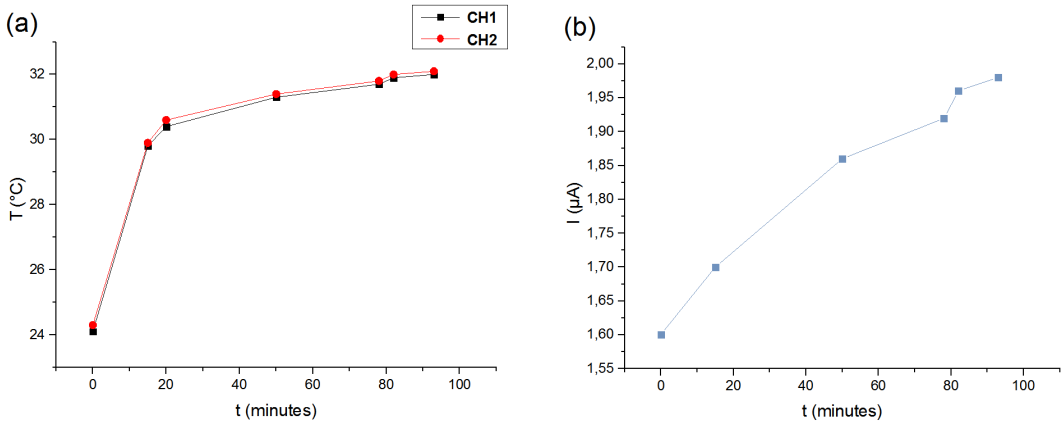

Figure 4.3: (a) Temperature measured inside the Compton camera Faraday cage as a function of time (starting at t=0 after powering the electronics) (CH1 and CH2 represent the 2 thermosensors); (b) Leakage current of the first DSSSD layer as a function of time, where I represents the leakage current in μA, before the intallation of the fan.

In Figure 4.3(a), it can be seen that the temperature, starting at 24.1 °C (and 24.3 °C, respectively), increases abruptly after powering the electronics, but continues rising after the first 15 minutes (however with a smaller slope). Figure 4.3(b) shows that the leakage current is increasing with temperature, starting from a value around 1.6 μA for ambient temperatures. Nevertheless, one needs to take into account that this measurement was performed after having the electronics turned on for 30 minutes, then turned off, so it was expected that the starting value for the leakage current was higher than the normal value (below 1 μA, as explained in Section 3.6.1) because the starting point was already well above 1 μA.

The leakage current negatively affects the performance of the DSSSD [87, 88], because a high leakage current results in a noise contribution and thus the energy resolution worsens [89]. Figures 4.3(a) and (b) allow to conclude that, as trivially to be expected, the temperature rise inside the Faraday cage correlates with the corresponding rise of the leakage current without further ventilation precautions.

Hence, this led to the installation of a fan unit to ventilate the cage. Ideally, the DSSSD should be cooled, using a cooling system that could achieve at least 1-2 °C, in order to minimize the leakage current and improve the DSSSD performance [87]. In Figure 4.2, one can see the fan unit on the left side of the cage, tightly attached to the cage using copper tape and sealing of gaps, to maintain the cage's light-tightness. After installing the fan, the resulting temperature curve was measured for 120 minutes, and this measurement is shown in Figure 4.4, as well as the leakage current of the six individual DSSSD modules, shown in Figure 4.5.

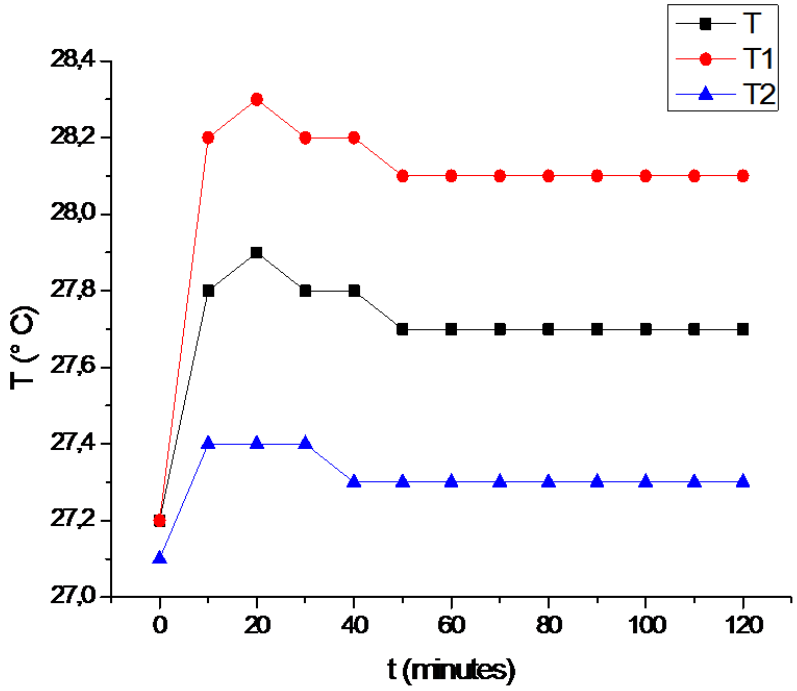

Figure 4.4: Temperature measured inside the Compton camera Faraday cage as a function of time (starting at t=0 after powering the electronics) (T1 and T2 are the 2 thermosensors and T is the average). This measurement was performed with the cooling fan already installed.

In Figure 4.4, one can see that the temperature slightly increases ∼0.2-1 °C after powering

the electronics. In fact, the installation of a cooling fan led to a maintenance of the temperature inside the cage, since the maximum temperature is ∼28 °C, reached immediately after powering the electronics. Although this can be considered a simple system for maintaining the temperature stable inside the cage, one can verify that this ventilation system works and preserves the temperature at an acceptable value for operating the DSSSD. This effect is visible in Figure 4.5, where the leakage current is shown for all the detector modules.

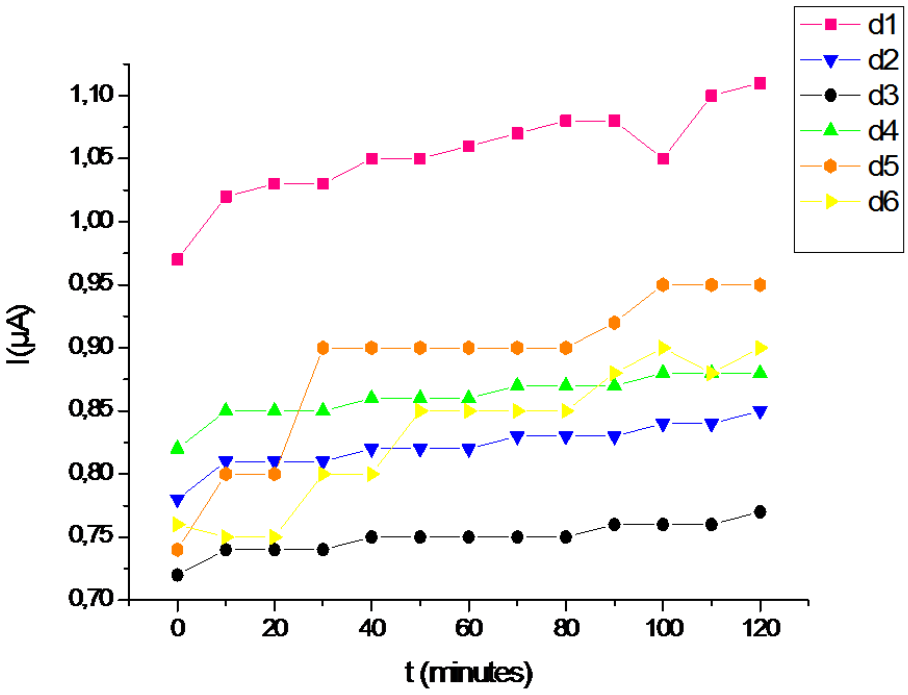

Figure 4.5: Leakage current of the six individual DSSSD modules as a function of time (where d1, d2, etc. represent the individual silicon layers) with the ventilation fan unit in operation.

Figure 4.5 displays the leakage currents of the six silicon detector layers of the tracking array measured as a function of time, starting at t=0 as used for the temperature measurements in Figure 4.4. As expected, here, since the leakage current was measured immediately after powering the electronics, the starting value is not 1.6 μA but well below 1 μA. Before, and without a ventilation system, the leakage current rose to values $\gg$1 μA immediately after powering the electronics, which is not verified here. A general trend of rising leakage currents with time is visible for all detectors, although after a longer period of time, as seen in Figure 4.6, the temperature stabilizes and even starts to decrease. Except for module 1, all leakage currents stay below 1μA, which is a reasonable value for the leakage current in the DSSSD

modules.

Moreover, the heating power of the electronics in the cage was measured by S. Aldawood [90], who verified that a relatively low temperature, after installing the ventilation fan, affects the heat load inside the cage. This measurement was performed using a power clamp, which via induction measured the current that flows in the power supply cable during operation of the electronics, and the obtained value was 38 W, a low value when compared with other similar experiments. The device used to measure the power consumption is Voltcraft, model VC605.

During the Tandem accelerator experiment, the temperature was measured for 100 hours, and is shown in Figure 4.6.

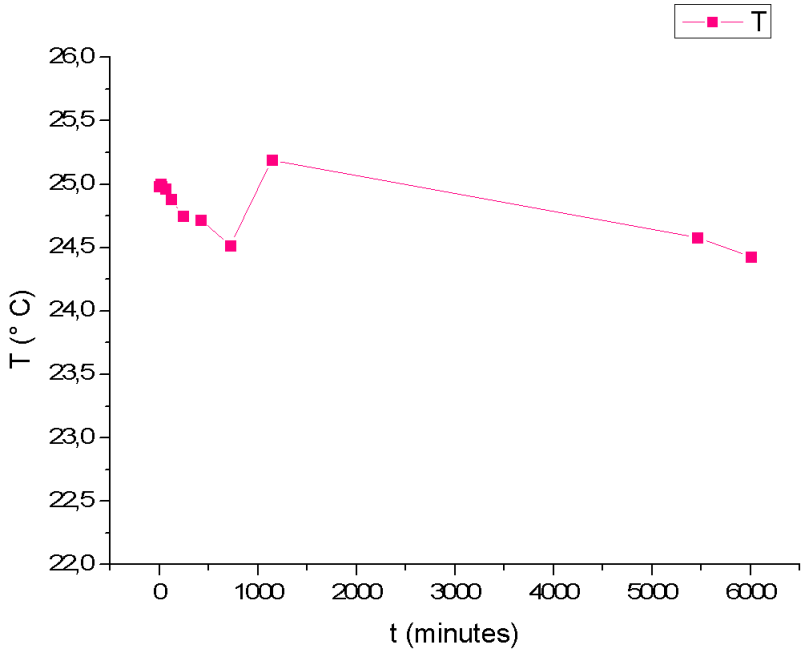

Figure 4.6: Temperature curve measured inside the Compton camera Faraday cage as a function of time after the installation of a ventilating fan unit, during the Tandem accelerator experiment in June 2014.

Here, the temperature was being measured by the thermosensors software via internet. Due to connectivity dificulties between the thermosensor logging station and the data acquisition hardware, a large gap is present in the data between ca. 1000 and 5000 minutes. On average, the temperature inside the detector cage could be kept below 25°C, and thus in a tolerable temperature regime for a safe and stable operation of the signal processing electronics. It will be evaluated in the future, if further active cooling is needed in order to reduce the thermal

electronic noise in particular of the GASSIPLEX-based silicon detector readout chain.

4.2 Experimental Setup at the Tandem Accelerator

All experiments using a proton beam performed during this thesis project were performed at the Tandem accelerator of the Maier-Leibnitz-Laboratorium (MLL) in Garching, a joint facility of the LMU and the TUM. The laboratory is used by several research groups from the Physics Departments at LMU and TUM. The largest unit of the MLL in Garching is the 14 MV Tandem Van-de-Graaff accelerator (Figure 4.7). It has been operating since 1970, and over the decades, the laboratory has become internationally known through its pioneering research in both fields of atomic and nuclear physics. Today, the accelerator remains essential for a variety of experiments, because it is a useful tool for generating ion beams with very good quality (energy variation, options for pulsing and polarization). This was possible due to the constant upgrading of the accelerator and its control network, keeping up-to-date with the actual state-of-the-art technology. Today, increasingly interdisciplinary research is being performed there, in the fields of nuclear physics, materials analysis, radiation biology and medical physics.

Figure 4.7: 14 MV Tandem-van-de-Graaff accelerator at the MLL in Garching [91].

The Compton camera was tested using a 20 MeV proton beam, provided by the Tandem

accelerator. The aim of the current work was not yet to reconstruct the photon source position, although this is the main aim in the near future using the MEGALib event and image reconstruction code package [48]. Such reconstruction requires the availability of position data from the absorbing detector. As described in Sections 2.5 and 2.6, this topic (i.e. applying the k-NN method) is still work in progress. The aim of the Tandem accelerator experiments has been, so far, to characterize the individual detector components of the Compton camera under online conditions in order to identify further improvement potential. During the first half of 2014, two experiments were performed: the first one, in April 2014, was performed using the reduced startup version of the $LaBr_3$ signal processing electronics with only 1/4 of the PMT readout segmentation (64 channels). The second experiment (June 2014) was performed already using the full $LaBr_3$ readout capability, with 256 channels.

Figure 4.8 displays the experimental setup, showing on the left side the evacuated beam line (1), which, behind a DN 100 gate valve, was reduced via a reducer flange (from DN 100 to DN 40)(2), ending in a DN 40 window flange (shown in Appendix B), where a 30 μm thick Kapton foil (15 mm diameter) served to seal the vacuum of the beamline from the outside atmospheric pressure. A cylindric water phantom (3) (water-filled PLEXIGLAS® cylinder, 30 mm long, 30 mm diameter) with an equally 30 μm thick Kapton foil entrance window foil served as tissue equivalent target for the production of the proton-induced prompt photons (a sketch of the phantom design can be found in Appendix A). During the beam tuning, instead of the water phantom, a scintillation crystal (CsI) was placed at the position of the beam exit to air, allowing to visualize the beam spot, which could be monitored with a CCD camera (4). The Compton camera cage was placed perpendicularly to the beam axis, centered to the water phantom, as visible in figure 4.8. For 20 MeV protons, the Bragg peak in water lies in a distance of $\sim$4.2 mm from the entrance window, as verified through a SRIM simulation. The Compton camera was aligned such that the Bragg peak position was placed in the center of the field of view (50×50 mm^2) of the Compton camera, centered behind the aluminum entrance window of the Faraday cage. In addition, the markers (5) and (6) in Figure 4.8 point to the ventilation fan of the Faraday cage and a vacuum tube connecting to the vacuum pump, respectively.

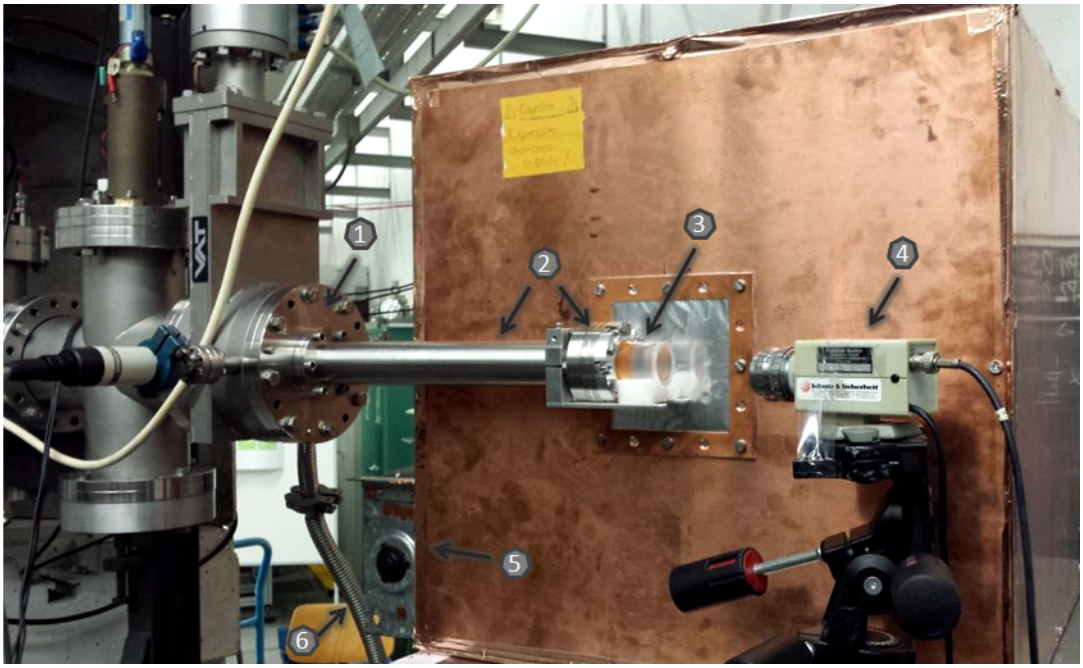

Figure 4.8: Setup used for the online measurements at the MLL Tandem accelerator, using a 20 MeV proton beam (entering from the left (1)) in a DN 100 vacuum tube that is reduced to DN 40 in front of the Compton camera (2), exiting to air through a 30μm Kapton window and hits a cylindrical water phantom (3). A CCD camera (4) can be used to monitor the beam spot on target position during beam focusing, when the water phantom is exchanged for a scintillating CsI crystal.

4.2.1 Energy pedestal corrections

Any analysis of digitized energy values, both from $LaBr_3$ and DSSSD detectors, first requires the determination of the digitized dark current of the digitizer, the so-called pedestal. This is of particular importance for the DSSSD readout, where only 10 bit dynamic range of the ADC is available. Using a -75 V depletion voltage for the DSSSD modules, the pedestal measurements were done before starting the experiment at the Tandem accelerator in June 2014. However, during the measurements, it turned out that the pedestal values were changing after a short period of time, most likely due to temperature changes of the readout electronics. Therefore, the pedestal measurements were periodically repeated.

The energy pedestal values were obtained from measurements without input signals entering the electronics. Typically, the pedestal peak follows a Gaussian distribution, thus centroid and width (σ) were determined via Gaussian fits to the pedestal peaks. Finally, a pedestal suppression was implemented in the analysis code, where the peak centroid plus a multiple

of the peak width σ was subtracted from the registered ADC value. This procedure was performed automatically for all the 1536 DSSSD channels and the derived pedestal subtraction correction factors were implemented for all the silicon layers.

We started out by using a $3{\cdot}\sigma$ pedestal correction factor for both n and p sides. However, it turned out that this pedestal correction was too small for the p side (Figure 4.9). Hence, the correction factor n was successively increased from 3 to $6{\times}\sigma$, which was the finally accepted value for the p side, as can be seen in Figure 4.9 (d). Here, the increasing suppression of the dark current (pedestal) peak can be followed from n=3 to n=6. The 2D projections of the pedestal are displayed in Figure 4.9, from the first layer of silicon detectors, channel 30 of the p side.

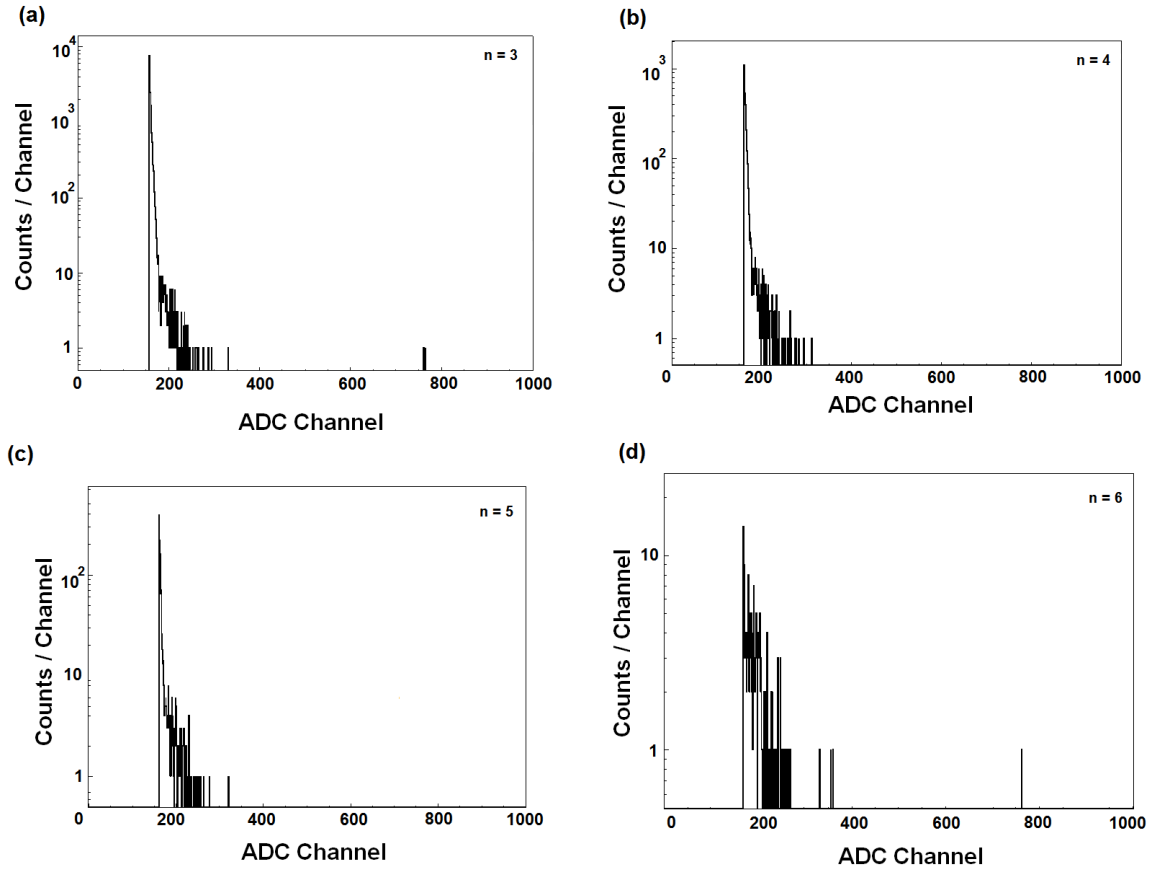

Figure 4.9: 2D projections of the pedestal for the first layer of silicon detectors (Channel 30 of the p side). The successive suppression of the pedestal peak is visible as a function of the correction factor $n{\cdot}\sigma$ for n=3 - 6 (σ being the variance of the initial pedestal peak).

A similar procedure was performed for the n side of the silicon detectors. The starting point was again a correction factor of $3{\cdot}\sigma$ which was then increased in parallel to the increase of the

n value for the p side, from n=3 to n=6. Here it turned out that a much smaller correction factor was sufficient, with an optimum value at n=3.5, as can be seen from Figure 4.10.

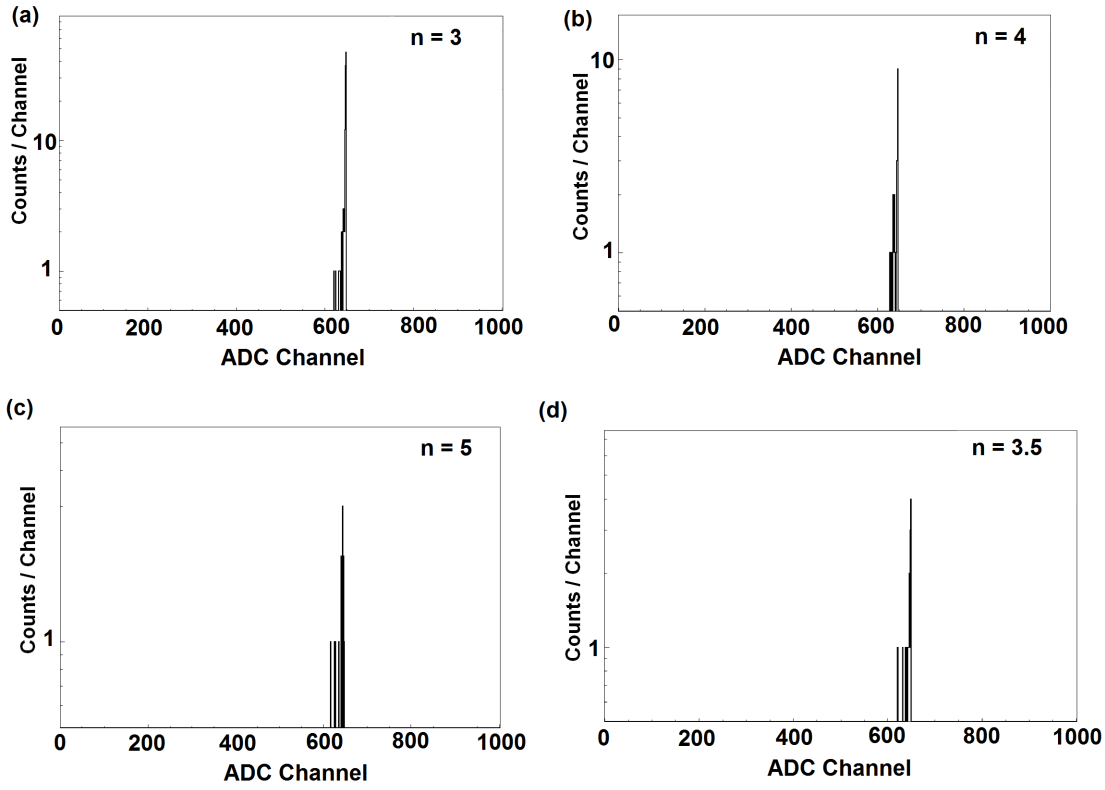

Figure 4.10: 2D projections of the pedestal for the first layer of silicon detectors (Channel 220 of the n side). The successive suppression of the pedestal peak is visible as function of the correction factor $n{\cdot}\sigma$ for n=3-5, where n=3.5 is the optimum value.

4.3 Results and Discussion

During the Tandem accelerator experiment, signals from both scatter and absorbing detectors were acquired. In the near future, once some improvements to the system are done and the reconstruction algorithms are ready to be used (mainly requiring the position information from the $LaBr_3$), one can track and reconstruct the photons and electrons resulting from the interactions of the water phantom with the proton beam. However, so far the setup is still working as two independent modules, the DSSSD and the $LaBr_3$ absorber detector. The signals collected from these detectors were independently analyzed.

4.3.1 DSSSD

The acquired signals from the Tandem accelerator experiments are presented in the following pages.

Figure 4.11 shows the signal from DSSSD 1 recorded during the Tandem accelerator experiment after implementing the adequate pedestal corrections. On the horizontal axis, the 256 channels (128 from the p side and 128 from the n side) are visible, and on the vertical axis the measured uncalibrated ADC value is shown.

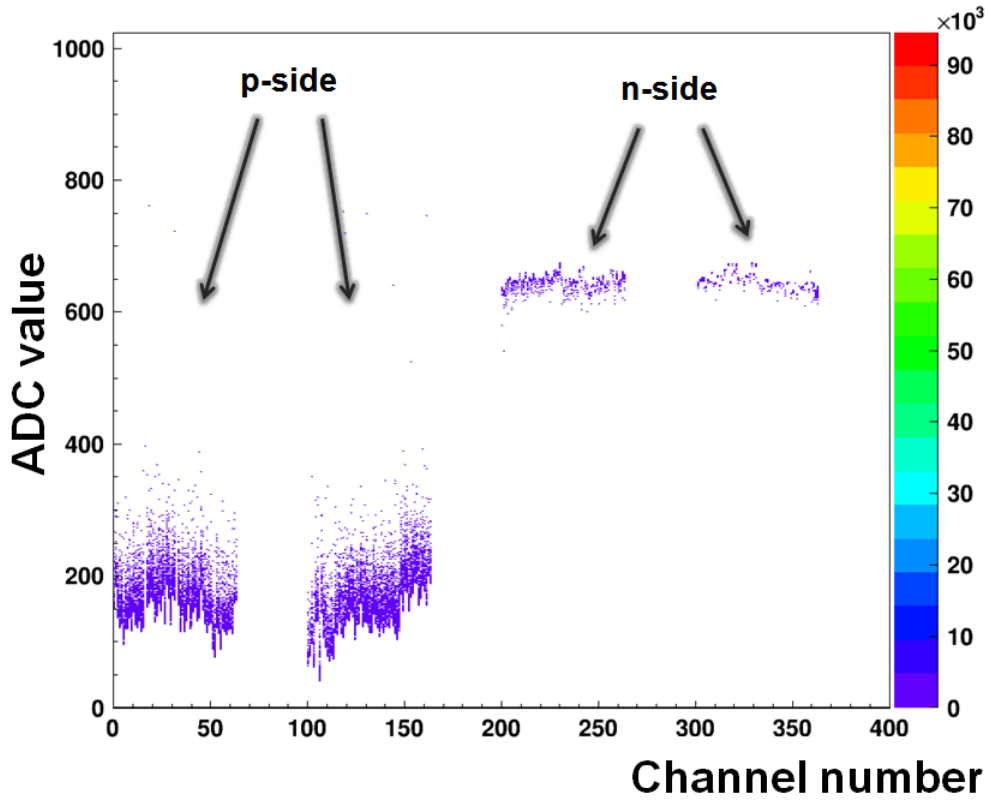

Figure 4.11: Uncalibrated γ ray energy spectra collected by the DSSSD modules of the first DSSSD layer, for the irradiation of a water phantom with 20 MeV protons. The first two structures, on the left, represent the 2×64 signal channels from the p side of the silicon detectors and the two structures on the right represent the corresponding 2×64 signals from the n side. The color scale denotes the intensity of the signal.

The display of the 256 channels of the detector module in Figure 4.11 is such, that the 64 channels of the odd and even strips of the respective n or p side are displayed starting with the display channel 1, 101, 201 and 301, respectively. As it can be seen, the n side baseline is located around channel 650. This reflects the fact that the GASSIPLEX chip was originally

designed exclusively for handling positive signals. In order to allow also for processing of the negative signals from the n side strips, the baseline had to be lifted to about channel 650 by an exchange of resistors. Unfortunately, a further shift upwards, which would be desirable in view of the usable dynamic range of the ADC, is not possible due to an otherwise saturation of the multiplexing amplifier.

Moreover, it turned out that in the present configuration the p side and the n side of the silicon detectors exhibit significantly different relative efficiencies (the dead-time and solid angle corrections for each layer are not yet implemented in this analysis), which also vary across the different detector layers.

Table 4.1 lists the comparison between the relative intensities measured with the two sides, while the 2D plot is represented in Figure 4.11.

DSSSD Layer number	**Total Entries**	Σ**(n)**	Σ**(p)**	Σ**(n)**/Σ**(p)**
1	118580	5192	113388	0.046
2	43170	2925	40245	0.073
3	51191	6930	44261	0.157
4	48418	3513	44905	0.078
5	56630	8143	48487	0.168
6	52669	4353	48316	0.090

Table 4.1: Comparison of the relative intensities for the n and p sides of the 6 DSSSD modules, with a bias voltage of -75 V, after pedestal supression.

From Table 4.1 one can conclude that the efficiencies of the n and the p sides unexpectedly differ by about a factor of $\sim$20. In fact, the p sides show an $\approx$20 times higher efficiency. In order to test the possibility that the bias voltage had been chosen too low, resulting in a not fully depleted detector volume, the bias voltage was increased from -75 V to -85 V. A similar analysis to the one shown in Table 4.1 provides the numbers of (pedestal corrected) entries in the spectra of the n and p sides, respectively, for the six detector modules as listed in Table 4.2.

Layer number	Total Entries	Σ(n)	Σ(p)	Σ(n)/Σ(p)
1	116789	5674	111115	0.051
2	43649	2720	40929	0.066
3	51695	6777	44918	0.151
4	48667	3255	45412	0.072
5	56568	7856	48712	0.161
6	52781	4028	48753	0.083

Table 4.2: Comparison of the relative intensities for the pedestal-corrected n and p sides, with a bias voltage of -85 V.

As one can infer from a comparison of Table 4.2 with Table 4.1, the relative efficiencies remain approximately the same. However, the leakage current increased, exceeding a value of 1 μA, as expected for operating the detectors with larger bias voltage. Therefore, and in view of the unchanged efficiencies, it was decided to keep the bias voltage at the original value of -75 V.

The origin of this unexpected and unfavorable behavior of the DSSSDs and their signal processing electronics is not yet understood and is subject to ongoing studies. One reason for such differences in the efficiencies of the n and p sides of the DSSSD modules could be that the multiplexing amplifier is operating, for the n side, already in saturation, induced by the shift of the baseline to +2.85V. This hypothesis will be tested with a new, modified, readout board, with a baseline lowered to ∼2.6V.

4.3.2 Prompt γ ray energy spectra

The prompt γ ray energy spectra were measured by the $LaBr_3$ absorber detector, by irradiating a water phantom with ∼20 MeV protons. The Compton camera was mounted under an angle of 90 °relative to the beam line, and also an angle of 0 °was tested during the Tandem accelerator experiment in April 2014. The prompt γ ray energy spectra displayed here (Figure 4.12 and Figure 4.13) were calibrated using the energy calibration represented in Figure 3.9, via a linear fit, where only energies up to 1.3 MeV were included (as obtained from standard calibration sources).

Therefore, significantly deviations from the "'true" photon energies beyond the range of the calibration points due to non-linear effects can be expected.

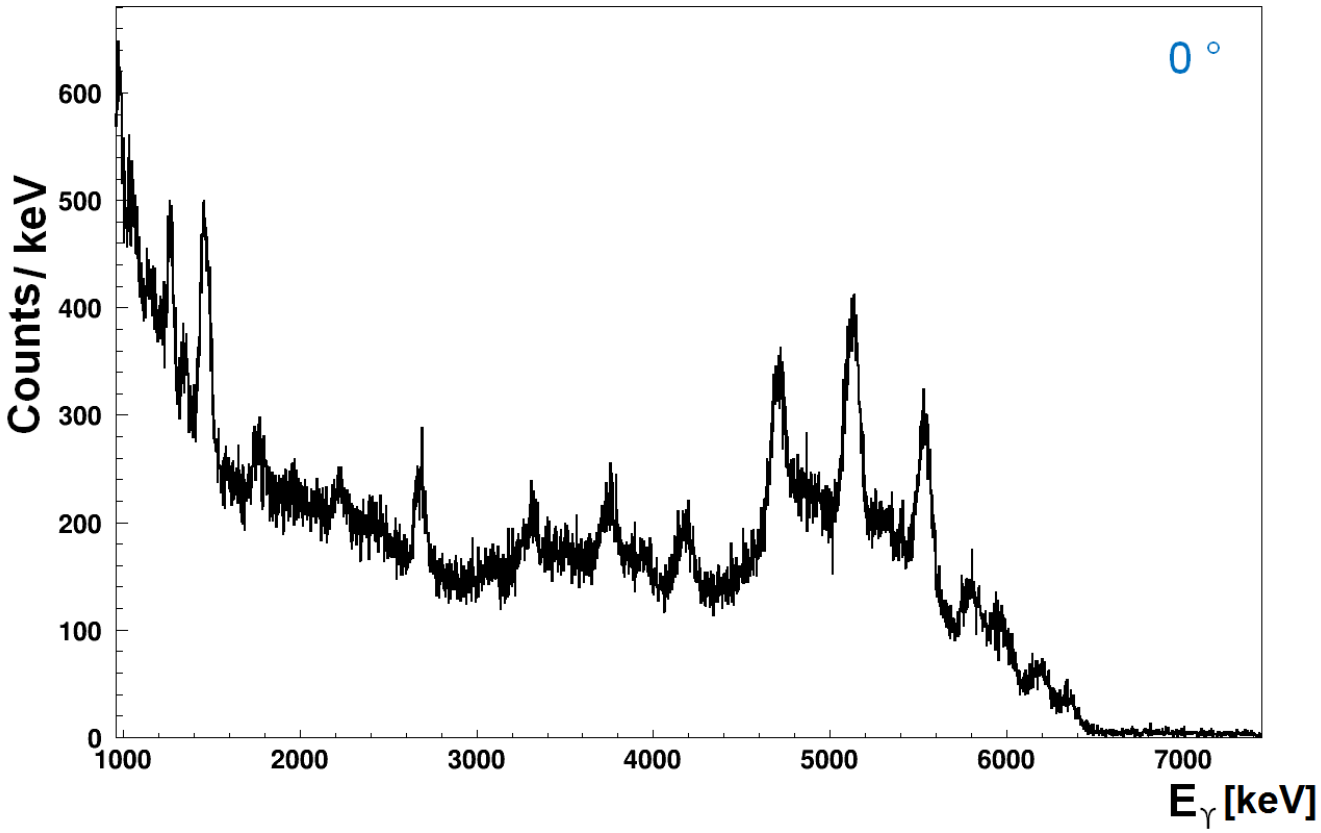

Figure 4.12: Calibrated measured prompt γ ray energy spectrum from the irradiation of a water phantom with 20 MeV protons using the $LaBr_3$ detector in April 2014. The Compton camera was mounted under an angle of 0°relative to the beam line. The energy calibration only includes energies up to 1.3 MeV.

The detector position at 0°relative to the incident beam was chosen to search for the significance of neutron background, predominantly emitted in forward directions. No significant differences can be observed between Figure 4.12 and Figure 4.13, where the γ ray energy spectra are shown for the two alternative camera positions at 0°and 90°, respectively. This means that for $E_p = 20$ MeV, neutron background contributions from neutron-induced (n, γ) reactions only negligibly contribute to the prompt γ ray energy spectrum.

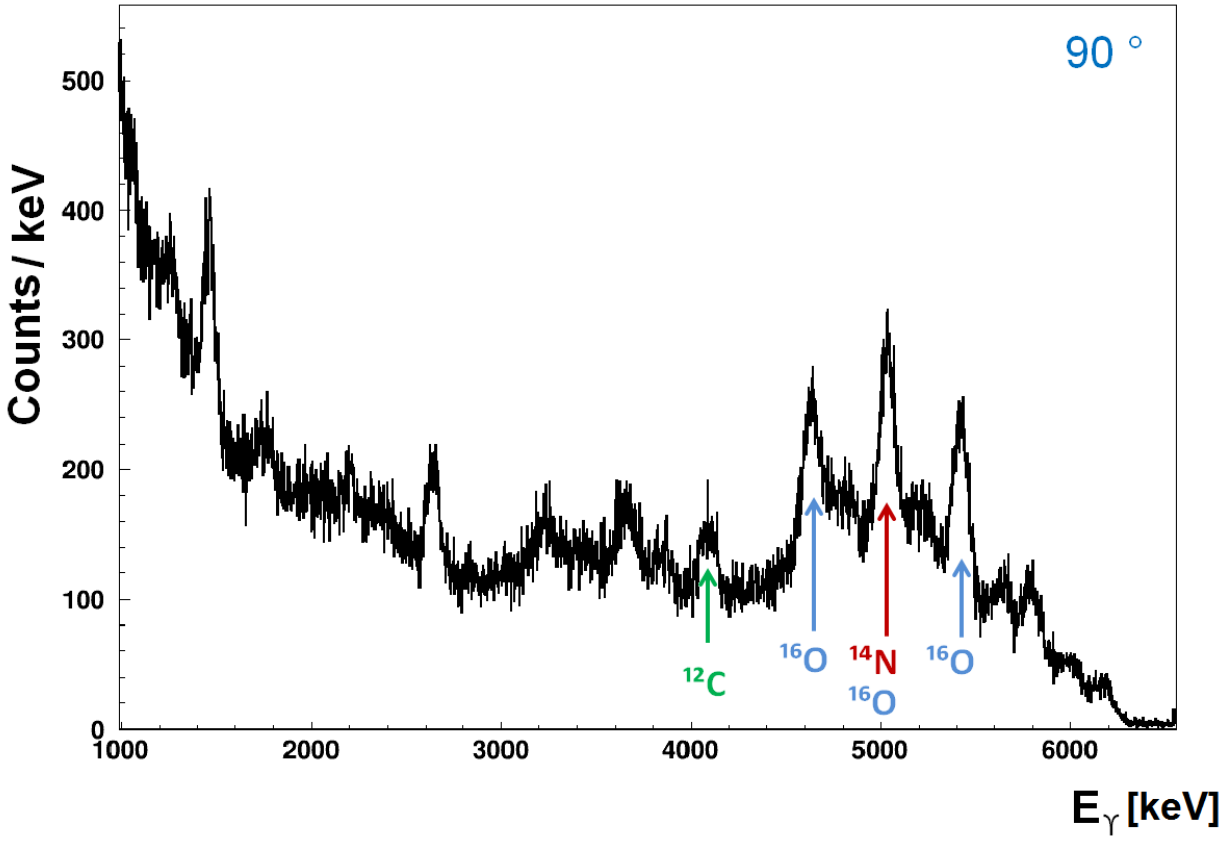

Figure 4.13: Measured prompt γ ray energy spectrum from the irradiation of a water phantom with 20 MeV protons using the $LaBr_3$ detector in June 2014. The Compton camera was mounted under an angle of 90 °relative to the incident beam. The linear energy calibration only includes energies up to 1.3 MeV. In green, the peak from the 4.44 MeV photons originating from the deexcitation of ^{12}C is marked. The red arrow indicates the 5.11 MeV peak from the ^{14}N deexcitation and in blue are shown the 6.13 MeV photopeak from the deexcitation of ^{16}O and its corresponding single- and double-escape peaks.

The linear energy calibration, only including energies up to 1.3 MeV, applied for both spectra from Figures 4.12 and 4.13, explains the strong deviations of the positions from excited nuclei transitions (indicated in Figure 4.13 by colored arrows).

From a GEANT4-based Monte-Carlo simulation of the $LaBr_3$ response to the irradiation of a water phantom with 20 MeV protons, an assignment of the observed peak structures in Figures 4.12 and 4.13 can be made. Figure 2.5 displays the corresponding simulated spectrum together with the assignments. This knowledge allows to interpret the measured γ ray energy spectra, which obviously suffer from a significant non-linear calibration characteristics, leading to strong deviation of the linear energy calibration from the expected peak positions

beyond ∼2 MeV.

In Figure 4.13 colored arrows indicate the contributions from the dominant nuclear interactions leading to excited states, which decay by photon emission. Figure 4.14 shows a fit to the ^{16}O group, including single- and double-escape peaks. The fit results in centroid positions of the peaks at 4.643 MeV (for the double-escape peak), 5.032 MeV(for the single-escape peak) and 5.420 MeV for the ^{16}O decay photopeak, instead of 5.108 MeV for the double-escape peak, 5.619 MeV for the single-escape peak and 6.13 MeV for the deexcitation of the first excited state in ^{16}O .

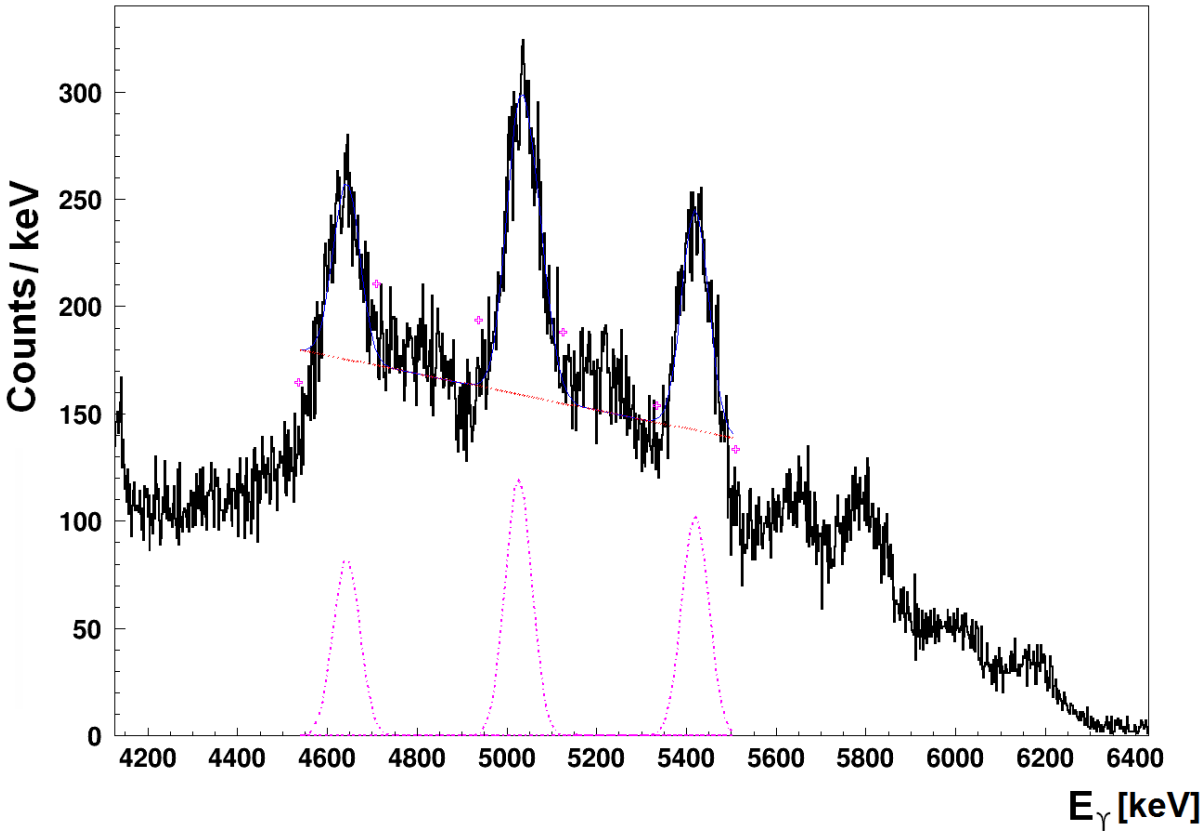

Figure 4.14: (Part of the) measured prompt γ ray energy spectrum registered by the $LaBr_3$ detector during the water phantom irradiation (from the data shown in Figure 4.13). The initial energy calibration only included energies up to 1.3 MeV. Therefore, the energetic positions of the three prominent peaks do not coincide with their respective transition energies: from left to right these peaks correspond to double-escape peak from the 6.13 MeV transition in ^{16}O, the corresponding single-escape peak (together with a weaker contribution from the 5.11 MeV deexcitation in ^{14}N) and finally the photopeak of the 6.13 MeV ground-state transition in ^{16}O. The dotted lines indicate Gaussian fit components to determine the energetic positions of the peak in the still linearly calibrated energy spectrum.

Beased on the firm assignment of the high-energy peak structure obtained from the simulated spectrum, these peaks can be included in the energy calibration procedure. Thus a set of calibration points ranging up to a photon energy of 6.13 MeV is available, which was used for the new energy calibrations already shown in Section 3.4, where a quadratic calibration was used to fit the calibration data up to 6.13 MeV. Figure 4.15 shows the resulting recalibrated new prompt γ ray energy spectrum. As it can be seen from Figure 4.15, the transition energies of the main γ ray transitions exhibit now the expected values. These dominant reaction channels (as described in Section 2.2 and Figure 2.5) are marked in the prompt γ ray energy spectrum from Figure 4.15 with colored arrows and are indicated with their transition energies.

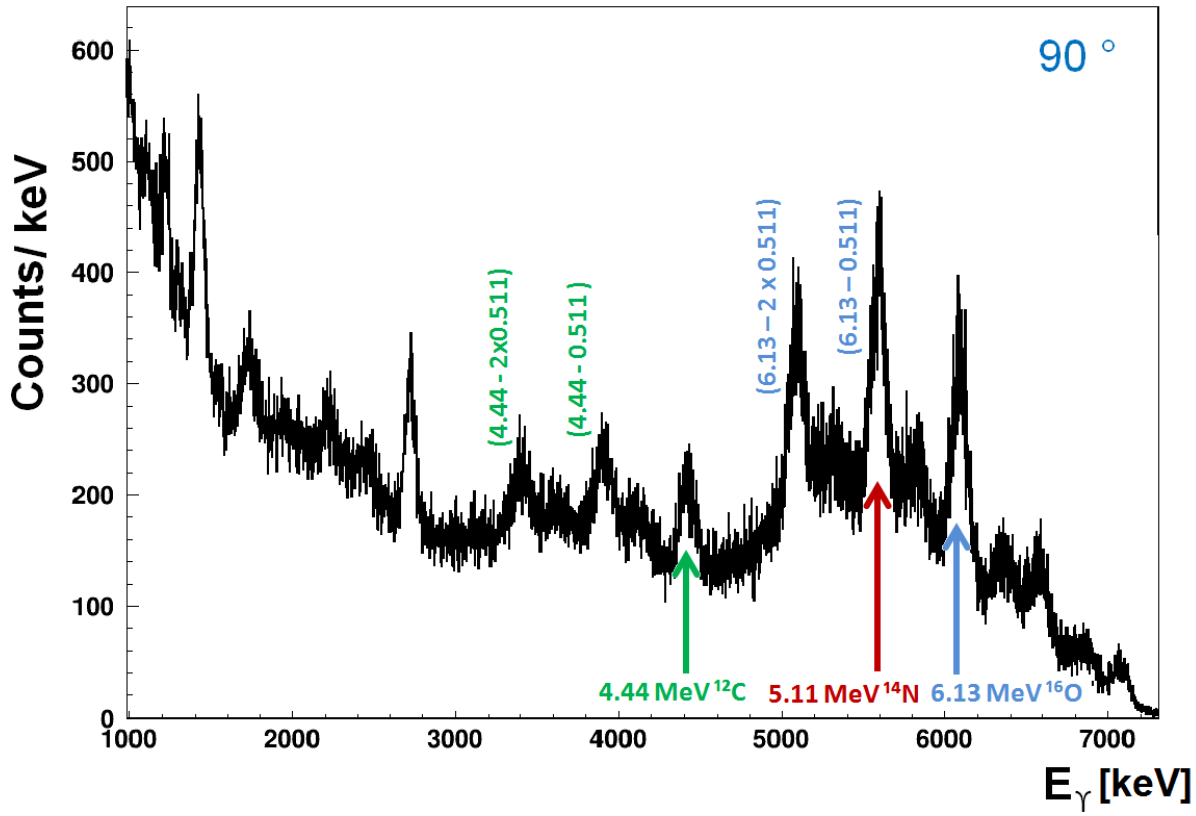

Figure 4.15: Measured prompt γ ray energy spectrum registered by the $LaBr_3$ detector during the water phantom irradiation. The Compton camera was mounted under an angle of 90°relative to the incident beam, and the (quadratic) energy calibration includes energies up to 6.130 MeV. The photopeaks from ground-state transitions in ^{12}C (4.44 MeV), ^{14}N (5.11 MeV) and ^{16}O (6.13 MeV) are marked with arrows, while the single- and double-escape peaks are marked with their respective transition energies.

The final γ ray energy spectrum from the water phantom, irradiation with 20 MeV protons is displayed in Figure 4.16. The spectrum was rebinned to 4 keV/bin, and a Gaussian fit was applied to check the quality of the energy calibration. The centroids of the dominant carbon and oxygen peaks were determined. The resulting comparison of nominal transition energies and calibrated peak positions (listed in Table 4.3) proves an accuracy of the energy calibration of 0.2-0.5%, which is more than sufficient for our purposes.

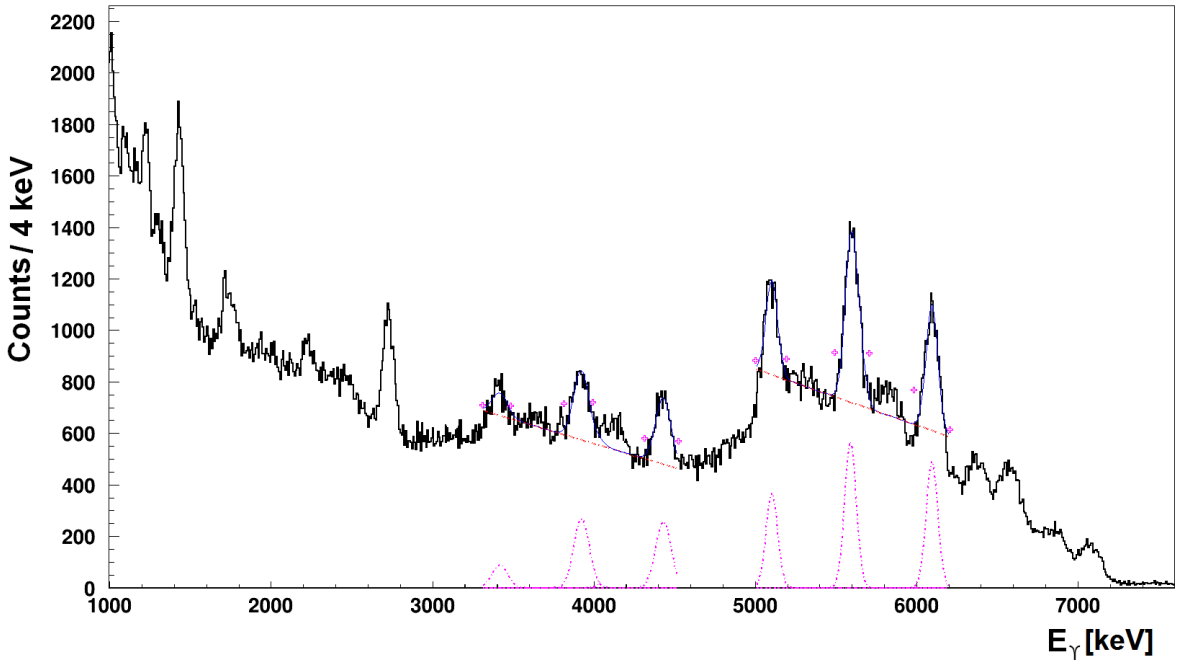

Figure 4.16: Rebinned prompt γ ray energy spectrum from Figure 4.15, where the ^{16}O group is represented by the dominant three peaks below 6 MeV. They were fitted with Gaussian fits, together with the photopeak, single- and double-escape peaks of the 4.44 MeV transitions in ^{12}C. The dashed straight red lines indicate the background assumptions included in the fitting procedure.

The fit results are shown in Table 4.3.

Isotope	^{12}C		^{16}O		
Energy [keV]	transition	measured	transition	measured	Type of transition
	4439	4430	6130	6095	photopeak
	3928	3922	5619	5614	single-escape
	3415	3416	5108	5104	double-escape

Table 4.3: Comparison of nominal transition energy values and calibrated peak positions.

Thus we can conclude, that the $LaBr_3$ absorber crystal is now fully understood and characterized, except the ongoing work on the spatial resolution in Section 3.4.

The planned experiment with a high-energy photon calibration (4.44 MeV) to be performed at the Dresden Tandetron facility will allow to characterize the energy response of the DSSSDs, which could not be performed from the data obtained in the Tandem accelerator experiments due to the multitude of transition energies contained in the obtained energy spectra.

5

Conclusions and Future Work

The described Master thesis project constitutes only a part of a R&D project, the development of a Compton camera for prompt γ-rays detection in hadron therapy. Nevertheless, significant contributions could be achieved during the course of the project: several contributions for the setup of the Compton camera infrastructure, namely

- work in the setup of the Faraday shielding cage, including tests and implementation of the fan unit;
- implementation of a temperature control in the Faraday cage;
- setup of Compton camera support structures;
- implementation of the full 256-channel readout electronics of the $LaBr_3$ detector;
- design improvements of the collimated ^{137}Cs source assembly.

Some tasks related to offline characterization measurements were also performed, such as

- energy calibration during the Tandem accelerator experiments;
- spatial measurements with a collimated ^{137}Cs source and setup improvements in this field.

Online characterization measurements were carried out with success, such as

- 2 experiments with a 20 MeV proton beam at the Garching Tandem accelerator;
- data analysis of the beam experiments and improvements in the analysis code and correction algorithms during the beamtime experiments.

Design tasks, for example:

- design of a new water phantom with a cylindric shape, based on Monte-Carlo simulations;
- design of a water phantom holder;
- design of a window for the Faraday Cage;
- design of a new frame for the ^{137}Cs source collimator used for spatial measurements.

Moreover, some MATLAB codes were developed, namely for the Fermi-function fits.

For the near future, several steps need to be performed, in order to work with the full capability that this complex system can offer. One of the priorities is the energy calibration of the DSSSD modules using the modified readout boards (for low E_γ). The modified readout boards will also allow for verifying the dynamic range of the GASSIPLEX boards, in order to quantify the gain factor of the multiplexing amplifiers, especially for clarifying the issue of reduced efficiency of the n side modules. Similar priority will be given to the development of an optimized collimator with 0.5 mm diameter, in order to complete the spatial resolution characterization of the $LaBr_3$ scintillator. Within this thesis project, already design drawings of a new support frame for the collimator assembly were developed.

A major improvement of the setup is still in progress: so far, only energy values were measured with the Compton camera detectors. Moreover, the choice in particular of the $LaBr_3$ scintillator was motivated by the supreme timing properties of this scintillator material, in order to allow for a discrimination of neutron background via time-of-flight measurements.

Therefore, the next step of completing the signal processing electronics comprises the installation of VME-based Time-to-Digital Converter modules (TDC). They will allow to precisely measure the arrival time of signals from the $LaBr_3$ detector.

Besides these hardware improvements, also significant efforts need to be invested to extend various software components, starting from the readout function for the new VME modules that needs to be developed and implemented into the readout code. Once the collimator frame is ready, new measurements using the ø0.5 mm collimator and the ^{137}Cs source need to be performed, in order to provide the adequate reference data set for the k-NN method. Once this reference data set (based on a 2D grid scan) is available, the data can be implemented to the k-NN method code for position reconstruction.

Existing data analysis codes will be extended to fully exploit all the correlations that can be extracted from the highly segmented detector systems to improve their understanding, also in view of scattering and cross-talk effects (for example, visible in different multiplicity distributions). These developments go hand in hand with an increasing understanding of the DSSSD modules and their GASSIPLEX-based boards. Developments have already started towards a next generation of DSSSD readout, potentially lifting some of the limitations presently imposed by the GASSIPLEX-based readout system, such as the lack of trigger functionality and monitoring output contacts.

Finally, also further simulations will be needed to better characterize the electron tracking with the DSSSD modules. Since all these further steps have already started or are foreseen for the near future, first imaging measurements with the Compton camera are within reach to exploit this powerful technique for online range monitoring of therapeutic hadron beams.

Appendices

A

Sketches

During this project development, many times it was also necessary to build some new tools. Then, one had to do the sketches and take them to the workshop. All this sketches were done in Google SketchUp, a 3D modeling tool used for several applications such as architecture, design, engineering and others. Here are some of the necessary works:

Design of the new water phantom

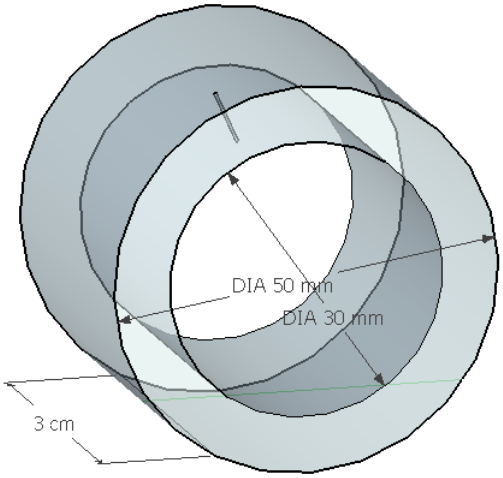

Figure A.1: Water phantom design. Detail of the back side.

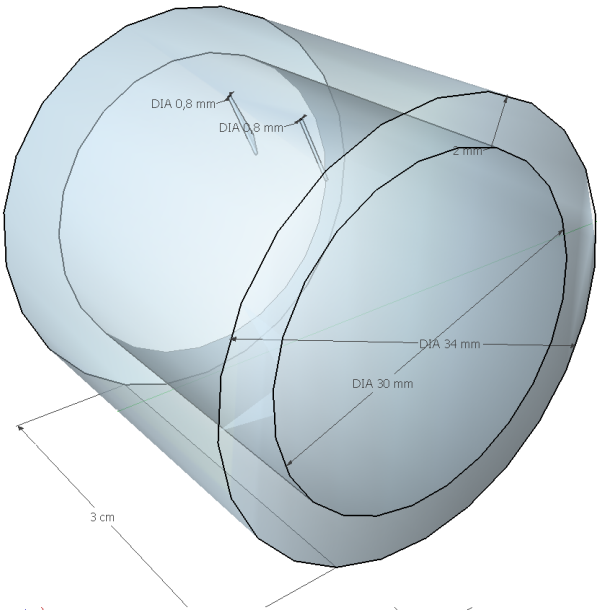

Figure A.2: Water phantom design. Detail of the side with the holes that allow to fill the water phantom using a needle.

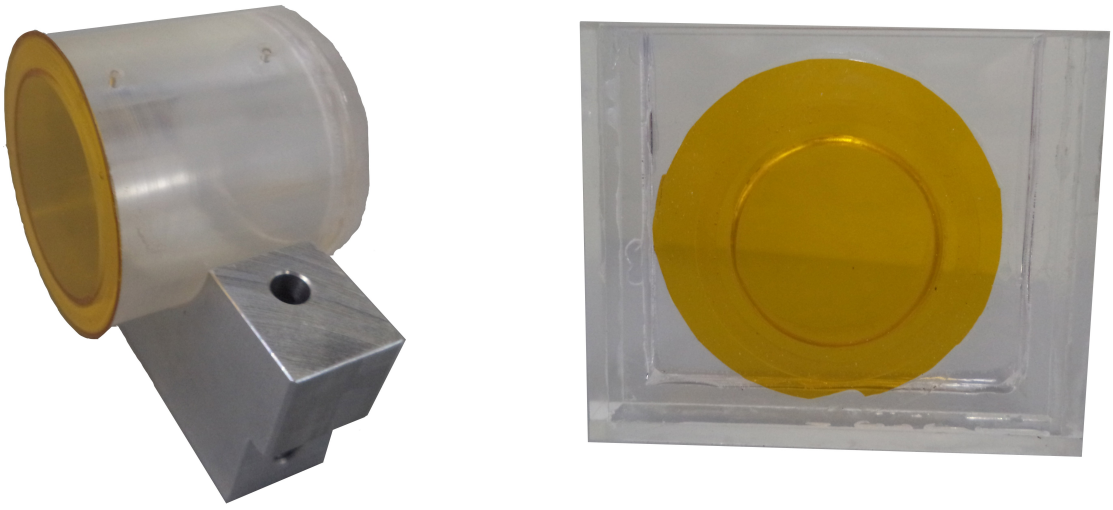

Figure A.3: Comparison of the new water phantom and part of its holder (left) with the old water phantom (right).

Design of the water phantom holder

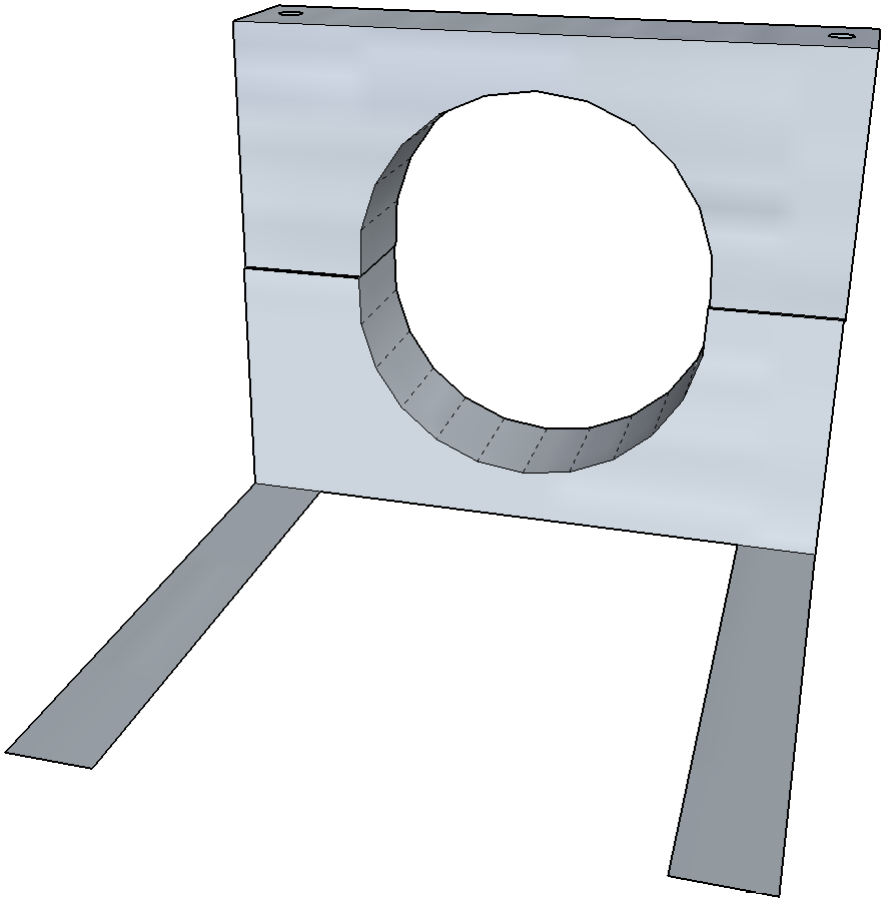

Figure A.4: New, and lighter water phantom holder, made of aluminum.

Design of the window for the Faraday Cage

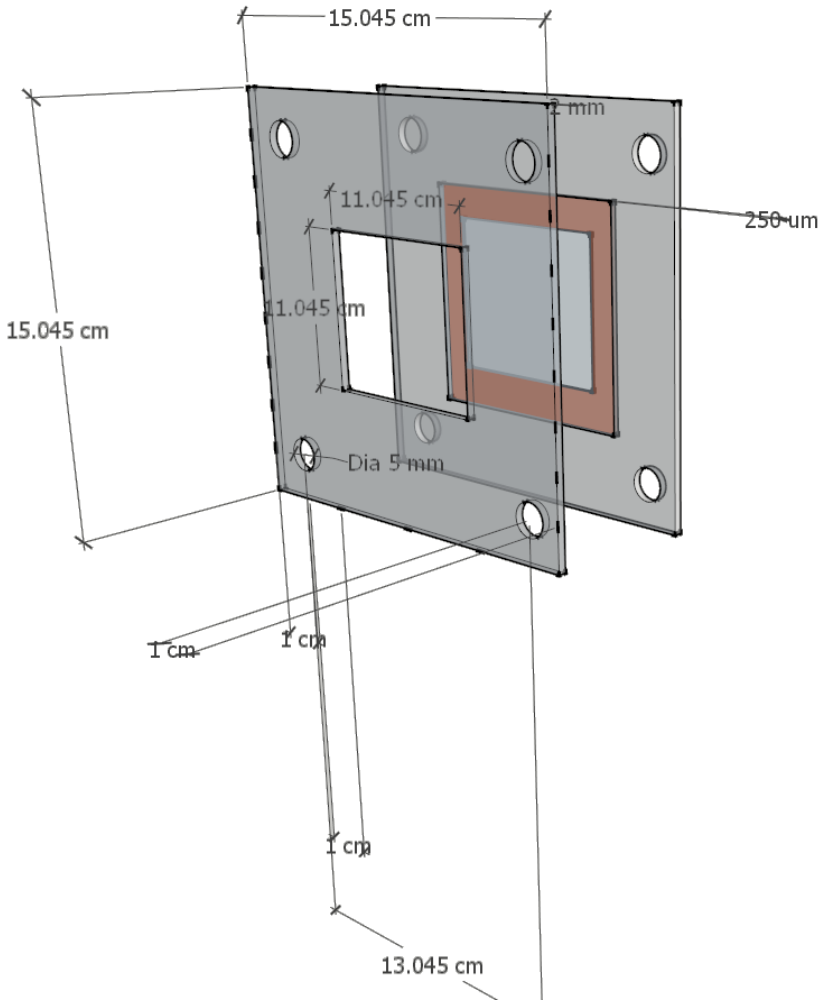

Figure A.5: Design of the window for the Faraday Cage (made of copper).

Design of the Copper frame for the 0.5 mm collimator

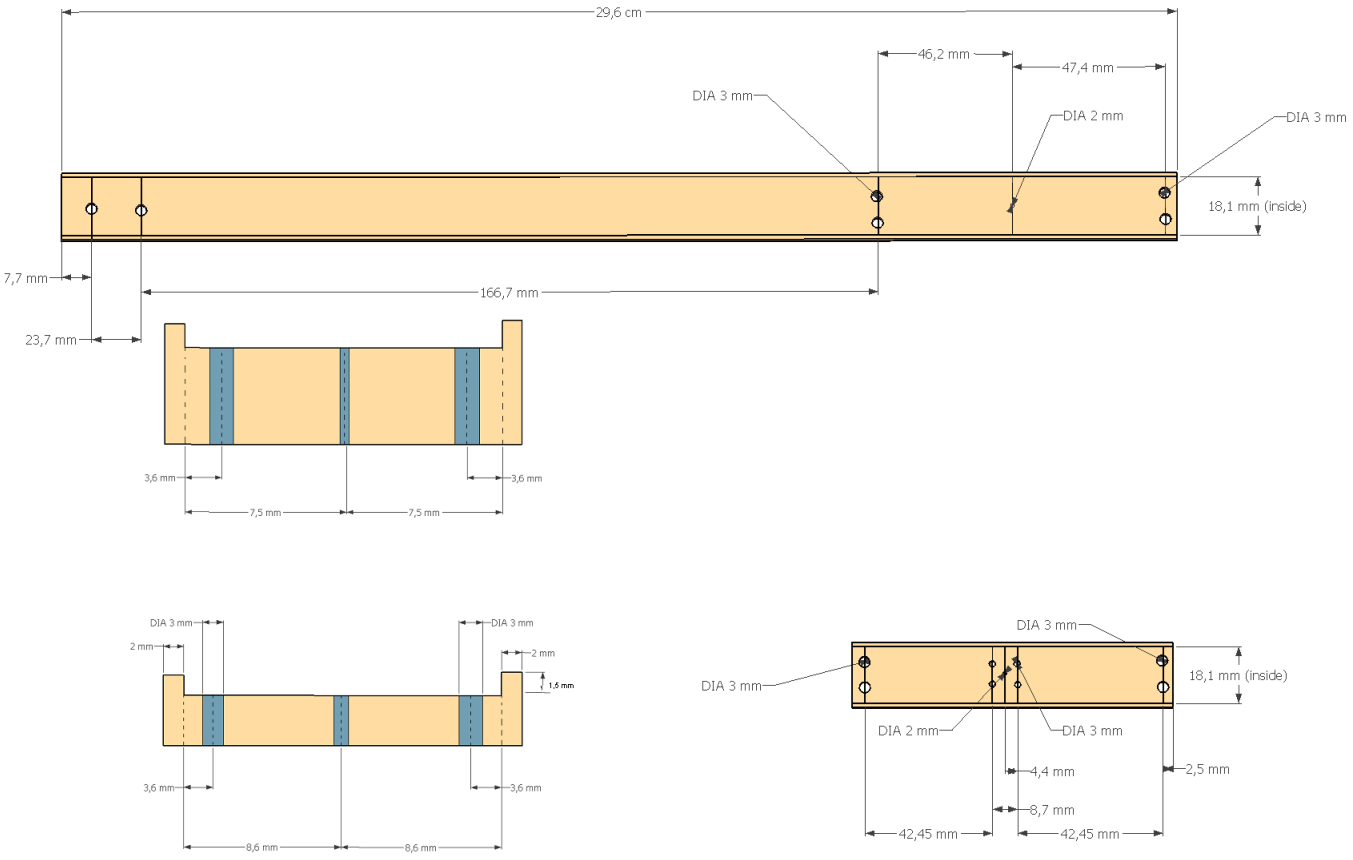

Figure A.6: Design of the Copper frame for the 0.5 mm (in diameter) collimator.

B

Methods and Materials

PMT readout adapter board

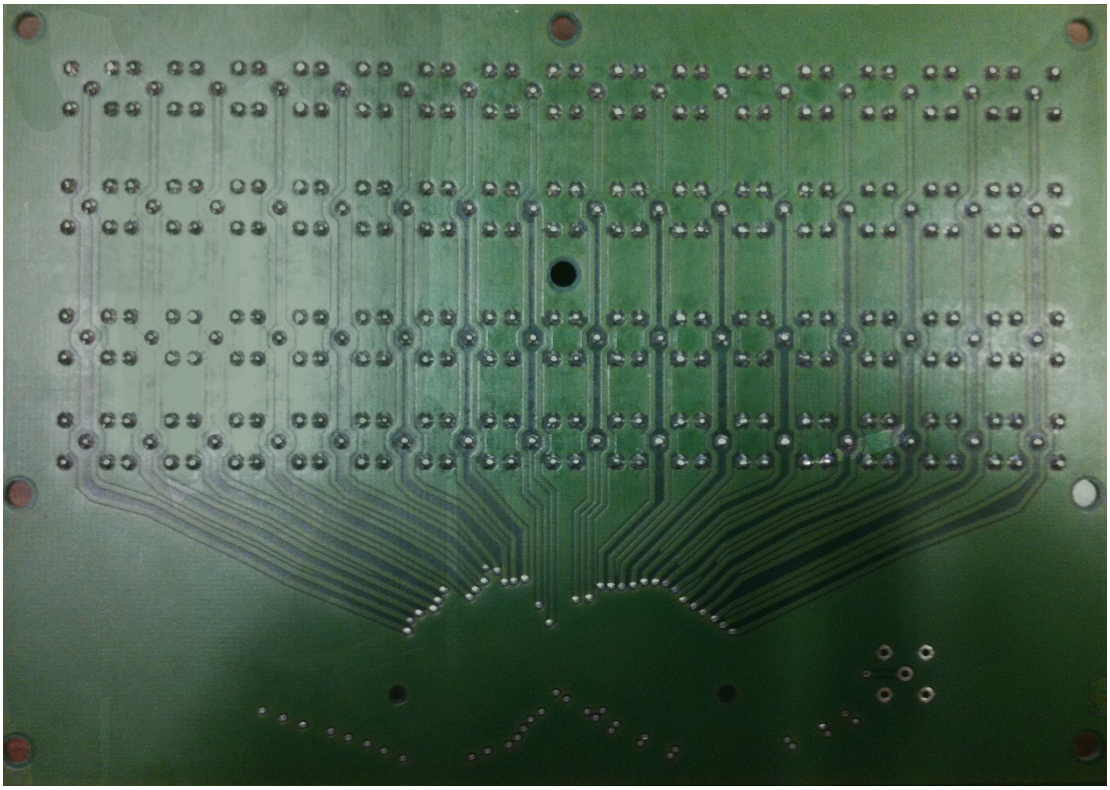

Figure B.1: PMT readout adapter board, detail of the back side.

Beam line reducer flange

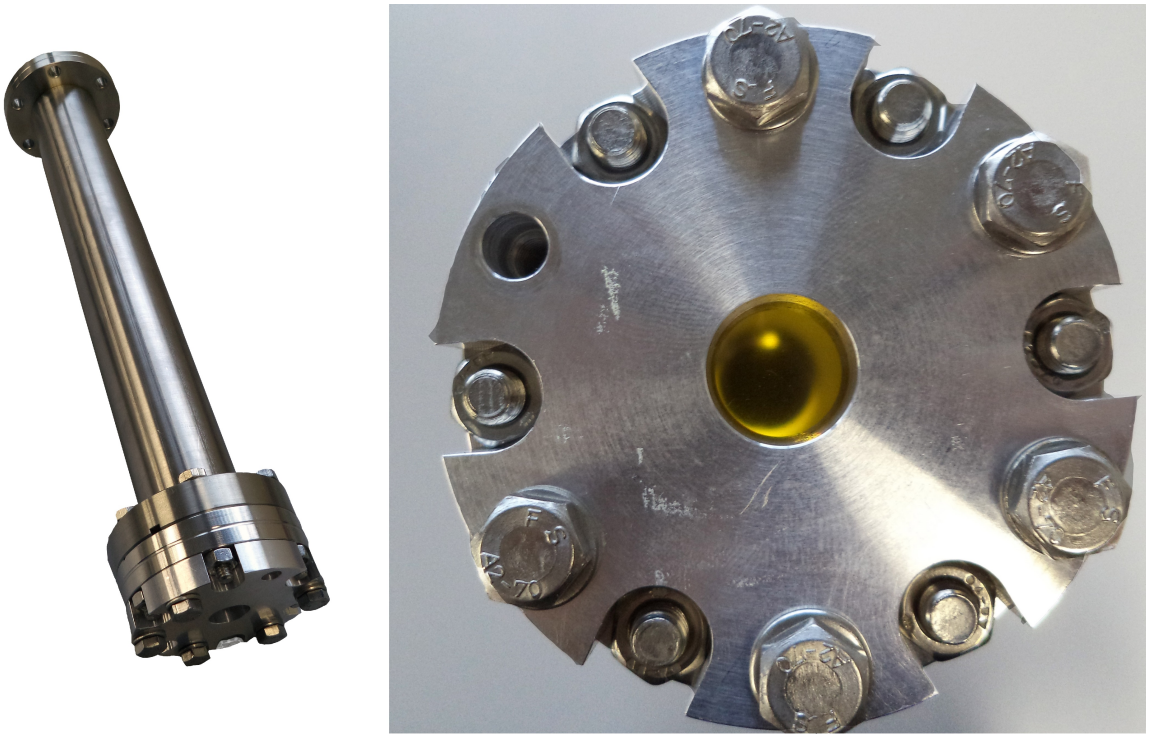

Figure B.2: Beam line reducer flange (from DN 100 to DN 40).

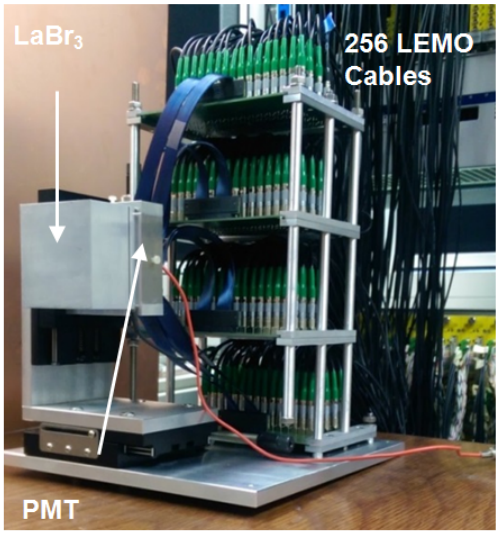

Figure B.3: $LaBr_3$ detector attached to the PMT, and PMT adapter board with 256 LEMO cables.

Arrangement of the two collimators

In Section 3.4, the arrangement of the setup using the 1 mm (in diameter) collimator and 1-4 slabs of the 0.5 mm (in diameter) collimator was mentioned. Here, the setup is represented, with the 1 mm collimator on the back side, and the slabs of the 0.5 mm collimator in front of it.

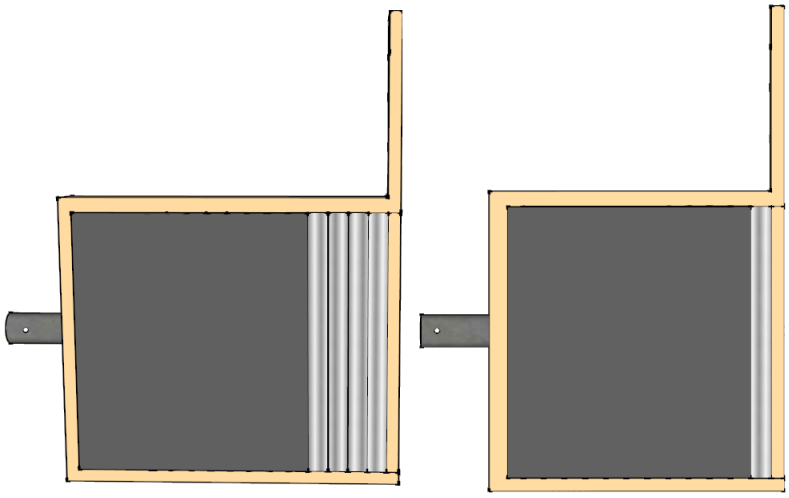

Figure B.4: Arrangement of the 1 mm collimator with the 0.5 mm collimator.

C

Results

Fermi-fits

Some MATLAB codes had to be developed in order to perform parallel analysis. Ideally, all these tools should be implemented in ROOT format, so that all the tasks could be done by *HistPresent* interface, but one decided that, as a first approach, this analysis would be done using MATLAB tools. MATLAB (**mat**rix **lab**oratory) "is a high-level language and interactive environment for numerical computation, visualization and programming". MATLAB is used for a wide range of applications, including signal processing and communications, image and video processing, control systems, tests and measurements (in several areas, such as psychology, medical physics, computational finance or biology). This software is able to perform numeric computation, data analysis, algorithm development, and others. The Fermi- and inverse Fermi-function fits mentioned in Section 3.5 were done using MATLAB and they are represented here:

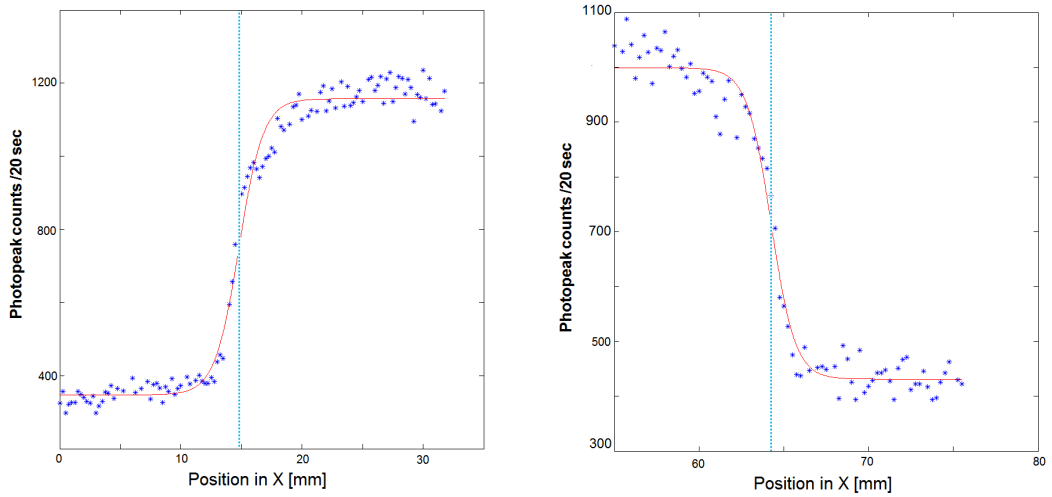

Figure C.1: An inverse Fermi- and a Fermi-function were fitted to the rising and falling edge of the count-rate profile from a scan in x direction, respectively, using the ø1 mm collimator and 2 additional slabs of the ø0.5 mm collimator. The points of inflection are marked with the blue dashed lines, with a value of x = 14.8 and x = 64.25 mm.

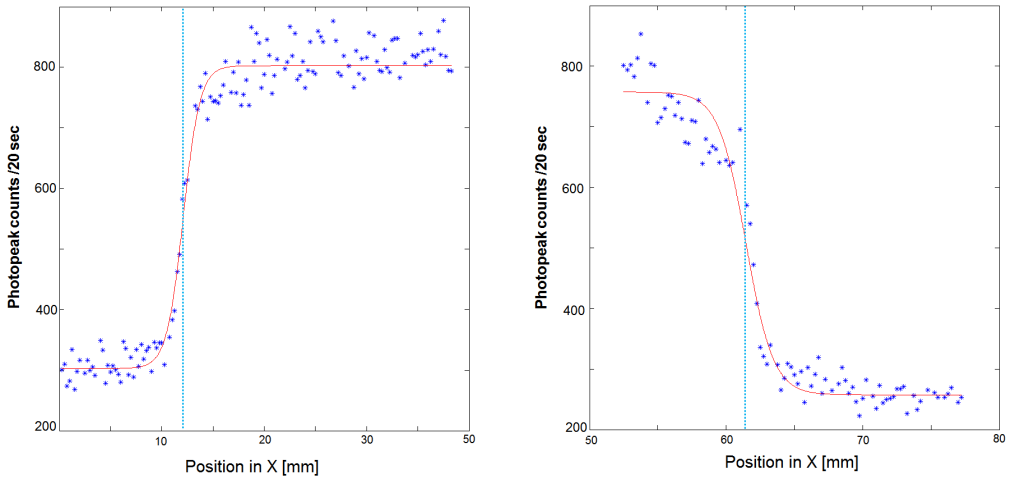

Figure C.2: An inverse Fermi- and a Fermi-function were fitted to the rising and falling edge of the count-rate profile from a scan in x direction, respectively, using the ø1 mm collimator and 3 additional slabs of the ø0.5 mm collimator. The points of inflection are marked with the blue dashed lines, with a value of x = 12.09 and x = 61.45 mm.

6

Bibliography

[1] Faculty of Physics, Chair of Experimental Physics; Online, December 2013; Available at: http://www.med.physik.uni-muenchen.de.

[2] Munich-Centre for Advanced Photonics; Online, December 2013; Available at: http://www.map.uni-muenchen.de/.

[3] M. Center, R. Siegel, A. Jemal, *Global Cancer: Facts & Figures*, American Cancer Society, 2011.

[4] Cancer Research UK; *Key facts for all cancers combined*; Online, August 2012; Last update: May 2012; Available at: http://info.cancerresearchuk.org/cancerstats/keyfacts/Allcancerscombined/018212#All.

[5] P. Crespo, *Optimization of In-Beam Positron Emission Tomography for Monitoring Heavy Ion Tumor Therapy*, PhD Thesis, Technische Universität Darmstadt, 2005.

[6] G. Kraft., *Tumortherapy with ion beams*, Nucl. Instrum. Meth A. 454 (2000), 1-10.

[7] Optivus Proton Therapy: *History of Proton Therapy*; Online, December 2013; Last Update: 2008; Available at: http://www.optivus.com/history.html.

[8] J.-M. Lagniel, *Hadrontherapy in Europe*, In 2007 Particle Accelerator Conference, Albuquerque, USA, June 2007.

[9] H. Paganetti, and T. Bortfeld, *Proton Beam Radiotherapy — the state of the art*, New Technologies of Radiation Oncology (Medical Radiology Series), 2005, 1-36.

[10] C. A. Tobias, J. H. Lawrence, J. L. Born, R. McCombs, J. E. Roberts, H. O. Anger, B. V. A. Low-Beer, and C. Huggins; *Pituitary irradiation with high energy proton beams: A preliminary report*, Cancer Research 18(1958), 121-139.

[11] C. A. Tobias, H. O. Anger, and J. H. Lawrence; *Radiological use of high energy deuterons and alpha particles*, Am. J. Roentgenol. Radium Ther. Nucl. Med. 67 (1952), 1-27.

[12] C.A. Tobias, D.C. Van Dyke, and M. E. Simpson; *Irradiation of the pituitary of the rat with high energy deuterons*, Am. J. Roentgenol. Radium Ther. Nucl. Med., 72:1-21, 1942.

[13] S. Falkmer, B. Fors, and B. Larsson; *Pilot study on proton irradiation of human carcinoma*, Acta Radiologica 58 (1962), 33-51.

[14] J-M. Lagniel, *Status of the Hadrontherapy Projects in Europe*, IEEE Applications of Accelerators, Technology Transfer and Relations with Industry, 2007.

[15] Rinecker Proton Therapy Center, Online, Available at: `http://www.rptc.de/en/`.

[16] S. Braccini, *Progress in Hadrontherapy*, Nucl. Phys. B PS 172 (2007), 8-12.

[17] U. Amaldi, S. Braccini, *Present challenges in hadrontherapy techniques*, Eur. Phys. J. Plus 126 (2011), 11070-4.

[18] M. H. Richard et al., *Design Guidelines for a Double Scattering Compton Camera for Prompt-γ Imaging During Ion Beam Therapy: A Monte Carlo Simulation Study*; IEEE Trans. Nucl. Sci., 58 (2011), 87-94.

[19] C-H. Min et al., *Prompt gamma measurements for locating the dose falloff region in the proton therapy*, Applied Physics Letters, 89 (2006), 183517.

[20] E. Testa, M. Bajard, M. Chevallier, D. Dauvergne, F. Le Foulher, N.Freud, J. Létang, J. Poizat, C. Ray, and M. Testa, *Dose profile monitoring with carbon ions by means of prompt-gamma measurements*, Nucl. Instr. Meth. B 267 (2009), 993-996.

[21] E. Testa et al., *Monitoring the Bragg peak location of 73 MeV/u carbon ions by means of prompt γ-ray measurements*, Applied Physics Letters, 47 (2008), 093506.

[22] M. Engelsman, M. Schwarz, L. Dong, *Physics controversies in proton therapy*, Semin. Radiat. Oncol. 23 (2013), 88-96.

[23] U. Ratzinger, G. Clemente, C. Commenda, H. Liebermann, H. Podlech, R. Tiede, W. Barth, L. Groening, *A 70 MeV proton linac for the FAIR facility based on CH-cavities*, in Proc. LINAC 2006 (2006), 526-530.

[24] U. Amaldi, S. Braccini, P. Puggioni, *High-frequency Linacs for Hadrontherapy*, Reviews of Accelerator Science and Technology 2 (2009), 111-131.

[25] W. Enghardt et al., *Charged hadron tumor therapy monitoring by means of PET*, Nucl. Instr. Meth. A 525 (2004), 284-288.

[26] C. Lang, D. Habs, K. Parodi, and P.G. Thirolf, *Sub-millimeter nuclear medical imaging with high sensitivity in positron emission tomography using β^+ coincidences*, Journal of Instrumentation 9 (2014), P01008.

[27] M.E. Phelps, *PET - Physics, Instrumentation and Scanners*, Springer, 2006.

[28] A. van der Veldt, E. Smit, A. Lammertsma, *Positron emission tomography as a method for measuring the drug delivery to tumors* in vivo*: the example of ^{11}C docetaxel*, Front. Oncol. 13 (2013), 208.

[29] E. Urakabe et al., *Spot scanning using radioactive ^{11}C beams for heavy-ion radiotherapy*, Jpn. J. Appl. Phys. 40 (2001) 2540.

[30] H. Mizuno et al., *Washout measurement of radioisotope implanted by radioactive beams in the rabbit*, Phys. Med. Biol. 48 (2003) 2269.

[31] T. Inaniwa et al., *Quantitative comparison of suitability of various beams for range monitoring with induced β^+ activity in hadron therapy*, Phys. Med. Biol. 50 (2005) 1131.

[32] P.G. Thirolf, *On the role of nuclear fragmentation for the advancement of in-vivo medical imaging*, 4th Int. Conf. on Nuclear Fragmentation (Kemer (Antalya), Turkey), 2013.

[33] D.R. Schaart, *Emerging detector technologies in time-of-flight positron emission tomography*, MLL-Kolloquium, 2013.

[34] M. Conti, *State of the art and challenges of time-of-flight PET*, Physica Medica 25 (2009), 1-11.

[35] Deutsches Elektronen-Synchroton, Particle Physics, *PET R& D in Hamburg: Introduction to PET*; Online, September 2014; Available at: `http://www-flc.desy.de/pet/intro.php`; Last Update: December 2012.

[36] F. Stichelbaut, Y. Jongen, Meeting of the 30^{th} Particle Therapy Cooperative Group, San Francisco, October 2003, unpublished.

[37] R.W.Todd et al., *A proposed γ camera*, Nature 251 (1974), 132-4.

[38] M. Singh and D. Doria, *An electronically collimated gamma camera for single photon emission computed tomography: part II. Image reconstruction and preliminary experimental measurements*, Med. Phys. 10 (1983), 428.

[39] T. Kormoll, F. Fiedler, C. Golnik, K. Heidel, M. Kempe, S. Schoene, M. Sobiella, K. Zuber, and W. Enghardt, *A prototype Compton camera for in-vivo dosimetry of ion beam cancer irradiation*, 2011 IEEE Nuclear Science Symposium and Medical Imaging Conference (NSS/MIC) (2011), 3484-3487.

[40] M. Frandes, *Gamma-ray detection and compton camera image reconstruction with application to hadron therapy*, PhD thesis, University of Lyon, 2010.

[41] L. J. Harkness, A. J. Boston, H. C. Boston, R. J. Cooper, J. R. Cresswell, A. N. Grint, P. J. Nolan, D. C. Oxley, D. P. Scraggs, T. Beveridge, J. Gillam, and I. Lazarus, *Optimization of a dual head semiconductor compton camera using GEANT4*, Nucl. Instr. Meth. A. 604 (2009), 351-354.

[42] M. H. Richard, *Design study of a Compton camera for prompt-gamma imaging during ion therapy*, PhD thesis, University Claude Bernard Lyon, 2012.

[43] G.F. Knoll, *Radiation Detection and Measurement*, 4th. ed., John Wiley & Sons, Hoboken, 2010.

[44] K. Krane, *Introductory Nuclear Physics*, John Wiley & Sons, 1987, 191-207.

[45] National Institute of Standards and Technology (NIST), XCOM —*Photon Cross Sections Database*; Online, September 2014; Available at: `http://physics.nist.gov/PhysRefData/Xcom/html/xcom1.html`; Last update: December 2011.

[46] USGS, THE USGS Water Science School, *The water in you*, Online, August 2014; Available at: `http://water.usgs.gov/edu/propertyyou.html`.

[47] Encyclopedia of Science, *Biological abundance of elements*, Online, August 2014; Available at: `http://www.daviddarling.info/encyclopedia/E/elbio.html`.

[48] C. Lang, *PhD Thesis*, Ludwig Maximilians Universität München, 2014, in preparation.

[49] H. Daido, M. Nishiuchi and A.S. Pirozhkov, *Review of laser-driven ion-sources and their applications*, Rep. Prog. Phys. 75 (2012), 056401.

[50] S. Karsch, *CALA and Garching plans*, EuroNNAc Workshop, CERN, Geneva, May 2011.

[51] H.T. Kim et al., *Enhancement of electron energy to multi-GeV regime by a dual-stage laser-wakefield accelerator pumped by petawatt laser pulses*, Phys. Rev. Lett. 111 (2013), 165002 .

[52] D. Jung et al., *Laser-driven 1 GeV carbon ions preheated diamond targets in the break-out afterburner regime*, Phys. Plasmas 20 (2013), 083103.

[53] H. van der Kolff, *Characterization of the absorbing detector component of a Compton Camera designed for beam range verification in hadron therapy*, Master Thesis, TU Delft and Ludwig-Maximilians-Universität München , 2014.

[54] J.D. Irwin, R.M. Nelms, *Basic Engineering circuit analysis*, 9th ed., John Wiley & Sons, 2008.

[55] M. Tooley, *Electronic Circuits: Fundamentals and Applications*, 3rd ed., Routlege, 2012.

[56] P.G. Thirolf, *Basics on Silicon detector technology*, Radiation Detectors for Medical Applications - Lecture, 2013; Online, September 2014; Available at: `http://www.physik.uni-muenchen.de/lehre/vorlesungen/sose_13/radiation-detectors-for-medical-applications/downloads/ss13_silicon-basics_06.pdf`

[57] S. Takeda, *Experimental study of a Si/CdTe semiconductor Compton camera for the next generation of gamma-ray astronomy*, PhD, Institute of Space and Astronautical Science, 3-1-1, Yoshinodai, Sagamihara 229-8510, Japan, 2012.

[58] E.B. Podgorsak, *Basic Radiation Physics - A Handbook for Teachers and Students*, International Atomic Energy Agency, Vienna, 2005.

[59] Saint-Gobain, Saint-Gobain Crystals; Online, December 2013; Available at: `http://www.detectors.saint-gobain.com/`.

[60] S. Seifert, *Silicon photomultipliers and monolithic scintillators for time-of-fight PET*, BOXPress, 2012.

[61] D.N. Ter Weele, D.R. Schaart, P. Dorenbos, *The Effect of Self-absorption on the Scintillation Properties of Ce^{3+} Activated $LaBr_3$ and $CeBr_3$*, IEEE Trans. Nucl. Sci. 61 (2014), 683-689.

[62] P.G. Thirolf, *Status of a Compton camera prototype for online range verification of proton beams*, Joint Conference of the SGSMP, Zurich, 2014.

[63] L. C. Parra, *Reconstruction of cone-beam projections from Compton scattered data*, IEEE Trans. Nucl. Sci. 47 (2000), 1543-1550.

[64] A. Zoglauer et al., *MEGAlib —Simulation and Data Analysis for Low-to-medium-energy Gamma-ray Telescopes*, MEGAlib Documentation; Online, September 2014; Available at: `http://megalibtoolkit.com/documentation`.

[65] H.T. van Dam et al., *Improved Nearest Neighbor Methods for Gamma Photon Interaction Position Determination in Monolithic Scintillator PET Detectors*, IEEE Trans. of Nucl. Sci. 58 (2011), 2139-2147.

[66] E. Fix and J. L. Hodges, Discriminatory Analysis, *Nonparametric Discrimination: Consistency Properties*, USAF School of Aviation Medicine, Randolph Field, Technical Report 4, 1951.

[67] M. C. Maas et al., *Experimental Characterization of monolithic-crystal small animal PET detectors read out by APD arrays*, IEEE Trans. Nucl. Sci. 53 (2006), 1071-1077.

[68] Carel W.E. van Eijk, *Inorganic scintillators in medical imaging*, Physics in Medicine and Biology, 47 (2002), R85-R106.

[69] Saint-Gobain Ceramics & Plastics, *BrilLance^{TM}380 Scintillation Material*; Online, July 2014; Last update: 2014; Available at: http://www.crystals.saint-gobain.com.

[70] F. Quarati et al., *Study of 138La radioactive decays using LaBr3 scintillators*, Nucl. Instr. Meth. A 683 (2012), 46-52.

[71] Mesytec GmbH & Co. KG, *MCFD-16 Data sheet*, Online, July 2014; Available at: `http://www.mesytec.com/datasheets/MCFD-16.pdf`.

[72] Mesytec GmbH & Co. KG, *MQDC-32 Data sheet*, Online, July 2014; Available at: `http://www.mesytec.de/datasheets/MQDC-32l.pdf`.

[73] *3M^{TM} Twisted Pair Flat Cable 3782 Series*, Online, July 2014; Available at: http://multimedia.3m.com/mws/mediawebserver?66666UuZjcFSLXTtOxfEOxz6EVuQEcuZgVs6EVs6E666666-.

[74] R. Lutter et al., Proc. of IEEE Conf. on Realtime Computing, Santa Fe, New Mexico (1999), and: *MARaBOU - A MBS and ROOT Based Online/Offline Utility*; Online, July 2014; Available at: http://www.bl.physik.uni-muenchen.de/marabou/htmldoc/marabou/GeneralDescription.html.

[75] T. Hoffmann, P. Forck, D.A. Liakin, *New Spill Structure Analysis Tools for the VME Based Data Acquisition System ABLASS at GSI*, AIP Conf. Proc. 868 (2006), 343-350.

[76] D. Siwal et al., *A VME based Data Acquisition system Pulse Shape Recording of gamma-ray detector*, Proc. of the DAE Symp. on Nucl. Phys. 56 (2011), 1050-1051.

[77] Techno isel, *Davinci XYZ gantry table system*; Online, August 2014; Available at: http://www.techno-isel.com/tic/Gantries.htm.

[78] isel Automation, isel-schrittmotor-steuerung C 10C und C 10C-E/A hardware-beschreibung (1995).

[79] Z. Dilli, *Intrinsic and Extrinsic Semiconductors, Fermi-Dirac Distribution Function, the Fermi level and carrier concentrations*, ENEE 313 (2009), Supplement I.

[80] CiS Forschungsinstitut für Mikrosensorik und Photovoltaik GmbH; Online, June 2014; Available at: http://www.cismst.org/.

[81] CERN, *Technological Developments at CERN in 1995*; Online, July 2014; Available at: http://alice-hmpid.web.cern.ch/alice-hmpid/publicns/ecp-94-017.pdf.

[82] Subatech, *A 16 integrated channels front end analog amplifiers with multiplexed serial readout*; Online, July 2014; Available at: http://www-subatech.in2p3.fr/ electro/projets/beta_imageur/data/gassiplex/gassplex0_7_3_QFP.pdf.

[83] F. Lehner, *The phenomenology of the micro discharge effects on Døsilicon modules*, Fermilab, Dønote 3804; Online, July 2014; Available at: http://d0server1.fnal.gov/projects/Silicon/www/Writeups/m_micro.ps.

[84] item®, MB Building Kit System, Online, Available at: http://www.item24us.com/products/mb-building-kit-system .

[85] H. Huang, G. Quan, J. Fan, *Leakage Temperature Dependency Modelling in System Level Analysis*, published in: 11*th* International Symposium on Quality Electronic Design (2010), 447-452.

[86] Pico® Technology, *PT-104 Data Logger Data Sheet*, Online, July 2014; Last Update: 2012; Available at: `http://www.picotech.com/document/datasheets/usbpt104pg.en-2.pdf`.

[87] C. Wrede, *New DSSSD mount and cooling system*, DRAGON Report, 2003; Online, Available at: `http://dragon.triumf.ca/docs/CoolingReport.pdf`.

[88] O. Toker, S. Masciocchi, E. Nygård, A. Rudge, P. Weilhammer, *VIKING, a CMOS low noise monolithic 128 channel frontend for Si-strip detector readout*, Nucl. Instr. Meth. A 340 (1994), 572-579.

[89] R. Andritschke, *Calibration of the MEGA Prototype — Hardware and Performance of a Combined Tracking Compton and Low-energy Pair Creation Telescope*, PhD Thesis, Technische Universität München, 2006.

[90] S. Aldawood, *PhD Thesis*, Ludwig Maximilians Universität München, in preparation.

[91] Maier-Leibnitz-Laboratorium (MLL), Tandem-Beschleuniger; Online, June 2014; Available at: `http://www.bl.physik.uni-muenchen.de/tandem/index.html`.